A Two-dimensional Hybrid-Direct Kinetic Model of a Hall Thruster

by

Astrid L. Raisanen

A dissertation submitted in partial fulfillment
of the requirements for the degree of
Doctor of Philosophy
(Aerospace Engineering)
in the University of Michigan
2020

Doctoral Committee:

Assistant Professor Benjamin Jorns, Chair
Professor Iain D. Boyd
Professor John E. Foster
Assistant Professor Kentaro Hara
Professor Mark J. Kushner

"The wide world is all about you:
you can fence yourselves in,
but you cannot forever fence it out.

– J. R. R. Tolkien, *The Fellowship of the Ring*

Astrid L. Raisanen

astridr@umich.edu

ORCID iD: 0000-0001-5152-0661

For my family

ACKNOWLEDGMENTS

Although this work is the culmination of a number of years of study and research at the University of Michigan (UM), one could argue that the journey to its inception began long ago, and this thesis is simply another step in the process of lifelong learning. To my mentors, instructors, colleagues, family, and friends: thank you.

First, I would like to acknowledge my thesis advisor, Prof. Iain Boyd. I entered his laboratory with an interest in computational work and gas dynamics, but I knew almost nothing about plasmas, and I am grateful that I was able to delve deeply into a new topic. Prof. Boyd was a supportive and flexible advisor, and this allowed me to balance my academic responsibilities throughout the duration of my program, take several courses, attend a variety of workshops and conferences, and take advantage of a wide array of learning opportunities.

I would also like to thank my committee members. Prof. Ken Hara, an alum of the Nonequilibrium Gas and Plasma Dynamics Laboratory (NGPDL), was one of my biggest advocates and mentors, particularly early on in my research. I truly appreciate all of the discussions we had about my present research and ideas for the future. Prof. Mark Kushner, in addition to giving useful career advice, taught a fantastic course on plasma-chemistry interactions that I consider one of the most useful courses in my time at UM. Prof. John Foster taught a course on experimental plasma physics, and this exposed me to the methods that are used to collect the data that I utilized in my computational work. Prof. Ben Jorns introduced me to his former colleagues at NASA's Jet Propulsion Laboratory (JPL) and some years later agreed to chair my thesis committee when my own advisor left UM. I would also like to acknowledge Prof. Mirko Gamba and Prof. Ken Powell, both of whom I had the privilege to work with as a graduate student instructor. Other faculty in the aerospace, nuclear, and chemical engineering departments also contributed to my learning.

Members of the administration in Aerospace Engineering, including Denise Phelps and Jessica Jones, were also instrumental in ensuring that funding and resources were taken care of so that I could focus on research. Further, I would also like to acknowledge my funding sources. My work at the University of Michigan was primarily sponsored by a grant from the Air Force Office of Scientific Research (AFOSR), with partial funding from a Rackham School of Graduate Studies fellowship and a fellowship from the Department of Aerospace Engineering. I was fortunate to intern at the Air Force Research Laboratory (AFRL) in Edwards, CA, and I would be remiss if I did not acknowledge the support and friendship of Dr. Justin Koo and Dr. David Bilyeu, among others.

Next, I would like to thank my colleagues and friends at UM. I would like to acknowledge my friends in NGPDL, particularly Dr. Lauren Mackey, Dr. Horatiu Dragnea, Dr. Maria Choi, Dr. Brandon Smith, and Alex Vazsonyi. First year courses and subsequent qualifying exams would not have been the same without Logan White, Dr. Jacob Francis, Dr. Eric Parish, and Dr. Devina Sanjaya. I would also like to extend thanks to my friends in the Plasmadynamics and Electric Propulsion Laboratory (PEPL), particularly Dr. Sarah Cusson, Dr. Ethan Dale, Dr. Marcel Georgin, Dr. Scott Hall, Shad Hepner, and Ben Wachs for useful discussions on plasma physics and hall thrusters. To all the other friends at UM with whom I danced, did martial arts, ran, had a mug of coffee or glass of wine, and commiserated about the graduate school experience: thank you.

I would like to acknowledge my family and their role in this effort. My parents, Brita and Warren, raised an independent, first generation college student, and they, along with my siblings (Peter, Emmalee, Spencer, Madeline, Olivia, Emmett, and Lidia) and grandparents, have been supportive of my academic endeavors. My parents-in-law, Alison and Henry, have also been my cheerleaders for most of the journey to my Ph. D., and their support has not gone unnoticed, particularly in the last couple years of this effort. Last, but certainly not least, I would like to thank my husband, Mick. I never imagined that I would meet my life partner at a mixer for new engineering graduate students or that we would spend most

of my graduate school experience living across the country from one another. He has been the greatest support of all. He asked questions, helped me hash out ideas from time to time, and simply listened when things got frustrating and I ran into the dead ends that so often accompany open-ended research. A thousand times, thank you.

TABLE OF CONTENTS

LIST OF FIGURES

FIGURE

LIST OF TABLES

TABLE

LIST OF APPENDICES

APPENDIX

LIST OF ABBREVIATIONS

UM University of Michigan

NGPDL Nonequilibrium Gas and Plasma Dynamics Laboratory

JPL Jet Propulsion Laboratory

AFOSR Air Force Office of Scientific Research

AFRL Air Force Research Laboratory

PEPL Plasmadynamics and Electric Propulsion Laboratory

HET Hall effect thruster

BBGKY Bogoliubov Born Green Kirkwood Yvon

MHD magnetohydrodynamics

PIC particle-in-cell

Isp specific impulse

DK direct kinetic

PPT pulsed plasma thruster

MPD magnetoplasmadynamic

EP electric propulsion

SPT stationary plasma thruster

TAL thruster with anode layer

PPT pulsed plasma thruster

GEO Geosynchronous Earth Orbit

VDF velocity distribution function

MCC Monte Carlo collision

DSMC direct simulation Monte Carlo

LTE local thermodynamic equilibrium

PDEs partial differential equations

VDF velocity distribution function

ECDI electron cyclotron drift instability

CEX charge exchange

ODEs ordinary differential equations

CFL Courant Friedrichs Lewy

MUSCL monotonic upwind scheme for conservation laws

MPI Message Passing Interface

SEE secondary electron emission

RF radio frequency

SCL space charge limited

SMG semicoarsening multigrid

AMR Adaptive mesh refinement

ABSTRACT

The goal of this dissertation is to improve the state-of-the art modeling approaches available for simulating the discharge plasma in a Hall effect thruster (HET). A HET is a space propulsion device that utilizes electrical energy to ionize and accelerate propellant, generating thrust. The device features a cross-field configuration, whereby the transverse magnetic field traps electrons, and the axial electric field electrostatically accelerates ions out of the thruster channel. This configuration enables desirable thruster performance characteristics typically characterized by a relatively high specific impulse (1000-3000 s) and a high thrust density (a few N m^{-2}).

High fidelity computational models are useful to investigate the physical processes that govern the HET's performance, efficiency, and lifetime limitations. The non-equilibrium nature of the plasma transport should be resolved so that the flow can be accurately characterized. A grid-based direct kinetic (DK) simulation is capable of modeling the non-equilibrium state of plasma without the numerical noise that is inherent to particle-based methods since the velocity distribution functions (VDFs) are obtained in a deterministic manner. As the primary objective of this work, a two-dimensional, hybrid-DK simulation of the discharge plasma in a HET is developed. As a secondary objective, a plasma sheath, one of the important physical structures that form in the discharge plasma of a HET near the channel walls, is examined via a two-dimensional full DK simulation that highlights slight spatial differences in the sheath as a result of electrically disparate, adjacent wall materials. The memory storage requirements and computational load for the parallelized

DK simulation grow with additional species, physical space dimensions, and velocity space dimensions. Some of these numerical limitations are encountered within this work.

The hybrid-DK HET model utilizes a quasi-one-dimensional fluid electron algorithm in conjunction with a two-dimensional DK method to simulate the motion of neutral atoms and ions in a HET channel and near-field plume. Upon its development, the hybrid-DK simulation is benchmarked against results obtained from a two-dimensional hybrid-particle-in-cell (PIC) simulation with an identical fluid electron algorithm. To achieve agreement between the simulation results, a boundary condition for the DK model that satisfies particle conservation at the wall boundaries is developed, and electron model boundary conditions that provide solution stability are sought and utilized. For both high-frequency and low-frequency oscillations, the two simulations show good agreement for both time-averaged and dynamic plasma properties. Statistical noise tends to randomize plasma oscillations in the PIC simulation results, whereas the DK results exhibit coherent oscillatory behavior. Furthermore, results indicate that the DK simulation is capable of responding to small changes in electron dynamics, which is promising for future work.

The DK plasma sheath simulation models a two-dimensional plasma sheath that highlights slight spatial differences inside the sheath as a result of electrically disparate, adjacent materials. To accomplish this goal, a quasi-one-dimensional sheath model is first built in a two-dimensional framework, boundary conditions are developed, and results are verified against theoretical expectations. Then, the full two-dimensional plasma sheath is modeled. The proof-of-concept model shows that two-dimensional effects are present in the vicinity of the discontinuous plasma potential at the wall, and electron and ion VDFs both clearly exhibit changes due to these effects.

CHAPTER I

Introduction

"Because of collective behavior, a plasma does not tend to conform to external influences; rather, it often behaves as if it had a mind of its own."

– Francis F. Chen, *Introduction to Plasma Physics*

In the present chapter, the general motivation for this dissertation is provided in Section 1.1, states of matter are described in Section 1.2, and the characteristics of a plasma are introduced in Section 1.3. An overview of gas and plasma modeling for different flow regimes is described in Section 1.4, and in Sections 1.5 and 1.6, the plasma discharge device of interest, the Hall effect thruster, is described in detail. Specific research objectives for this thesis are outlined in Section 1.7.

1.1 Motivation

With the increase in computational power in recent years, numerical simulations have become a critical component of engineering applications and to general scientific inquiry. This work explores computational methods related to the modeling of the Hall effect thruster (HET), a spacecraft propulsion device that utilizes plasma for operation. The motivation for this research is multi-fold. From the perspective of basic plasma science, computational models can assist in the collective understanding of the physical processes that govern the behavior of plasmas. Seen through the lens of mathematics and the growing

field of computation, new numerical models may provide insight into the capabilities and limitations of existing models and algorithms presently in use. Finally, from a human perspective, space has captured the collective imagination of humankind. To further explore this final frontier, it is essential to have a deep understanding of the physics that govern modern-day space technologies.

1.2 Matter

All matter consists of atoms, either alone or composed into molecules. In a solid, intermolecular forces are strong relative to the amount of thermal energy, and molecules are closely bound to one another in a fixed volume. Analysis of solids is concerned with stress, strain, deformation, and failure. In a liquid, intermolecular forces are weaker than those in a solid, but molecules are still packed closely together in a fixed volume, and the matter will take the shape of its container. In a gas, intermolecular forces are weaker than those in a liquid, and random molecular motion via collisions may occur. The particles in a gas will spread out or compress to fill the volume they are allowed.

Liquids and gases are both fluids, i.e. substances that continuously deform when subjected to a shear force. When a fluid is in local thermodynamic equilibrium, macroscopic flow properties including density, flow velocity, temperature, and pressure vary slowly in space and over time. Liquids are typically incompressible, dense compared to gases, and almost always exist in local thermodynamic equilibrium. Gases, however, have a fairly large range of densities and levels of collisionality. They can exist in both equilibrium and non-equilibrium states. A plasma is an ionized gas, known in popular literature as the fourth state of matter, and by mass it comprises approximately 99% of the visible universe. [1] It may be partially or completely ionized, i.e. it can consist of both neutral and charged particles or solely the latter.

1.3 Characteristics of a Plasma

Since electrons have a much larger mobility than other species in a plasma due to their small mass, they arrange themselves to shield out external electric fields. The Debye length, λ_D, measures the scale of the charge imbalance in a plasma and is described by:

$$\lambda_D = \sqrt{\frac{\epsilon_0 k_b T_e}{e^2 n_e}} \tag{1.1}$$

where ϵ_0 is the vacuum permittivity, k_b is Boltzmann's constant, e is the elementary charge, n_e is the electron number density, and T_e is the electron temperature. Note that e is always taken as a positive value in this work.

λ_D can be derived by considering a one-dimensional plasma of density n_0 subjected to an applied potential such that $\phi(x = 0) = \phi_0$. To compute $\phi(x)$, assuming ions are singly charged, the Poisson equation is solved. The one-dimensional Poisson equation is described by:

$$\nabla^2 \phi = \frac{d^2\phi}{dx^2} = -\frac{e(n_i - n_e)}{\epsilon_0} \tag{1.2}$$

Assuming that the perturbation due to the applied potential occurs on the time scale of electrons, which is much smaller than the ion time scale, the ion density will remain unperturbed, i.e. $n_i = n_0$. In the presence of potential energy, $-e\phi$, the electron distribution function, $f_e(v_x)$, is:

$$f_e(v_x) = A \exp\left(\frac{-\frac{1}{2}m_e v_x^2 - e\phi}{k_b T_e}\right) \tag{1.3}$$

where A is a constant. Integrating $f_e(v_x)$ over v_x, the *Boltzmann relation* is obtained:

$$n_e = n_0 \exp\left(\frac{e\phi}{k_b T_e}\right) \tag{1.4}$$

Substituting Eq. (1.4) into Eq. (1.2) and expanding the potential in a Taylor series results in the following relationship:

$$\frac{d^2\phi}{dx^2} = \frac{en_0}{\epsilon_0}\left[\exp\left(\frac{e\phi}{k_b T_e}\right) - 1\right] = \frac{e^2 n_0}{\epsilon_0 k_b T_e}\phi \tag{1.5}$$

The solution to Eq. (1.5) corresponds to:

$$\phi = \phi_0 \exp\left(-\frac{|x|}{\lambda_D}\right) \tag{1.6}$$

According to Eq. (1.6), when the Debye length is small compared to a representative physical length scale ($\lambda_D \ll (x = L)$), electrical charge imbalances are negligible outside of the Debye sphere, rendering the plasma *quasineutral*. Thus, ion and electron densities are approximately equal ($n_i \approx n_e$) over length scales greater than the plasma Debye length.

Consider a Debye sphere with a radius of λ_D. In an ideal plasma, a Debye sphere must contain a macroscopically large number of particles ($N_D \gg 1$). This is necessary so that a plasma will exhibit *collective* behavior, meaning that long-range interactions between charged particles dominate over binary collisions. Correspondingly, in a collisional plasma, charged particles should not collide so frequently with neutral atoms that their motion is controlled by hydrodynamic forces rather than electromagnetic forces. Therefore, the frequency of a typical plasma oscillation should be large compared to the mean time between particle collisions, i.e. $\omega\tau > 1$, where ω is the plasma frequency and τ is the mean time between particle collisions.

1.4 Overview of Gas and Plasma Modeling

The basis for all dilute gas dynamics is the Boltzmann equation which in its general form is given as:

$$\frac{\partial f}{\partial t} + \mathbf{v}\frac{\partial f}{\partial \mathbf{z}} + \mathbf{a}\frac{\partial f}{\partial \mathbf{v}} = S_{boltz} \tag{1.7}$$

Eq. (1.7) states that the velocity distribution function, f, evolves in time, t, physical space, $\mathbf{z}$, and velocity space, $\mathbf{v}$. S_{boltz} on the right hand side of Eq. (1.7) is a collision term due to two-particle interactions. Elastic collisions are described by the Boltzmann collision integral, which is given by:

$$S_{boltz} = \int\int g\sigma(f_A^{'}f_B^{'} - f_A f_B)d\Omega d\mathbf{v} \tag{1.8}$$

where subscripts A and B denote the colliding particles, $g = |\mathbf{v}_B - \mathbf{v}_A|$ is the relative speed between particles A and B, $\sigma d\Omega$ is the differential cross section where $d\Omega$ is the solid angle, and superscript $'$ denotes information after the collision event. [2]

The Boltzmann equation is derived from the more general Liouville equation, which describes the time evolution of the phase space distribution function for a system of N particles. The derivation of the Boltzmann equation is described in detail in Reference [3]. Two of the primary assumptions for this derivation include: (1) that the collision integral, S_{boltz}, considers only binary collisions and (2) that the velocities of two colliding particles are not correlated with each other. With these assumptions, the Liouville equation can be transformed into a chain of equations consisting of multiple particle distribution functions known as the Bogoliubov Born Green Kirkwood Yvon (BBGKY) hierarchy, and the truncated BBGKY hierarchy may then be used to obtain the Boltzmann equation. The Boltzmann equation is challenging to solve, both analytically and computationally, so simplifications are made when possible. Note that other types of collision models may be

incorporated into Eq. (1.7). For example, ionization processes may be taken into account by applying an ion source term, S_{ion}:

$$S_{ion} = \nu_{ion} f_{neutral} \tag{1.9}$$

where ν_{ion} is the ionization frequency and $f_{neutral}$ is the distribution function for neutral atoms. The Fokker-Planck collision model provides another important collision integral for fully-ionized plasma physics applications, as the model takes into account binary elastic collisions between charged particles known as Coulomb interactions. [4]

1.4.1 Knudsen Number

The Knudsen number (Kn) is a dimensionless parameter that describes the level of non-equilibrium of a gas flow and is defined as the ratio of the mean free path, λ_{mfp}, to a representative physical length scale, L:

$$Kn = \frac{\lambda_{mfp}}{L} \tag{1.10}$$

Whether the flow is collisional or collisionless is determined by the value of the Knudsen number. If the Knudsen number is much smaller than unity, the flow is collisional. If there are a significant number of elastic collision events without any inelastic collision events, the gas particles relax to a Maxwell-Boltzmann velocity distribution, also known as a *Maxwellian* distribution. Such a gas is in the continuum regime, meaning that the frequency of intermolecular collisions inside the sampling volume is high, and thermodynamic equilibrium can be established. In the continuum regime, macroscopic flow properties vary continuously from point to point in the flow, and the conservation equations for mass, momentum, and energy can be solved using macroscopic approaches. If $Kn \to \infty$, the gas is in the free molecular flow regime, i.e. the flow is collisionless. For an intermediate Knudsen number ($0.01 < Kn < 1$), the flow is in a transitional, non-equilibrium state,

and it is necessary to consider the non-Maxwellian nature of the gas. Modeling techniques for these different regimes are discussed in Sections 1.4.2-1.4.4.

1.4.2 Near-Equilibrium Gas Dynamics Models

For a non-ionized gas with a small Knudsen number, numerical models often make the assumption that the flow relaxes to a Maxwellian distribution. In this regime, it is appropriate to derive partial differential equations (PDEs) to model gas flows by taking moments of the Boltzmann equation (Eq. (1.7)). Perhaps the most widely used sets of equations are the Euler equations and the Navier-Stokes equations (discussed in various texts including References [2] and [5]). The Euler equations for adiabatic, inviscid flows are derived assuming that gas particles relax to a Maxwellian distribution. The Euler equations consist of a set of five PDEs and can be used to analyze certain aspects of incompressible and compressible flow fields including, for example, the lift generated over a thin airfoil at a small angle of attack or the properties across a steady shock wave. The Navier-Stokes equations consist of twenty PDEs involving heat flux and shear stress tensors and are derived by assuming a relaxation toward an equilibrium distribution and performing the Chapman-Enskog perturbation expansion under the assumption of a short relaxation time. [2, 6]

As $Kn \rightarrow \infty$, free molecular flow analysis may be used. The flow is collisionless, so the collision integral in Eq. (1.7) goes to zero, and the free molecular gas stream is characterized by a Maxwellian velocity distribution function (VDF). Therefore, it is possible to calculate fluxes of properties such as mass, momentum, and energy when the flow field encounters a surface, such as a spacecraft, and to analyze the effects of the flow field on the vehicle. When the Knudsen number is in the transitional regime, it is necessary to use a numerical method that allows for the analysis of strongly non-equilibrium flows. The approaches for modeling gas dynamics in this regime are discussed in Section 1.4.4.

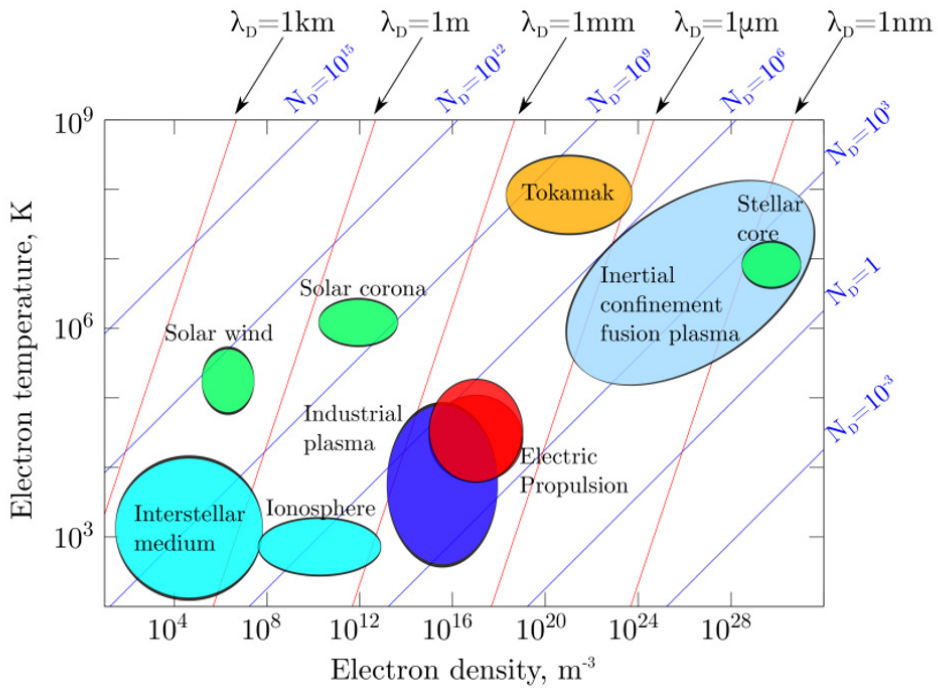

Figure 1.1: Summary of various plasmas for a wide range of densities and temperatures. Image reproduced from Reference [7].

1.4.3 Near-Equilibrium Plasma Dynamics Models

For plasmas, the Boltzmann equation is coupled with Maxwell's equations, which are described in Chapter II, to account for electric and magnetic fields in the medium. As shown in Fig. 1.1, plasmas span a variety of length scales, densities, and temperatures. The two main near-equilibrium models of plasma dynamics are two-fluid theory and magnetohydrodynamics (MHD). Two-fluid theory approximates a plasma as "mutually interacting, finite-pressure electron and ion fluids" [8]. This approach requires that particles conform to Maxwellian VDFs, which is true only if there are sufficient collisions present or if there is another randomizing process in place that allows for this assumption. This last point is important, since two-fluid equations have been utilized successfully to model some weakly collisional and collisionless plasmas. A partial justification for its use in these cases is that a strong magnetic field can play the role of collisions by forcing particles to gyrate in a Larmor orbit that is much smaller than the particle mean free

path. Some phenomena that have been successfully modeled using the two-fluid approach include Alfvèn waves relevant to the solar corona and fast magnetic reconnection in solar flares. [9] The MHD model approximates a plasma as a single, finite-pressure, electrically-conducting fluid. Essentially, the two-fluid equations are combined to describe a single, center-of-mass fluid with a relative drift motion between the fluids. The MHD approach has been used in cosmic electrodynamics, fusion, and other areas. [10]

1.4.4 Non-Equilibrium and Hybrid Modeling Techniques

For both non-ionized gases and for plasmas, the non-equilibrium flow regime requires an approach which can account for the departure from local thermodynamic equilibrium (LTE). One of the most popular techniques for non-ionized gases is the direct simulation Monte Carlo (DSMC) approach. Developed by Bird in in the 1960s, the DSMC approach is a stochastic method that emulates the physics of the Boltzmann equation. [11] The DSMC approach necessitates the creation of particles, for which the equations of motion are solved, and collisions are accounted for in a stochastic fashion. A simulated particle does not represent a single real particle but rather a *macroparticle*, or a collection of of identical real molecules. Thus, the technique does not simulate every real molecule, and the deterministic nature of molecular movement and collisions cannot be retained below the scale of a computational cell size. [2]

Analogous to the DSMC technique for neutral gases is the electrostatic particle-in-cell (PIC) method which can be used to simulate the motion of plasma in the presence of an electric field. Throughout this work, the term *PIC* will be used to refer to the solution technique for the motion of both non-ionized and ionized gases. The term *DSMC* will be reserved for the collision technique associated with the DSMC approach. Often, the PIC technique is used in plasma physics to model the collisionless Boltzmann, or Vlasov equation. Examples of applications for which Vlasov theory may be applied include collisionless sheaths (discussed in Chapter VI) and Landau damping, which is collisionless

damping of plasma waves. Landau damping can occur for both electrons and ions; ion acoustic waves, for instance, can be greatly affected by Landau damping. [10] Collisional forms of the kinetic equation are also commonly modeled using the PIC technique.

In lieu of the stochastic PIC technique, a deterministic direct kinetic (DK) method can also be utilized to simulate the motion of non-ionized gases and plasmas. This method resolves the Boltzmann or Vlasov equations in discretized phase space by evaluating the grid-based VDFs as they evolve over time, and its implementation is the bulk of the present work. The primary advantage of the DK method compared to the PIC method is that there is no statistical noise in the DK algorithm. [12] In recent years, one-dimensional DK methods have been used to model plasma sheaths [12, 13, 14], HET channel physics [15], mode transitions in HETs [16], and ion acoustic turbulence in a cathode plume. [17] Two-dimensional and axisymmetric DK methods have been applied to the axial-azimuthal geometry of a HET [18], to hollow cathode plasmas [19], and, as described in this work, to axial-radial HET geometries. [20] A full discussion of the DK method is provided in Chapter II.

Depending on the application, a combination of modeling techniques can be beneficial. In applications where ions and electrons are in different regimes, a hybrid approach may be appropriate. In the present work related to a HET, ions and neutral particles are modeled using kinetic (DK and PIC) techniques while electrons are considered to be a fluid. The hybrid numerical techniques utilized in this work are discussed at length in Chapter III.

1.5 In-Space Propulsion Systems

An overview of numerical modeling has been provided in previous sections. Now, it is necessary to introduce the primary object of numerical modeling in this work: the Hall thruster, a type of space propulsion device. Simply stated, the objective of a space propulsion device is to move its host vehicle. A specific propulsion system is often designed for

a unique purpose. For example, a launch from Earth's surface requires much more thrust than an orbit transfer, and it is more efficient that different propulsion systems be utilized for these two purposes. According to Newton's second law, the rate of change in time of an object's momentum, $\mathbf{p}$, is equal to the sum of the external forces, $\mathbf{F}_{ext}$, acting on that object:

$$\mathbf{F}_{ext} = \frac{d\mathbf{p}}{dt} = \frac{d(m\mathbf{v})}{dt} \qquad \text{Newton's second law} \tag{1.11}$$

where m is the mass of the object and $\mathbf{v}$ is its velocity. Assuming that a space vehicle operates in total vacuum, i.e. that external gravitational and frictional forces acting on the vehicle are negligible, then $\mathbf{F}_{ext} = 0$.

If the mass flow rate of the propellant, $\frac{dm}{dt} = \dot{m}$, and its exit velocity, $\mathbf{u}_e$, are also constant and uniform, then Eq. (1.11) can be rewritten as:

$$m\frac{d\mathbf{v}}{dt} = -\dot{m}u_e \tag{1.12}$$

where the negative sign indicates that mass is ejected from the vehicle in the direction opposite to the vehicle's motion. Integrating Eq. (1.12) from the initial state of the rocket at time t_i, to a state sometime later at time t_f, it is found that:

$$\frac{m_f}{m_i} = \exp\left(\frac{-\Delta v}{u_e}\right) = \exp\left(\frac{-\Delta v}{gI_{sp}}\right) \tag{1.13}$$

where Δv represents the velocity change for a maneuver of interest between times t_i and t_f. Over the course of a space vehicle's mission, Δv can also represent the sum of all changes in velocity. $I_{sp} = \frac{u_e}{g} = \frac{F_{th}}{\dot{m}g}$ describes the thrust provided by the fuel, relative to the weight-use-rate of the fuel. Eq. (1.13) states that, to achieve a high Δv during a maneuver, either the fuel consumption, i.e. the resultant change in mass, or the specific impulse must be high. A high specific impulse (Isp) is indicative of an efficient maneuver that minimizes the

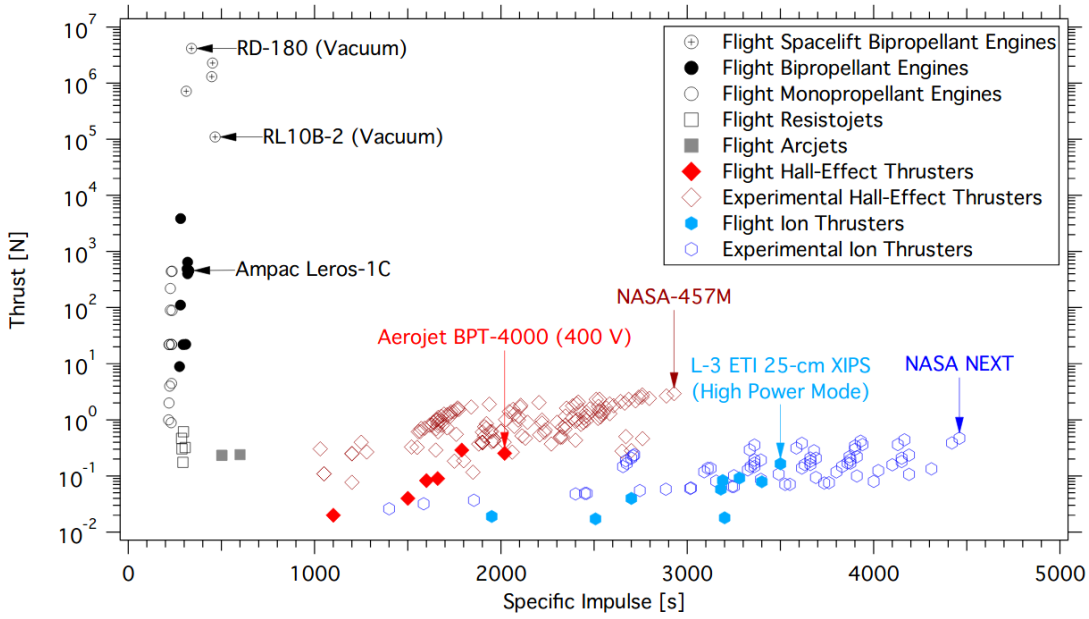

Figure 1.2: Thrust and specific impulse of various chemical and electric space propulsion devices. Figure reproduced from Reference [21]

propellant mass, thereby maximizing the allowable mass of non-propellant cargo on board the space vehicle, known as the payload. The thrust and specific impulse values of various chemical and electric space vehicles are displayed in Fig. 1.2. Chemical propulsion devices (displayed in the figure as bipropellant and monopropellant engines) typically consume a relatively large amount of fuel, display low levels of Isp and relatively high levels of thrust. Electric propulsion devices, described in Section 1.5.1, typically display higher levels of Isp and lower levels of thrust in comparison to their chemical counterparts.

1.5.1 Electric Propulsion

EP devices produce thrust by utilizing electrical energy to generate high exit velocities for the propellant molecules, thereby using relatively little fuel by mass to achieve a particular thrust level compared to conventional types of propulsion. Typical EP systems are described briefly below.

1. *Electrothermal* devices include resistojets and arcjets. Propellant is heated via an

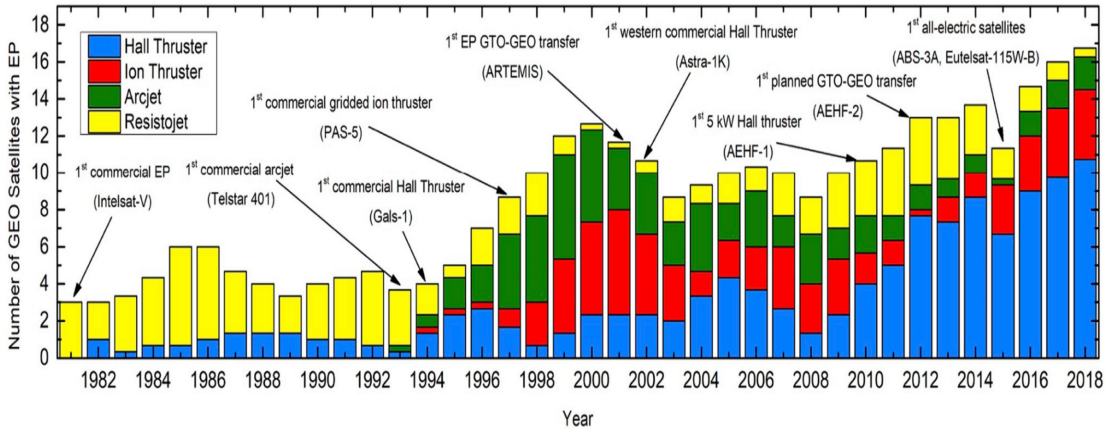

Figure 1.3: Number of EP-based GEO satellites launched in the years 1981 through 2018 (3-year moving average), divided into electric thruster subclasses. Image reproduced from Reference [22].

electrical source prior to entering a nozzle, where it is thermally expanded.

2. *Electromagnetic* devices include the pulsed plasma thruster (PPT) and the magnetoplasmadynamic (MPD) thruster. These devices utilize the interaction of time-varying electric and magnetic fields to ionize and accelerate particles.
3. *Electrostatic* thrusters include Hall effect thrusters and ion thrusters. The propellant gas is first ionized and then accelerated out of the thruster via an applied electric field.

A breakdown of the present-day usage of common EP devices is shown in Fig. 1.3. Overall, the total usage of EP systems for flight continues to grow, and presently, HETs make up well over half of the EP systems currently launched on GEO satellites.

1.6 Hall Effect Thrusters

A HET is a space propulsion device typically used for applications including satellite station keeping and orbit raising maneuvers. A schematic of a typical, single-channel HET is shown in Fig. 1.4. In a standard configuration, the thruster operates at nominal power levels of 1.5-4.5 kW and generates relatively high Isp (1500-2000 s) and thrust levels on the

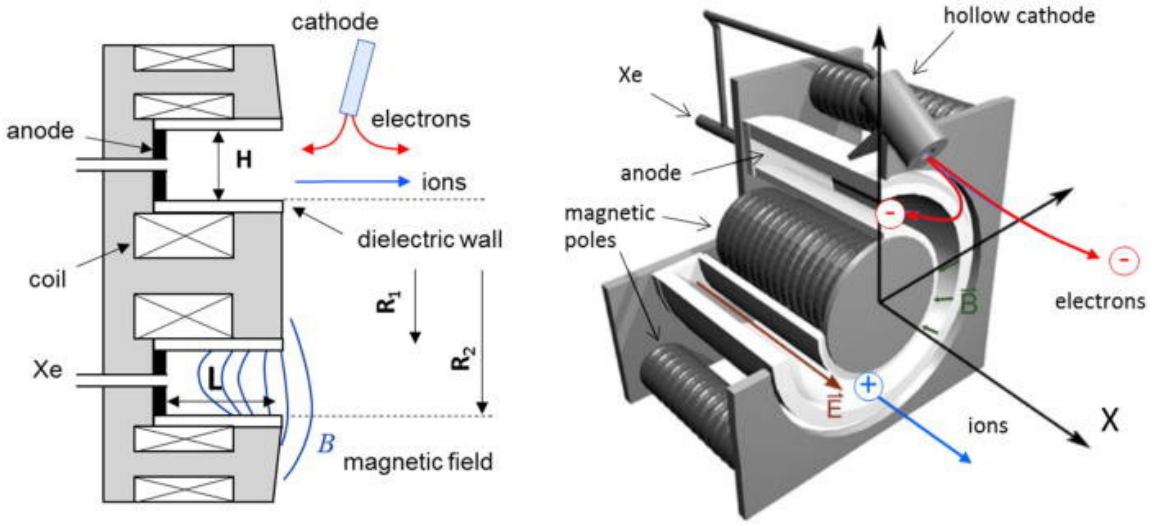

Figure 1.4: Schematic of a Hall effect thruster. (Left) two-dimensional side view of a thruster, and (right) three-dimensional cross section of a thruster. Image reproduced from Reference [25].

order of 100 mN. [23] The first HET was a stationary plasma thruster (SPT), developed in the then Soviet Union in the late 1960s, and it was launched in 1971 on board the satellite *Meteor-18*. [24] Another type of HET is the thruster with anode layer (TAL). The primary difference between the two models is that the TAL has metallic walls and contains a shorter channel than the SPT, whose longer channel walls are typically composed of an insulator material such as boron nitride.

HETs have advanced significantly since the 1970s, and their development continues yet today. To combat the high rate of erosion at thruster channel walls, magnetically-shielded thrusters were constructed. [26] Today, thrusters are being scaled from their traditional power levels to both higher (100 kW+) and lower levels (<100 W) of power. [27, 28] When these new configurations become available for flight, the breadth of applicability of the HET may increase greatly to include missions for small satellites such as cubesats as well as larger vehicles for deep space missions.

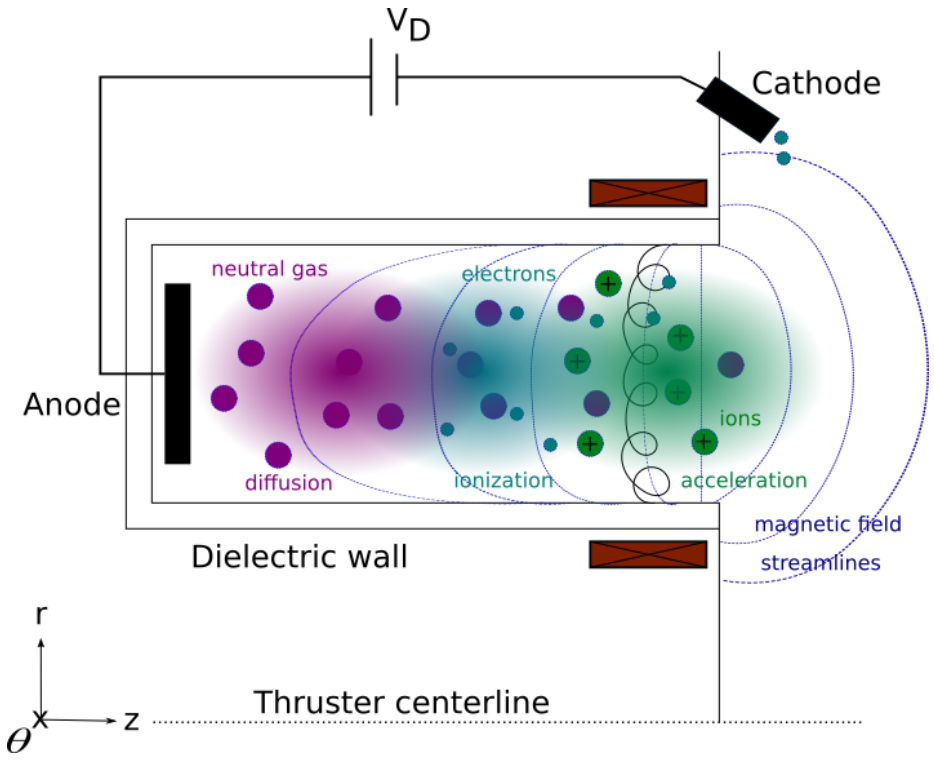

Figure 1.5: Cross section of Hall effect thruster channel.

1.6.1 Hall Effect Thruster Operating Principles

The HET is an electrostatic accelerator that utilizes the Hall effect to confine electrons and a large electric field to accelerate ions and generate thrust. A schematic of a HET channel cross section is shown in Fig. 1.5. The device contains either electromagnets or permanent magnets that create a primarily radial magnetic field inside the thruster channel and its near-field plume. Typical nominal operating conditions for Fakel's SPT100M, an HET in the kW range, are displayed in Table 1.1. For operation, a noble gas such as xenon is injected at the anode-side of the thruster, and electrons are emitted into the flowfield via an external cathode which lies downstream of the thruster. An electric potential difference is applied between the anode and the cathode, with ground taken such that the anode potential is positively biased by several hundred volts, and the cathode potential is slightly negative.

The gyroradius or Larmor radius, r_L, describes the radius of the circular motion of a

Table 1.1: Typical operating conditions and orders of magnitude for a Hall thruster in the kW range (Fakel SPT100M). Values obtained from Reference [25].

Parameter	Value
Channel length, L	2.5 cm
Inner channel radius, R_1	3.5 cm
Outer channel radius, R_2	5.0 cm
Discharge current, I_D	4.5 A
Discharge voltage, V_D	300 V
Power, P_D	1350 W
Xenon mass flow rate, $\dot{m}$	5.3 mg/s
Thrust, T	90.2 mN
Specific impulse, Isp	1734 s
Mean velocity of ion beam, $V_{i,b}$	17 km/s

charged particle in the presence of a magnetic field. It is described by:

$$r_L = v_\perp / \omega_B \tag{1.14}$$

where $v_\perp$ is the particle's velocity perpendicular to the magnetic field, and ω_B is the particle's cyclotron frequency. Inside the thruster channel, electron-neutral collisions occur, and positively charged ions are generated via electron-impact ionization. The ions have a large gyroradius compared to the diameter of the channel and therefore remain mostly non-magnetized. Thus, ions are electrostatically accelerated out of the channel. Due to quasineutrality, the axial force density acting on ions due to the electric field (en_eE_z) is equal and opposite to the axial force density acting on electrons. However, electrons have a small gyroradius, and in the presence of a radial magnetic field, they cannot freely accelerate toward the anode. Instead, they drift in the azimuthal direction, thereby generating an axial magnetic field force density on themselves due to the interaction of the azimuthal current density and the radial magnetic field ($j_{e,\theta} \times B_r$), where $j_{e,\theta}$ is known as the Hall

current. This force density is approximately equal and opposite to the electrostatic force density acting on the electrons; therefore, electron motion toward the anode is impeded by the magnetic field. The measure of electron confinement due to the magnetic field is described by the Hall parameter, Ω, which is the ratio of the electron cyclotron frequency to the electron momentum transfer frequency, ν_m:

$$\Omega = \omega_{B,e}/\nu_m \tag{1.15}$$

Ω is typically much larger than unity in a HET, indicating that electrons are at least partially confined, resulting in a favorable probability of ionization collisions with neutral atoms.

In Fig. 1.5, three overlapping regions are shown (not to scale) to portray the major processes that occur inside the discharge channel of a typical HET. Near the anode, electron diffusion is high, and the magnetic field is low. Neglecting the anode sheath, which may span a few Debye lengths near the anode surface, the electric field is also typically small in the near-anode region. Near the exit of the thruster channel, the electric and magnetic fields are large, ionization occurs, and ions are accelerated out of the channel to generate thrust.

1.6.2 Hall Thruster Challenges

Ultimately, the goal of developing HETs from an engineering perspective is to improve metrics such as thruster performance, efficiency, and lifetime. However, there are several fundamental, unknown aspects related to their operation. Together with experimental and theoretical work, modeling efforts may lead to a better understanding of these fundamental questions. Although not intended to be an exhaustive review, this section outlines some of the aspects of HETs that affect the device's key metrics including performance, efficiency, and lifetime. Comprehensive reviews of HET physics as well as research efforts devoted to modeling can be found in the literature by Boeuf [25], Goebel and Katz [23], and Hara

[29], among others.

Thruster performance and stability are affected by a wide range of plasma oscillations, ranging from narrow-band, coherent waves to broadband turbulence (1 kHz-50 MHz). [30] Perhaps most ubiquitous to thruster operation is the "breathing mode", a low frequency global oscillation ranging from 15-35 kHz that results in a global depletion and replenishment of neutral particles and can vary significantly in amplitude, depending on the operating condition. [31] The azimuthal spoke oscillation, also a part of the low frequency band, is associated with a perturbed azimuthal electric field and density that are observed to oscillate in-phase with a rotating spoke. [32] The electron cyclotron drift instability (ECDI), implicated in electron heating and possibly related to anomalous transport, is an azimuthal mode associated with an electron density fluctuation and lies in the MHz frequency range. [33] The high frequency band is associated with both transient-time oscillations and Rayleigh-type instabilities. [34]

Thruster efficiency, $\eta = Tv_e/P_{in}$, where P_{in} is the input power, is largely determined by the ionization and acceleration processes, and these processes are primarily dictated by electron transport. Non-classical, cross-field electron transport, often called *anomalous electron transport*, affects the mobility of electrons in the thruster and has been qualitatively attributed to phenomena including wall collisionality and plasma turbulence. [35] Electron transport is the subject of a large body of past and current research. For example, theoretical and modeling efforts have recently focused on investigating ECDI as a source for anomalous transport. [36] Recent experimental evidence suggests that electron transport is directly correlated with the breathing mode; that is, transport profiles indicate that the anomalous collision frequency fluctuates by several orders of magnitude over the course of a breathing cycle; [37] and it has been suggested via experimental evidence that the increase in neutral particles due to the finite background pressure in a vacuum test chamber shifts the location of the acceleration zone, resulting in different thruster behavior on orbit compared to ground testing, but the reason for this has not yet been established from first

principles. [38]

The service lifetime of the HET has historically been limited by high rates of erosion at the thruster channel walls, implying that plasma-wall interactions are very important in these devices. [39] Due to magnetic shielding in newer thruster configurations, erosion of the channel walls has been significantly reduced since the electric field intensity near the walls is lowered, reducing ion bombardment. [40] However, recent studies show that the movement of the acceleration zone in magnetically shielded thrusters compared to standard configurations may result in additional erosion of thruster pole pieces since the movement of the potential contours at the edge of the plasma beam allow for high energy ions to be accelerated radially toward the pole pieces. [41] Thus, plasma-wall interactions continue to be an area of interest and importance for the HET.

High fidelity computational models are useful to investigate the physical processes that affect a thruster's performance, efficiency, and lifetime limitations. The non-equilibrium nature of the plasma transport should be resolved so that the flow can be accurately characterized. The primary purpose of the present work is to apply a two-dimensional, deterministic, direct kinetic algorithm to a HET simulation and investigate its ability to capture complex phenomena compared to a state-of-the art PIC simulation.

1.7 Research Objectives

The goal of this work is to improve the state-of-the art modeling approach for the Hall effect thruster and to understand the capabilities and limitations of the utilized modeling techniques. To that end, the following objectives are met in in this work:

- Development of a two-dimensional, hybrid-DK simulation of a Hall thruster channel and its near-field plume.
- Development of conservative kinetic boundary conditions for particle-wall collisions in the thruster channel and at the pole pieces.

- Analysis of injection boundary conditions in the DK simulation.
- Modification and additional development of a two-dimensional, hybrid-PIC simulation, including a study on the limitations of the Monte Carlo collision (MCC) algorithm.
- Development of an anode boundary condition within the electron fluid simulation framework.
- Benchmarking of the developed hybrid-DK simulation with a comparable hybrid-PIC simulation, modeling the UM/AFRL P5 Hall thruster.

Relevant to the DK numerical method as well as Hall effect thrusters but distinct from full HET modeling, a preliminary two-dimensional DK plasma sheath model is also introduced. Objectives include:

- Development of conservative kinetic boundary conditions, particularly at the plasma injection site.
- Development, verification, and implementation of a two-dimensional DK plasma sheath simulation.

The thesis is set up as follows. Chapter II describes the equations that govern the physics of the discharge plasma in a Hall thruster channel and near-field plume. Chapter III describes the numerical techniques that are utilized to implement the governing equations in hybrid-DK and hybrid-PIC simulations. Chapter IV describes the development of conservative boundary conditions for the two-dimension DK algorithm. Chapter V presents results for the benchmarking effort, and limitations are discussed for both the DK and PIC techniques. In Chapter VI, results for a fully two-dimensional, collisionless plasma sheath are presented. Finally, in Chapter VII, conclusions and future work are discussed.

CHAPTER II

Governing Equations

"Plasma physics is usually not a precise science. It is rather a web of overlapping points of view, each modeling a limited range of behavior. Understanding of plasmas is developed by studying these various points of view, all while keeping in mind the linkages between the points of view."

– Paul M. Bellan, *Fundamentals of Plasma Physics*

This chapter is concerned with the equations that govern the physics of the discharge plasma in a Hall effect thruster channel and near-field plume. This work models a HET in two (z, r) spatial dimensions. As shown in Fig. 1.1 of Chapter I, the Debye length in a HET is on the order of 1 μm - 0.1 mm. Because the plasma Debye length is small compared to the spatial resolution achieved with the numerical model in this study, the quasineutral approximation is used, i.e. $n_e = Zn_i$, where Z is the degree of ionization. The HET magnetic field configuration and its relationship to the electron simulation grid is described in Section 2.1. The fluid electron equations are detailed in Section 2.2, and the kinetic equations that govern more massive ions and neutral particles are discussed in Section 2.3. Current conservation in the device is detailed in Section 2.4, and particle collisions and electron transport are described in Section 2.5 and Section 2.6, respectively. Details regarding the numerical implementation of the governing equations via the DK and PIC methods are described in Chapter III.

2.1 Magnetic field

To sufficiently confine electrons inside the thruster channel, the magnetic field in a HET is optimized via a combination of electromagnets both internal and external to the device. The magnetic field, $\mathbf{B}$, is governed by Maxwell's equations, which in differential form are described by the following expressions:

$$\nabla \cdot \mathbf{B} = 0 \qquad \text{Gauss' Law for Magnetism} \tag{2.1a}$$

$$\nabla \times \mathbf{B} = \mu_0 \left(\mathbf{j} + \epsilon_0 \frac{\partial \mathbf{E}}{\partial t} \right) \qquad \text{Ampère's Law} \tag{2.1b}$$

where μ_0 is the vacuum permeability and $\mathbf{j}$ is the current density. Eq. (2.1a) states that the divergence of the magnetic field is zero everywhere. Because the field is divergence-free, a magnetic field stream function, λ, that is perpendicular to $\mathbf{B}$ may be constructed. One such possible stream function corresponds to:

$$\frac{\partial \lambda}{\partial r} = r B_z \tag{2.2a}$$

$$\frac{\partial \lambda}{\partial z} = -r B_r \tag{2.2b}$$

where z and r denote the axial and radial directions, respectively. The magnetic field stream function is important for the construction of a quasi-one dimensional electron fluid solver, as the magnetic field streamlines make up the electron grid. As will be described in Section 2.2, electron motion perpendicular to the magnetic field is important. Therefore, it is necessary to calculate the normal derivative to the magnetic field streamlines, $\frac{\partial}{\partial \hat{n}}$, which

is described by:

$$\frac{\partial}{\partial \hat{n}} = \frac{\partial}{\partial \lambda}\frac{\partial \lambda}{\partial \hat{n}} = \frac{\partial}{\partial \lambda}\nabla\lambda \tag{2.3}$$

The vector normal to $\mathbf{B}$ is described by $\hat{n}$:

$$\hat{n} = \frac{B_z}{B}\hat{r} - \frac{B_r}{B}\hat{z} \tag{2.4}$$

and the gradient of λ is:

$$\nabla\lambda = \frac{\partial \lambda}{\partial r}\hat{r} + \frac{\partial \lambda}{\partial z}\hat{z} = rB_z\hat{r} - rB_r\hat{z} \tag{2.5}$$

Combining Eq. (2.4) and Eq. (2.5), Eq. (2.3) can be recast as:

$$\frac{\partial}{\partial \hat{n}} = rB\frac{\partial}{\partial \lambda}\hat{n} \tag{2.6}$$

If variations in the magnetic field due to plasma currents and dynamic electric fields are assumed to be small compared to the field produced by the electromagnets, Ampère's law (Eq. (2.1b)) reduces to:

$$\nabla \times \mathbf{B} = 0 \tag{2.7}$$

This is a reasonable assumption in a HET, since $\mu_0\left(\mathbf{j} + \epsilon_0\frac{\partial \mathbf{E}}{\partial t}\right) \approx 0.02$ T/m which is small compared to magnetic field gradients due to electromagnetics (≈ 0.5 T/m). [42] Therefore, a magnetic potential function, σ, exists such that

$$\mathbf{B} = \nabla\sigma \tag{2.8}$$

and Laplace's equation must be satisfied in the plasma region, namely:

$$\frac{\partial^2 \sigma}{\partial z^2} + \frac{\partial^2 \sigma}{\partial r^2} + \frac{1}{r}\frac{\partial \sigma}{\partial r} = 0 \tag{2.9}$$

The relationship between $\mathbf{B}$, σ, and λ is described by:

$$B_z = \frac{1}{r}\frac{\partial \lambda}{\partial r} = \frac{\partial \sigma}{\partial z} \tag{2.10a}$$

$$B_r = -\frac{1}{r}\frac{\partial \lambda}{\partial z} = -\frac{\partial \sigma}{\partial r} \tag{2.10b}$$

If sufficient boundary information is available, the vacuum magnetic field can be numerically obtained by solving Laplace's equation (Eq. (2.9)). If measured magnetic field data is provided, it is possible to check how much the field varies from a vacuum condition by determining the deviation from zero for the following expression:

$$\nabla \times \mathbf{B} = \left(\frac{\partial B_r}{\partial z} - \frac{\partial B_z}{\partial r} \right) \hat{\theta} \tag{2.11}$$

The magnetic field is assumed to be static for the purposes of the HET simulation ($\frac{\partial \mathbf{B}}{\partial t} = 0$). A typical magnetic field configuration for a SPT is shown in Fig. 2.1. Both the two-dimensional field configuration for an axial-radial thruster cross section as well as the radial magnetic field magnitude along the thruster channel centerline are displayed. Note that the Hall parameter is typically largest near the thruster channel exit, where the radial magnetic field is the largest, indicating that electron confinement is also high at that location.

2.2 Electrons

Since their characteristic time scale is much smaller than that of ions due to the large difference in mass, electrons are considered to be at steady state on the time scale of ions.

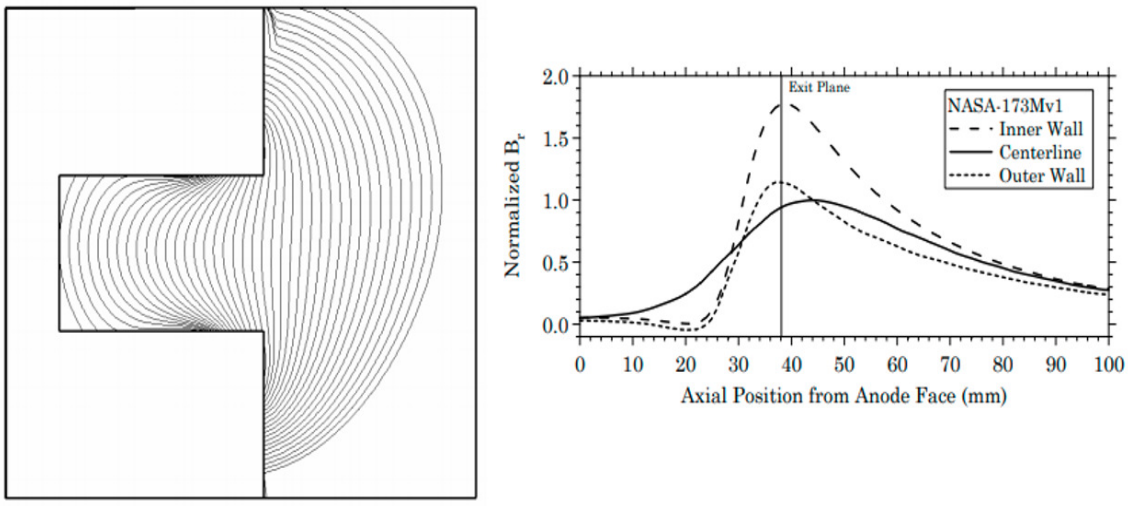

Figure 2.1: Typical magnetic field configuration in a Hall thruster. On the left, experimentally-obtained magnetic field lines are shown in z-r geometry. On the right, the radial magnetic field for the NASA-173Mv1 thruster is shown as a function of axial position from the anode. Image reproduced from Reference [43].

Along a magnetic field streamline, thermal equilibrium of confined electrons is assumed, allowing for the approximation of constant electron temperature. Assuming a Maxwellian distribution for electrons and an isotropic pressure, a quasi-one-dimensional fluid electron algorithm, similar to the approaches used by Koo and Boyd, Fife, and Hagelaar *et al*, is employed. [44, 42, 45]

The conservation of mass, momentum, and energy must be satisfied in the fluid approach. The conservation equations are derived by taking moments of the kinetic equation for electrons (Eq. (1.7)). In their general form, the fluid conservation equations are described by:

$$\frac{\partial n}{\partial t} + \nabla \cdot (n\mathbf{u}) = \dot{n} \tag{2.12}$$

$$\frac{\partial (mn\mathbf{u})}{\partial t} + \nabla \cdot (mn\mathbf{u}\mathbf{u} + \overline{\overline{P}}) = qn(\mathbf{E} + \mathbf{u} \times \mathbf{B}) + \mathbf{R} \tag{2.13}$$

$$\frac{\partial(n\epsilon)}{\partial t} + \nabla \cdot (n\epsilon \mathbf{u} + \mathbf{u} \cdot \overline{\overline{P}} + \mathbf{q}) = \mathbf{j} \cdot \mathbf{E} - \Lambda \tag{2.14}$$

where $\mathbf{u}$ is the bulk velocity, $\dot{n}$ is the particle production and loss rate, $\overline{\overline{P}}$ is the pressure tensor, $\mathbf{R}$ is the momentum change due to collisions and shear forces, ϵ is the total energy, $\mathbf{q}$ is the conductive heat flux, and Λ is the energy loss due to elastic and inelastic collisions.

2.2.1 Electron Momentum Perpendicular to the Magnetic Field

Across lines of force, i.e. perpendicular to magnetic field streamlines, the force balance on electrons is described by the one-dimensional generalized Ohm's Law, also known as the drift-diffusion approximation. [29] This approximation assumes that the time-varying evolution of physical phenomena is slow compared to low-frequency plasma structures on the order of the ion and neutral motion. Additionally, the inertia term is neglected, an appropriate assumption when the bulk velocity is much smaller than the thermal velocity. These assumptions are valid provided that high-frequency instabilities on the order of the electron time scales are negligible. The momentum transfer term in Eq. (2.13) is assumed to follow $\mathbf{R} = -mn\nu_m(\mathbf{u} - \mathbf{u}_k)$, where ν_m is the momentum transfer collision frequency. The bulk velocity of the other species involved in the collision event, $\mathbf{u}_k \approx 0$. Assuming an isotropic pressure and applying the ideal gas law, the electron current density can be written from Eq. (2.13) as:

$$j_{e,\perp} = en_e u_{e,\perp} = en_e\mu \left(E_\perp - \frac{1}{en_e} \nabla_\perp p_e \right) = \underbrace{en_e\mu E_\perp}_{\text{drift}} - \underbrace{\frac{eD}{k_b T_e} \nabla_\perp p_e}_{\text{diffusion}} \tag{2.15}$$

where μ is the mobility and D is the diffusivity. Furthermore, the pressure, p_e is described by:

$$p_e = n_e k_b T_e \tag{2.16}$$

where T_e is the electron temperature. The electric field, $E_\perp$, is simply the gradient of the potential:

$$E_\perp = -\frac{\partial \phi}{\partial \hat{n}} \tag{2.17}$$

The classical electron conductivity across magnetic field lines, $\sigma_\perp$, is described by:

$$\sigma_\perp = \frac{e}{m_e \nu_m} \frac{1}{1+\Omega^2} \tag{2.18}$$

where m_e is the electron mass. The mobility is related to the conductivity via:

$$\sigma = e n_e \mu \tag{2.19}$$

and the diffusivity, D_m, and the mobility are related by the Einstein relation:

$$\frac{D_m}{\mu} = \frac{k_b T_e}{e} \tag{2.20}$$

Therefore, Eq. (2.15) becomes:

$$j_{e,\perp} = \sigma \left(-\frac{\partial \phi}{\partial \hat{n}} + \frac{1}{e n_e} \frac{\partial}{\partial \hat{n}} (n_e k_b T_e) \right) \tag{2.21}$$

Using Eq. (2.6), Eq. (2.21) can be rewritten so that the derivatives are taken with respect to the magnetic field streamlines. However, it is necessary to first consider thermal equilibrium of confined electrons, as described in Section 2.2.2.

2.2.2 Electron Momentum Parallel to the Magnetic Field

The concept of the thermalized potential is one of the most important tenets of the quasi-one-dimensional electron fluid algorithm. Electron dynamics occur very rapidly along magnetic streamlines, and diffusion parallel to the magnetic field is much larger than diffu-

sion perpendicular to it. Thus, using the assumptions from the drift-diffusion approximation, including no friction, Eq. (2.13) reduces to a balance between electric and pressure forces and can be written as:

$$en_e \frac{\partial \phi}{\partial \hat{t}} - \frac{\partial}{\partial \hat{t}}(n_e k_b T_e) = 0 \tag{2.22}$$

where $\hat{t}$ is the direction tangent to the magnetic field streamlines. Since electron dynamics in the parallel direction occur on a timescale much smaller than that in the perpendicular direction, it is assumed that electrons reach thermal equilibrium along magnetic field streamlines very rapidly. Due to this isothermal condition, Eq. (2.22) can be reduced to:

$$en_e \frac{\partial \phi}{\partial \hat{t}} = k_b T_e \frac{\partial n_e}{\partial \hat{t}} \tag{2.23}$$

Eq. (2.23) can be integrated with respect to λ to obtain:

$$\phi^*(\lambda) = \phi(\lambda, r) - \frac{k_b T_e(\lambda)}{e} \ln(n_e(\lambda, r)) \tag{2.24}$$

ϕ^* is known as the thermalized potential and was originally introduced by Morozov *et al.* [46] Based on Koo and Boyd's previous work, Eq. (2.24) is modified slightly in the present work to include a reference plasma density, n_e^*, so that the expression reads: [44]

$$\phi^*(\lambda) = \phi(\lambda, r) - \frac{k_b T_e(\lambda)}{e} \ln\left(\frac{n_e(\lambda, r)}{n_e^*}\right) \tag{2.25}$$

Since the reference density is a constant value, the modified expression does not change the calculation of $\phi(\lambda, r)$ unless $n_e(\lambda, r)$ falls below n_e^*. In the simulation, this situation is avoided by ensuring threshold limits are applied for the minimum plasma density in the domain.

2.2.3 Electron Current Density in the λ Grid

Using the expression for the electron current density in Eq. (2.21) in conjunction with the description of the thermalized potential in Eq. (2.25), an expression for $j_{e,\perp}(\lambda, r)$ can be determined. Note that $T_e = T_e(\lambda)$, $\phi^* = \phi^*(\lambda)$, $\phi = \phi(\lambda, r)$, and $n_e = n_e(\lambda, r)$. The gradient of the thermalized potential, $\frac{\partial \phi^*}{\partial \hat{n}}$, is described by:

$$\frac{\partial \phi^*}{\partial \hat{n}} = \frac{\partial \phi}{\partial \hat{n}} - \frac{k_b T_e}{e} \frac{\partial \ln(n_e)}{\partial \hat{n}} - \frac{k_b}{e} \ln\left(\frac{n_e}{n_e^*}\right) \frac{\partial T_e}{\partial \hat{n}} \tag{2.26}$$

Thus, Eq. (2.21) becomes:

$$j_{e,\perp} = \sigma \left(-\frac{\partial \phi^*}{\partial \hat{n}} \frac{k_b T_e}{e} \frac{\partial \ln(n_e)}{\partial \hat{n}} - \frac{k_b}{e} \ln\left(\frac{n_e}{n_e^*}\right) \frac{\partial T_e}{\partial \hat{n}} - \frac{1}{e n_e} \frac{\partial (n_e k_b T_e)}{\partial \hat{n}} \right) \tag{2.27}$$

Expanding the last term and simplifying, the expression becomes:

$$j_{e,\perp} = \sigma \left(-\frac{\partial \phi^*}{\partial \hat{n}} - \left[\ln\left(\frac{n_e}{n_e^*}\right) - 1 \right] \frac{k_b}{T_e} \frac{\partial T_e}{\partial \hat{n}} \right) \tag{2.28}$$

Finally, Eq. (2.28) can be re-written as a function of λ:

$$j_{e,\perp} = \sigma r B \left(-\frac{\partial \phi^*}{\partial \lambda} - \left[\ln\left(\frac{n_e}{n_e^*}\right) - 1 \right] \frac{k_b}{T_e} \frac{\partial T_e}{\partial \lambda} \right) \tag{2.29}$$

The electron current across a given magnetic field streamline can be calculated by integrating the contribution of particles that pass through the λ surface. Thus,

$$I_e = \int_S j_{e,\perp} \partial S \tag{2.30}$$

2.2.4 Electron Energy

Assuming that kinetic energy is negligible compared to internal energy and that the electrons take on a Maxwellian distribution (which is necessary for the fluid approximation),

the electron mean energy is described by $\epsilon = \frac{3}{2}\frac{k_b T_e}{e}$. The assumption of negligible kinetic energy is applicable when the electron bulk velocity is much smaller than the electron thermal velocity (low Mach number approximation). Strictly speaking, this assumption is not valid in the region where $\mathbf{E}\times\mathbf{B}$ drift is large. [29] Mean energy is transported via advection and diffusion, which are balanced by Joule heating and elastic and inelastic energy losses. Eq. (2.14) can therefore be recast as:

$$\frac{\partial}{\partial t}\left(\frac{3}{2}n_e k_b T_e\right) + \nabla\cdot\left(\frac{5}{2}n_e k_b T_e \mathbf{u} + \mathbf{q_e}\right) = \mathbf{j}_e\cdot\mathbf{E} - \Lambda_i \tag{2.31}$$

where Λ_i is the energy loss term due to inelastic collisions. Elastic energy losses due to heating via internal pressure gradients cancel with the pressure tensor term on the left hand side of Eq. (2.14), and Joule heating ($\mathbf{j}_e\cdot\mathbf{E}$) is the heating term due to collisional drag. [47]

Using the method followed by Koo, the electron energy equation can be further modified. [48] Heat conduction, $\mathbf{q}_e$, is written as:

$$\mathbf{q}_e = -K_e\nabla T_e \tag{2.32}$$

where the thermal conductivity, K_e, is described in terms of the thermal diffusivity, D_h, for a monatomic specie:

$$K_e = \rho c_p D_h = \frac{5}{2}n_e k_b D_h \tag{2.33}$$

The mass diffusion coefficient, D_m, conforms to the expression described by Eq. (2.20). A fundamental assumption of this analysis is that heat and mass diffuse by the same mechanism. Therefore, $D_h = D_m$, and the thermal conductivity can be described as a function of electron temperature and electron mobility:

$$K_e = \frac{5n_e k_b^2 T_e \mu_{e,\perp}}{2e} \tag{2.34}$$

Furthermore, the loss terms on the right hand side of Eq. (2.31) can be written as:

$$\mathbf{j}_e \cdot \mathbf{E} = -n_e e \mathbf{u} \cdot \mathbf{E} \tag{2.35}$$

and

$$\Lambda_i = n_e \epsilon \nu(\epsilon) \tag{2.36}$$

where $\nu(\epsilon)$ represents the frequency of electron energy losses. Eq. (2.31) is thus recast in its final form as:

$$\frac{\partial}{\partial t}(n_e \epsilon) + \nabla \cdot \left(\frac{5}{3} n_e \epsilon \mathbf{u}_e - \frac{10 \mu_{e,\perp} \epsilon}{9} \nabla \epsilon \right) = -n_e \mathbf{u}_e \cdot \mathbf{E} - n_e \epsilon \nu(\epsilon) \tag{2.37}$$

2.3 Ions and Neutral Particles

Since the HET plasma is in a non-equilibrium state, ions and neutral atoms are modeled using the DK or PIC kinetic techniques. A variety of physical phenomena occur in the thruster that contribute to the non-Maxwellian nature of the plasma. For example, the overlap of the ionization and acceleration regions in the channel may lead to a dispersion in the ion velocity. [49] In the plume, both high and low energy ions are present, with the latter dominating at large plume angles. [50] Some HET simulation techniques elect to model neutral particles using a continuum approach, but it has been demonstrated that neutral atoms play an important role in discharge plasma physics, for example via charge exchange (CEX), so this work applies a kinetic approach for both ions and neutral particles. [7, 51]

The DK approach considers the direct solution of the kinetic equation. For singly charged ions and neutral atoms, the distribution function, f, evolves over time, t, physical

space, z and r, and velocity space, v_z and v_r, according to the following kinetic equations:

$$\frac{\partial f_i}{\partial t} + v_z \frac{\partial f_i}{\partial z} + v_r \frac{\partial f_i}{\partial r} + \frac{eE_z}{m_i} \frac{\partial f}{\partial v_z} + \frac{eE_r}{m_i} \frac{\partial f}{\partial v_r} = S_i \tag{2.38a}$$

$$\frac{\partial f_n}{\partial t} + v_z \frac{\partial f_n}{\partial z} + v_r \frac{\partial f_n}{\partial r} = S_n \tag{2.38b}$$

In Eqs. (2.38a) and (2.38b), m_i is the particle mass, and subscripts i and n denote ions and neutral species, respectively. Ions in Eqn. (2.38a) accelerate due to the force from the electric field, $\mathbf{E} = (E_z, E_r)$. Since ions have a large gyroradius compared to the diameter of the channel, they are considered to be unmagnetized; therefore, the magnetic field force acting on ions is neglected. The general collision term is denoted by S, and it is calculated as the sum of collisions due to singly charged ionization which is discussed in Section 2.5.

The PIC approach considers the trajectories of each individual macroparticle through space and over time, effectively tracking the temporal change of the position of particles in phase space, namely:

$$\frac{d\mathbf{z}}{dt} = \mathbf{v} \tag{2.39a}$$

$$\frac{d\mathbf{v}}{dt} = \frac{\mathbf{F}}{m} \tag{2.39b}$$

where $\mathbf{F}$ is the field force acting on the particle of interest, i.e. $\mathbf{F}_i = e\mathbf{E}$ and $\mathbf{F}_n = 0$

2.4 Current Conservation

Assuming there is no charge buildup in the device, the total current, I_T, which includes the sum of the ion and electron contributions, is conserved. I_T is thus described by:

$$I_T = \int_S j_{e,\perp} \partial S + \int_S j_{i,\perp} \partial S \tag{2.40}$$

The ion current across a given magnetic field streamline can be calculated by integrating the contribution of particles that pass through the λ surface. Thus,

$$I_i = \int_S j_{i,\perp} \partial S = \int_S e n_i u_{i,\perp} \partial S \tag{2.41}$$

Incorporating the expressions for the electron and ion current contributions, namely Eq. (2.29) and Eq. (2.41), Eq. (2.40) becomes:

$$I_T = -\frac{\partial \phi^*}{\partial \lambda} \int_S e n_e \mu r B \partial S - \int_S e n_e \mu r B \left[\ln\left(\frac{n_e}{n_e^*}\right) - 1 \right] \frac{k_b}{e} \frac{\partial T_e}{\partial \lambda} \partial S + \int_S e n_i v_i \partial S \tag{2.42}$$

Eq. (2.42) can be rearranged to solve for the thermalized potential gradient, and summation across the domain is performed:

$$\begin{aligned} \sum_{\lambda=\lambda_a}^{\lambda_c} \frac{\partial \phi^*}{\partial \lambda} d\lambda = &- \sum_{\lambda=\lambda_a}^{\lambda_c} I_T \frac{1}{\int_S e n_e \mu r B \partial S} d\lambda \\ &- \sum_{\lambda=\lambda_a}^{\lambda_c} \frac{\int_S e n_e \mu r B \left[\ln\left(\frac{n_e}{n_e^*}\right) - 1 \right] \frac{k_b}{e} \frac{\partial T_e}{\partial \lambda} \partial S}{\int_S e n_e \mu r B \partial S} d\lambda \\ &+ \sum_{\lambda=\lambda_a}^{\lambda_c} \frac{\int_S e n_i v_i \partial S}{\int_S e n_e \mu r B \partial S} d\lambda \end{aligned} \tag{2.43}$$

The total current, I_T, is constant across all field lines and can be moved outside of the sum. If the thermalized potential is known at the anode and cathode, the expression for the

current simplifies to:

$$I_T = \left(\sum_{\lambda=\lambda_a}^{\lambda_c} \frac{d\lambda}{\int_S e n_e \mu r B \partial S} \right)^{-1} \left(\phi^*(\lambda_a) - \phi^*(\lambda_c) - \sum_{\lambda=\lambda_a}^{\lambda_c} \frac{\int_S e n_e \mu r B \left[\ln\left(\frac{n_e}{n_e^*}\right) - 1 \right] \frac{k_b}{e} \frac{\partial T_e}{\partial \lambda} \partial S}{\int_S e n_e \mu r B \partial S} d\lambda + \sum_{\lambda=\lambda_a}^{\lambda_c} \frac{\int_S e n_i v_i \partial S}{\int_S e n_e \mu r B \partial S} d\lambda \right) \tag{2.44}$$

2.5 Particle Collisions

Inelastic collisions play an important role in HET operation, as electron impact ionization of neutral propellant atoms both ignites and sustains the plasma discharge. Xenon is a noble gas with a large atomic mass and relatively low ionization energy, and for these reasons, it is commonly used as the propellant in a HET. Singly charged ions are the dominant ion species, and in this study, only singly charged, direct ionization collisions ($\mathrm{Xe} + \mathrm{e}^- \rightarrow \mathrm{Xe}^+ + 2\mathrm{e}^-$) are taken into account. However, it is worth noting that doubly and triply charged ions created via direct and stepwise ionization collisions are also observed in the HET discharge. For discharge voltages up to 300 V, the number flux fraction of doubly charged ions is 6-11%, and it is higher for larger discharge voltages. [52] Triply charged ions make up no more than a few percent of the total ion current in a HET discharge, but their presence becomes more important with larger discharge voltages and higher electron temperatures. [53] Furthermore, there is evidence to suggest that these high charged states are found in magnetically-shielded thrusters. [54]

Although typically not included in HET models (including the present model), some important excited states of xenon neutral atoms include the metastable state ($\mathrm{Xe}^*(^3\mathrm{P}_2)$) and radiative state ($\mathrm{Xe}^*(^3\mathrm{P}_1)$), among others. [29] Near the anode, the electron temperature is on the order of 2-5 eV, allowing for the presence of electronically excited states of xenon gas. Therefore, stepwise ionization to singly charged ions ($\mathrm{Xe}^* + \mathrm{e}^- \rightarrow \mathrm{Xe}^+ + 2\mathrm{e}^-$) in this

region may occur.

The ionization rate, $\dot{n}_{ion}$, is given by:

$$\dot{n}_{ion} = n_n n_e \xi(\epsilon) \tag{2.45}$$

where the electron density is equal to the ion density due to the quasineutral assumption. The reaction rate coefficient is a function of the particle energy distribution function of each reactant species, but because electrons are much less massive than neutral atoms, they have a much greater thermal velocity, and the rate coefficient can be reduced to a function of the electron energy distribution function, ϵ_e, namely: [53]

$$\xi = \int_{\epsilon_0}^{\infty} \left(\frac{2\epsilon_e}{m_e}\right)^{(1/2)} \sigma_i(\epsilon_e) f_e(\epsilon_e) d\epsilon_e \tag{2.46}$$

where ϵ_0 is the activation energy and σ_i is the collision cross-section. If electrons are described by a Maxwellian distribution function, then $\xi = \xi(T_e)$, and if collision cross-sections are known, Eq. (2.46) can be integrated to determine the rate coefficient. In this study, ionization cross-sections come from Puech and Mizzi. [55] For reference, ionization rates for singly-charged, doubly-charged, and stepwize ionization rates are calculated and plotted as a function of mean electron energy in Fig. 2.2. The DK method calculates ionization collisions in a deterministic fashion, while the PIC method utilizes the Monte Carlo Collision (MCC) approach. These numerical methods are described in Chapter III.

In some instances, low-energy neutral atoms and high-energy ions may collide with one another elastically, and an electron transfer event may occur ($\mathrm{Xe}_{slow} + \mathrm{Xe}^{+}_{fast} \rightarrow \mathrm{Xe}_{fast} + \mathrm{Xe}^{+}_{slow}$). This is known as a charge exchange (CEX) collision. This type of collision may significantly alter the VDFs, depopulating the high-energy region of the ion VDF and populating the low energy portion. The opposite happens for the neutral particle VDF, and thus the CEX collision creates a slow ion and a fast neutral atom. CEX collisions are known to be important in the plume region where the ionization rate is small. In space-

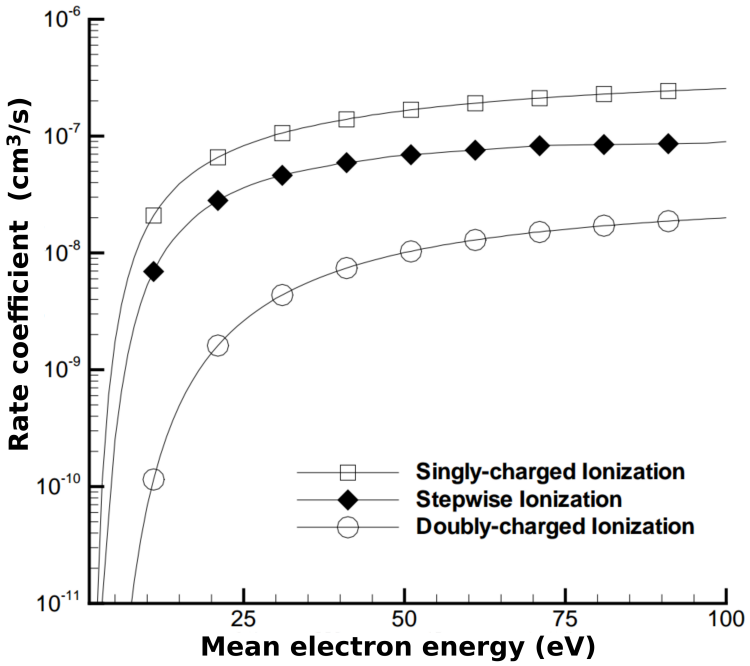

Figure 2.2: Xenon ionization rate coefficients. Singly charged ionization: $Xe + e^- \rightarrow Xe^+ + 2e^-$; stepwise ionization: $Xe^+ + e^- \rightarrow Xe^{++} + 2e^-$; and doubly charged ionization: $Xe + e^- \rightarrow Xe^{++} + 3e^-$. Image modified from Reference [48].

craft integration, CEX collisions are especially important, as they may result in vehicle sputtering and contamination. [56] Since the effects of CEX collisions are relatively small inside the thruster channel, this type of collision process is neglected in the present work.

2.6 Electron Transport and Energy Loss Mechanisms

The electron conductivity, σ, across magnetic field lines consists of classical and anomalous contributions. Restated from Eq. (2.18), the electron mobility ($\mu = \frac{\sigma}{en_e}$) perpendicular to the magnetic field is a function of the electron momentum transfer frequency, ν_m, and the electron cyclotron frequency, $\omega_{B,e}$:

$$\mu_{e,\perp} = \frac{e}{m_e \nu_m} \frac{1}{1+\Omega^2} \tag{2.47}$$

where the Hall parameter, $\Omega = \frac{\omega_{B,e}}{\nu_m}$. In this study, ν_m is simply augmented to account for effects of non-classical electron transport. This is necessary since electron transport perpendicular to the magnetic field is higher than predicted by classical transport. This approach of incorporating anomalous transport into the cross-field electron mobility term results in a modification of the drag term, $\mathbf{R}$, in Eq. (2.13), where $\mathbf{R}_{ano} = -mn\mathbf{u}\nu_{ano}$ and ν_{ano} is the frequency due to anomalous scattering.

The electron momentum transfer frequency is taken to be the frequency of electron-neutral collisions. Both electron-wall collisions and collisions due to Bohm diffusion are considered to be anomalous contributions to the overall electron collision frequency. The electron-neutral collision frequency, electron-wall collision frequency, and the effective Bohm collision frequency are calculated via the following expressions: [57]

$$\nu_{neut} = k_m n_n \tag{2.48}$$

$$\nu_{e,wall} = 10^7 \alpha_w \tag{2.49}$$

$$\nu_{Bohm} = \alpha_b \omega_{B,e} \tag{2.50}$$

where $k_m = 2.5 \times 10^{-13}$ m^{-3} s^{-1} and α_b is a coefficient less than 1. An example of calculated collision frequencies for electron-neutral collisions (ν_{neut}), electron-ion collisions, electron-wall collisions ($\nu_{e,wall}$), and Bohm collisions (ν_{Bohm}) in a typical HET channel and near-field plume is shown in Fig. 2.3.

Energy losses associated with ionization and excitation from the ground state as well as electron-wall losses are considered based on the computational models of Boeuf and Garrigues. [57] The expression for the frequency of electron energy loss due to ionization

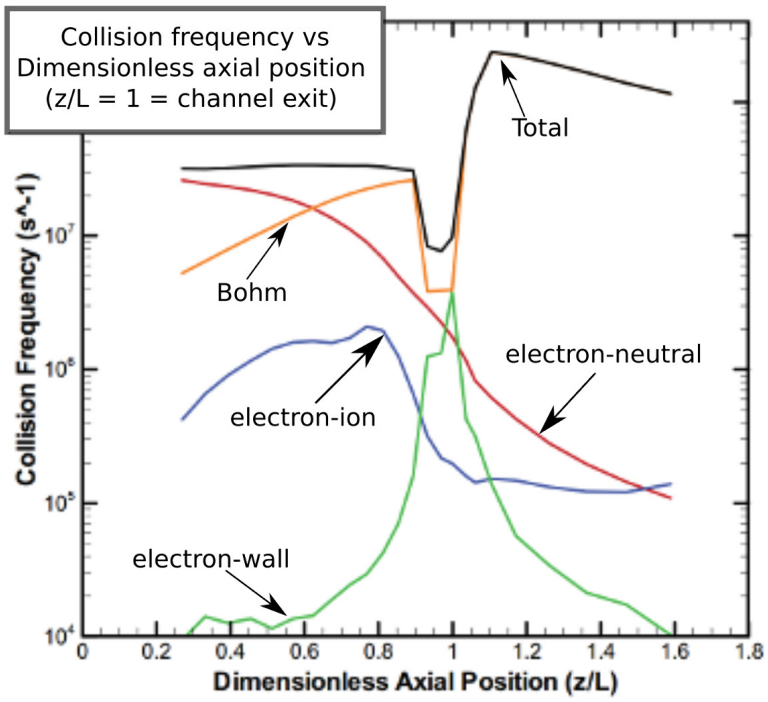

Figure 2.3: Collision frequency vs dimensionless axial position along the thruster channel centerline of a 6 kW Hall thruster for a total vacuum pressure condition ($p = 0$) . Image modified from Reference [58].

and excitation from the ground state is described by:

$$\nu(\epsilon)_{e-Xe} = n_n k_{e-Xe}(\epsilon) \tag{2.51}$$

where $k_{e-Xe}(\epsilon)$ represents the loss rate due to singly charged ionization from the ground state. The frequency of electron energy loss to the walls is described by:

$$\nu(\epsilon)_{walls} = 10^7 \alpha_w \exp\left(\frac{-U_{loss}}{\epsilon}\right) \tag{2.52}$$

where U_{loss} represents the potential barrier due to the formation of a dielectric sheath at the walls and $\alpha_w < 1$ represents the relative frequency of electron-wall collisions.

CHAPTER III

Numerical Methods

"All models are wrong, but some are useful."

– George E. P. Box

In this chapter, the hybrid-DK and hybrid-PIC numerical methods are introduced. The DK approach solves kinetic equations, such as the Vlasov and Boltzmann equations, in discretized phase space by evaluating the grid-based VDFs as they evolve over time. This Eulerian approach is distinct from the Lagrangian PIC approach, which models the trajectories of macroparticles in space and tracks their motion over time. In this work, a quasi-one-dimensional fluid algorithm is applied for electrons, and the DK and PIC approaches are used to model comparatively massive ions and neutral particles.

The chapter is set up as follows: DK and PIC methods are compared in Section 3.1, and existing hybrid-PIC HET simulations are reviewed in Section 3.2. The general simulation framework is described in Section 3.3, and the fluid electron algorithm is detailed in Section 3.4. Finally, kinetic ion and neutral algorithms for both the discretized DK and PIC models are described in Section 3.5.

3.1 Comparison of Direct Kinetic and Particle Methods

A brief synopsis of the general differences between the DK and PIC approaches is found in Table 3.1. Additionally, Figure 3.1 displays graphically the distinction between fluid, PIC,

and DK methods. The Vlasov and Boltzmann equations (Eq. (1.7)) are multidimensional, first-order, hyperbolic PDEs. The Eulerian DK approach solves these kinetic equations in discretized phase space by evaluating the grid-based VDFs as they evolve over time (Eqs. (2.38a), (2.38b)), whereas the Lagrangian PIC approach models the trajectories of macroparticles in space and tracks their motion over time, considering the set of two first-order ordinary differential equations (ODEs) of motion (Eqs. (2.39a), (2.39b)) for each individual macroparticle.

Although PIC techniques are more common, grid-based approaches similar to the DK method have been used in research areas including space physics, astrophysics, and tokamak modeling applications. The first grid-based Vlasov simulation was developed by Cheng and Knorr, and it utilized a finite difference scheme with cubic spline interpolation. [59] Other grid-based approaches have since been employed, including the finite volume method and the semi-Lagrangian technique. [60] The computational memory per physical cell is N_v^d, where N_v is the number of grid points in velocity space, and d is the number of dimensions. [7] For large systems, the computational cost may be prohibitive, and the grid size can be simplified through methods including phase space reduction [61, 62] and adaptive grid techniques. [63] The method utilized in this work, known as the direct kinetic (DK) method, was developed by Hara *et al* [7, 15]. It is a second-order accurate, finite volume solution technique with a modified Arora-Roe limiter to calculate the numerical flux of kinetic quantities through each cell interface, and it utilizes a Runge-Kutta method for time integration. No adaptive grid techniques are employed.

3.1.1 Numerical Error

Numerical errors are present in both the DK and PIC methods. Sources of numerical error may include rounding error, truncation error, finite statistical sampling, i.e. the use of a finite number of randomly distributed particles, and finite grid resolution. The advantage of the DK method compared to the PIC method is that there is no statistical noise in the DK

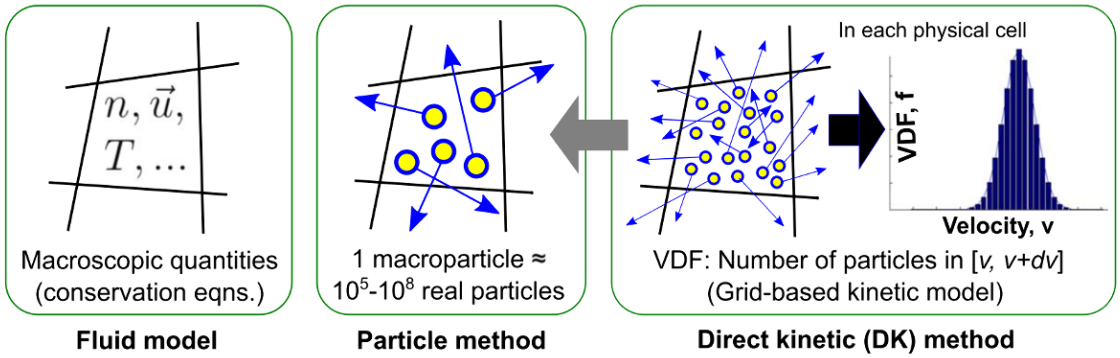

Figure 3.1: A graphical distinction between fluid, PIC, and DK numerical methods, considering the quantities in a single, discretized cell. Fluid models (left) consider the evolution of macroscopic quantities via conservation equations. A PIC method (middle) models the trajectories of macroparticles, and a DK method (right) considers the distribution of particles in phase space. Image reproduced from Reference [29].

Table 3.1: Comparison of direct kinetic and particle-in-cell modeling approaches. [12]

	Grid-based (DK)	Particle-based (PIC)
Description	Calculate VDFs in phase space	Solve for motion of macroparticles
Specification	Eulerian	Lagrangian
Equation	Hyperbolic partial differential equation	Ordinary differential equation
Macroscopic properties	Moments of VDFs	Particle information sampling
Collision rate	Integral of collision operator	Collision probability
Computational memory per physical cell	N_v^d (N_v: number of grid points in velocity space; d: number of dimensions)	$2dN_p$ (N_p: number of particles per cell; d: number of dimensions)
Primary source of numerical error	Global truncation error: $\epsilon_T \sim O[N_v^{-p}]$ (p is the order of accuracy of the numerical scheme)	Statistical noise: $\epsilon_s \sim O[N_p^{-1/2}]$

algorithm. The statistical noise associated with the PIC algorithm is nearly irreducible, and thus the resolution of phase space is poor. [64] Statistical noise becomes problematic if the physics of interest are in the low density region of phase space or the high-energy tail of the distribution function. [61] Discrete particle noise has been found to dominate the late-time decay of electron temperature gradient turbulence as well as the steady-state heat transport in simulations of plasma microturbulence, implying that conclusions regarding the behavior of such turbulence result from mistaking the effects of discrete particle noise for turbulence. [65] In HET simulations of the electron cyclotron drift instability, an instability associated with high frequency oscillatory behavior, it is found that numerical noise is responsible for the destruction of the cyclotron resonance if the number of macroparticles per cell is lower than approximately 1000. [39]

There is a body of literature available on discrete particle noise, [66, 67, 68] and for some plasma models, numerical noise levels are quantified as code and solution verification issues. [65, 69, 70] Verification is a process that assesses the correctness with which mathematical models are reproduced in a computational simulation. Verification can be conducted for the code itself by simulating problems for which analytic solutions are known, and solution verification can be applied via numerical error analysis of code responses for a problem without a known solution. [70] However, the credibility of solution verification is built upon a solid foundation of code verification problems. To quantify the level of numerical noise in a PIC simulation during the solution verification phase, statistical and discretization uncertainties are typically taken into account. The statistical uncertainty in the solution can be estimated by repeating the simulation with different pseudorandom number generator seeds. For the discretization uncertainty, the Richardson extrapolation can be used to approximate the analytical solution (or otherwise high precision solution of known accuracy), and the grid convergence may then be used to estimate the relative discretization uncertainty. [69]

In the present study, an axial-radial hybrid-PIC simulation of a discharge plasma is of

interest. Although such a HET simulation typically exhibits is a dominant low frequency mode around 10 kHz, numerical noise is nonetheless present in the model. To the author's knowledge, error quantification studies have not been performed at the verification stage for HET hybrid-PIC simulations. Unfortunately, without knowledge of individual numerical error calculations, this makes it difficult to accurately quantify the overall level of numerical noise in a multi-parameter simulation at a later stage. This is supported by the absence of simulation convergence studies for existing hybrid-PIC HET discharge plasma models in the literature. In general, provided that the grid discretization is satisfactory ($v\Delta t < \Delta x$), it is possible to say that the primary source of numerical error associated with the PIC technique is statistical noise, ϵ_s, as indicated in Table 3.1. The source of statistical noise is attributed to the use of a finite number of discrete macroparticles, and numerical errors occur when particle information is sampled using averaging techniques. In the hybrid-PIC simulation, statistical noise is present due to the use of neutral macroparticles, ion macroparticles, and a stochastic collision technique. The spatial error due to particle sampling is $O(N_p^{-1/2})$ and can be decreased by increasing the number of macroparticles in the simulation domain. However, for a dynamic simulation, sampling is required often, and statistical noise increases with the sampling rate. To mitigate the amount of noise associated with particle sampling, methods such as moment preserving constrained resampling (MPCR) have recently been introduced into some PIC numerical schemes. [71]

While the DK method contains no statistical noise, it is important that its overall numerical error be relatively low to justify its usage since the computational cost can be quite high, particularly for multidimensional simulations. The one-dimensional DK numerical method was verified and validated in previous work by Hara. [7] For the DK method, truncation error, the source of error associated with numerically solving a differential equation system, was found to be the dominant source of numerical error. Following the error calculations of Hara for the DK method, the local truncation error is $O(h^{p+1})$ for a p-th order method, and the global truncation error, or accumulative error, is $O(h^p)$ where h represents

the grid size. For a given system of size L_v, $h = L_v/N_v$; therefore, the numerical error for the grid-based method is proportional to $O(N_v^{-p})$. Note that the temporal error is neglected in this calculation. The implication is that the error can be reduced by using a larger number of grid points or a higher order of accuracy in the numerical scheme. The DK simulation does not require sampling and is therefore well-suited to model dynamically-changing, non-equilibrium flows such as the HET discharge plasma.

3.2 Review of Hybrid-PIC Hall Thruster Simulations

The discharge plasma in a HET has been simulated using a variety of fluid [72, 73, 74], kinetic [75, 76, 77], and hybrid [42, 78, 45, 44] modeling techniques in one, two, and three dimensions. Since this work discusses a two-dimensional model of the thruster channel and near-field plume, this section will be limited to a review of simulations with a similar configuration. These simulations leverage the difference in mass between electrons and ions to treat the electrons as a continuous fluid while ions and neutral particles are treated as discrete macroparticles; thus, they are known as "hybrid-PIC" simulations. Historically, hybrid-PIC simulations have performed well in the sense that, when coupled with a reasonable electron transport model, they have produced experimentally-verified steady-state trends and macroscopic properties including thrust and Isp.

Perhaps the most well-known hybrid-PIC simulation is HPHall which was originally developed by Fife in the late 1990s and was the first simulation to reproduce an oscillation of the same frequency as the HET breathing mode. [42] As a result of ongoing modeling improvements and additions, the present-day HPHall contains a number of capabilities. First, Gamero-Castaño and Katz implemented channel erosion and improved existing sheath models based on Ahedo's model for a three-species plasma sheath. [79, 80] Later, Parra *et al* updated heavy particle integration and weighting as well as the cross-field electron transport model. [81] Hofer *et al* further improved the cross-field transport and heavy

species models, and Huismann added a DSMC module for handling momentum-exchange and charge-exchange collisions between ions and neutral species. [58, 82, 56] Smith and Boyd updated collision cross sections and added triply charged ions to the simulation, and Dragnea and Boyd added the capability to use a two-dimensional electron fluid model in lieu of the quasi-one-dimensional model, although this feature requires further verification. [53, 83]

In the early 2000s, several HET models were constructed, primarily with the intention of investigating anomalous electron transport in the $z-r$ domain. The model of Fernandez *et al* is similar to HPHall, although details such as the computational grid, integration scheme, and treatment of nonlinear terms are different. [78] This model was primarily used by Scharfe *et al* to create a cross-field electron transport model based on simulated plasma properties. [84, 85] Another simulation was created by Hagelaar *et al* in 2002 which utilized ad hoc empirical parameters to characterize the cross-field electron mobility and electron energy losses. [45] Koo and Boyd's hybrid-PIC simulation is somewhat similar to that implemented by Hagelaar *et al.*, particularly with respect to the implementation of the current solver; it also focused on the implementation of an appropriate electron transport model. [44, 48] In this study, a modified version of Koo and Boyd's simulation is used for the hybrid-PIC approach. Its use is justified based on the fact that the hybrid-PIC simulation is written in a Cartesian coordinate system, enabling one-to-one mapping with the hybrid-DK simulation, and also because there are no additional physics modules, such as those included in HPHall's heavy particle algorithm, to further complicate an initial benchmarking effort for the hybrid-DK simulation.

3.3 Simulation Framework

The simulation domain includes the thruster channel and near-field plume, as illustrated in Fig. 3.2. A uniform Cartesian grid is used for the kinetic algorithm, and rotational

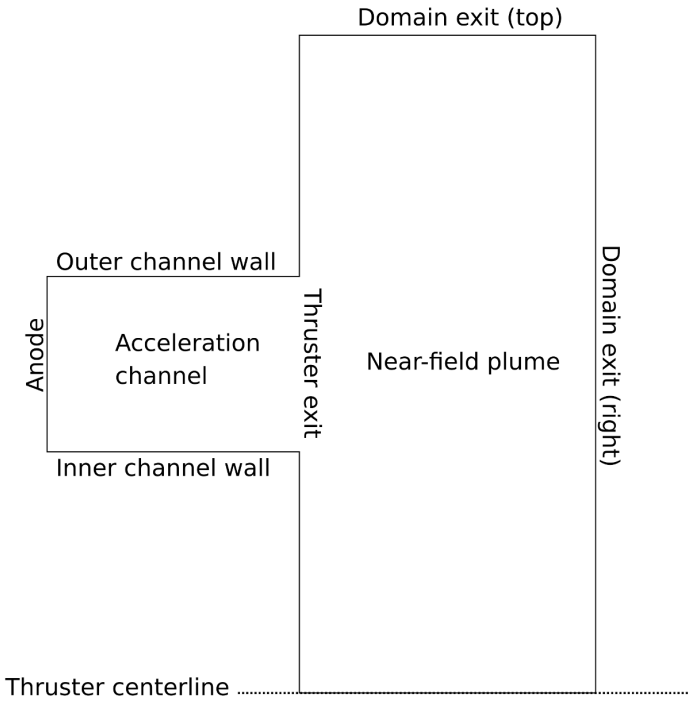

Figure 3.2: Hybrid-kinetic simulation domain.

symmetry about the thruster centerline is assumed. Neutral species are injected into the simulation at the anode side of the thruster (left hand side of the domain). The order of operations is very similar for the hybrid-DK and hybrid-PIC simulations. Hence, a general hybrid-kinetic framework is shown in Fig. 3.3. The electron fluid solver is employed to calculate the discharge current, electric field, and electron energy. The electron energy is required for the ionization algorithm, and the electric field is an input for the ion solver within the kinetic framework. The kinetic solver outputs mean properties including the ion and neutral densities and velocities, and these are passed to the electron solver as required.

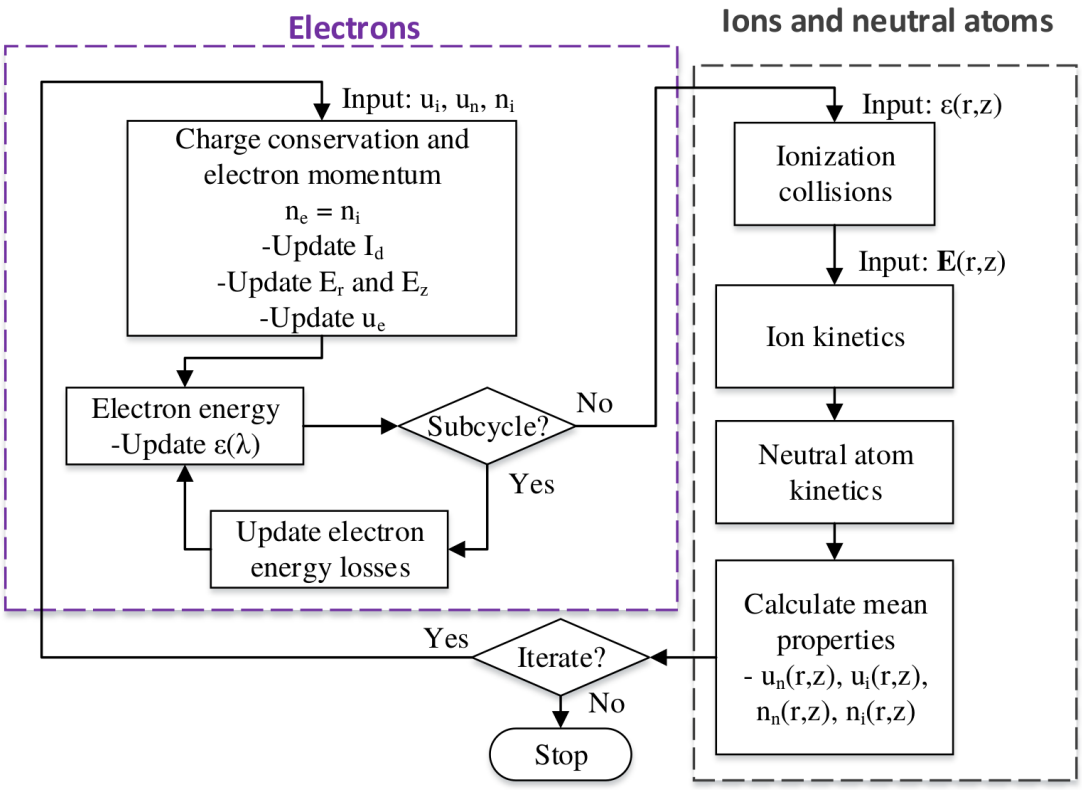

Figure 3.3: Hybrid-kinetic flowchart for the HET plasma simulation. The fluid electron algorithm is shown on the left, and the kinetic algorithm for ions and neutral particles is shown on the right.

3.4 Modeling Electrons

The quasi-one dimensional electron fluid algorithm is used to solve the equations outlined in Section 2.2. The present section describes how these equations are numerically solved in both the hybrid-DK and hybrid-PIC simulations. There are two main modules: the current solver and the electron energy equation solver.

3.4.1 Electron λ Grid

The electron grid is composed of discrete λ-lines, an example of which is shown in Fig. 3.4. To generate this grid, the magnetic field stream function is created via Eqs. (2.2a) and (2.2b). Starting at one corner of the domain, B_z and B_r are calculated at each nodal location via the following relationships:

$$\int d\lambda = \int r B_z dr \tag{3.1a}$$

$$\int d\lambda = \int -r B_r dz \tag{3.1b}$$

where r is measured from the centerline of the thruster, i.e. the bottom of the domain ($r = 0$) in Fig. 3.2. The absolute value of λ is not important; rather the reference values are essential. Therefore, the location where the minimum value of λ is found is set to zero, i.e. $\lambda_{ref} = \lambda_{min}$, and all other values of λ are calculated with respect to the minimum value ($\lambda = \lambda - \lambda_{ref}$). The spacing between λ-lines, $d\lambda$, is uniform by default, and the number of desired λ-lines is determined by the user. It is important that there are a sufficient number of λ-lines inside the thruster channel so that gradients in electron properties are sufficiently resolved; in cases where uniform spacing of λ results in very few λ-lines inside the channel, non-uniform spacing must be used.

The electron algorithm primarily considers the *active* solution domain, which lies be-

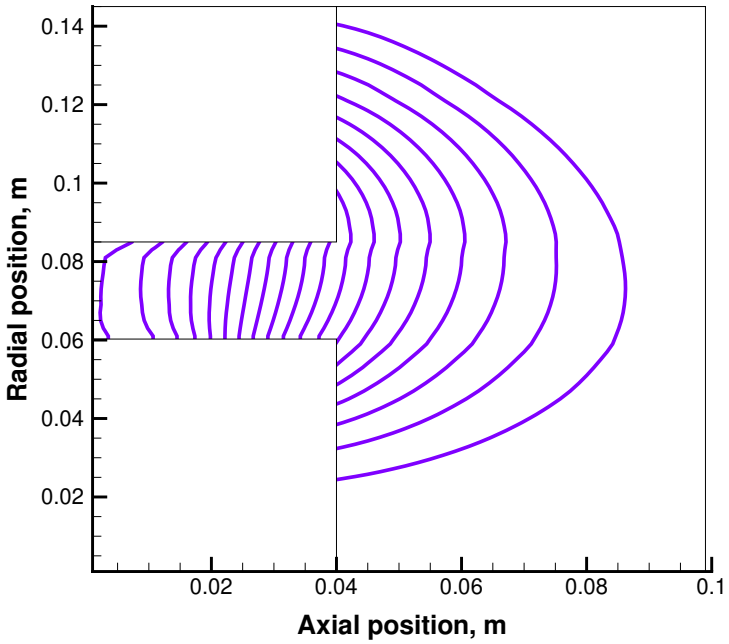

Figure 3.4: Discretized electron λ grid.

tween the anode λ-line, λ_a, and the cathode λ-line, λ_c. The anode and cathode magnetic field streamlines are offset from the left and right hand sides of the domain as shown in Fig. 3.5. Outside of the active solution domain, flow properties are extrapolated.

3.4.2 Electron Momentum and Current Conservation

Strictly speaking, some charge accumulation may occur at the dielectric insulating walls of the thruster; [86] however, the electron and ion currents are assumed to balance at the walls. Therefore, the total current, I_T, is conserved. The final form of the total current is

calculated in Eq. (2.44) and re-written here:

$$I_T = \left(\sum_{\lambda=\lambda_a}^{\lambda_c} \frac{d\lambda}{\int_S en_e \mu r B \partial S} \right)^{-1} \left(\phi^*(\lambda_a) - \phi^*(\lambda_c) - \sum_{\lambda=\lambda_a}^{\lambda_c} \frac{\int_S en_e \mu r B \left[\ln\left(\frac{n_e}{n_e^*}\right) - 1 \right] \frac{k_b}{e} \frac{\partial T_e}{\partial \lambda} \partial S}{\int_S en_e \mu r B \partial S} d\lambda + \sum_{\lambda=\lambda_a}^{\lambda_c} \frac{\int_S en_i v_i \partial S}{\int_S en_e \mu r B \partial S} d\lambda \right) \tag{3.2}$$

where n_e^* is a reference plasma density set to $n_e^* = 10^{12}$ m^{-3}. Numerical integration occurs across each λ surface between λ_a and λ_c using a central differencing scheme. In order to calculate the total current, the thermalized potential, ϕ^*, at the anode and cathode λ-lines must be known. In this model, since the plasma density and electron temperature are not necessarily fixed at the anode or cathode, ϕ^* is assumed to float at these locations, but ϕ is fixed.

From the total current, the gradient of the thermalized potential can be calculated via the following expression:

$$\frac{\partial \phi^*}{\partial \lambda} = -I_T \frac{1}{\int_S en_e \mu r B \partial S} - \frac{\int_S en_e \mu_{e,\perp} r B \left[\ln\left(\frac{n_e}{n_e^*}\right) - 1 \right] \frac{k_b}{e} \frac{\partial T_e}{\partial \lambda} \partial S}{\int_S en_e \mu_{e,\perp} r B \partial S} + \frac{\int_S en_i v_i \partial S}{\int_S en_e \mu_{e,\perp} r B \partial S} \tag{3.3}$$

The thermalized potential is then calculated using a forward differencing scheme, and the two-dimensional potential can be directly computed within the active domain as:

$$\phi(\lambda, r) = \phi^*(\lambda) + \frac{k_b T_e}{e} \ln\left(\frac{n_e(\lambda, r)}{n_e^*}\right) \tag{3.4}$$

Note that $\phi(\lambda, r)$ must be interpolated to the Cartesian grid. The potential is simply extrapolated upstream of λ_a and downstream of λ_c, as it is assumed that ϕ should be approximately constant in the high electron diffusion region in the vicinity of the anode, and likewise the potential drop reasonably far into the plume is minimal. One of the downsides of solv-

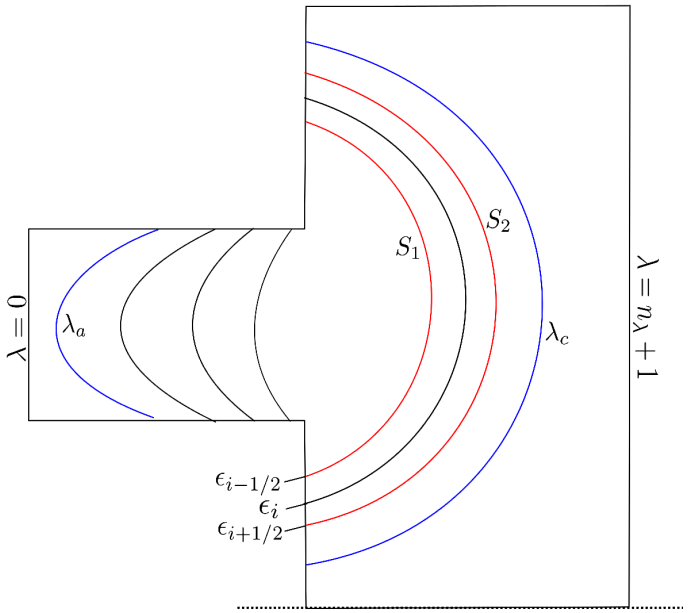

Figure 3.5: Electron solution geometry, not drawn to scale.

ing Eq. (3.2) directly is that it is not possible to take into account the potential fall due to an anode sheath since ϕ must be fixed at λ_a. An alternative approach to the solution methodology outlined here is discussed in Ch. VII.

3.4.3 Electron Energy Conservation

The method described in this section corresponds with the numerical scheme outlined by Koo in Reference [48], similar to the derivation by Fife. [42] Eq. (2.37) is the differential equation describing the electron energy along the centerline of the thruster. To account for the contribution of plasma off the centerline, it is volumetrically integrated over the domain as follows:

$$\int_V \frac{\partial}{\partial t}(n_e\epsilon)dV + \int_V \nabla\cdot\left(\frac{5}{3}n_e\epsilon\mathbf{u}_e\right)dV - \int_V \nabla\cdot\left(\frac{10\mu_{e,\perp}\epsilon}{9}\nabla\epsilon\right)dV = -\int_V n_e\mathbf{u}_e\cdot\mathbf{E}dV - \int_V n_e\epsilon\nu(\epsilon)dV \qquad (3.5)$$

Volume integrals are evaluated over the volume centered at ϵ_i, as shown in Fig. 3.5, and S_1 and S_2 integrals are evaluated at the surfaces marked $\epsilon_{i-1/2}$ and $\epsilon_{i+1/2}$, respectively. The solution methodology is described in the following subsections.

3.4.3.1 The Electron Velocity and Electric Field

To write an ODE for Eq. (3.5), it is necessary to consider $(u_{e,\hat{n}}, E_{\hat{n}}) = f(\epsilon)$. The thermalized potential gradient, $\frac{\partial \phi^*}{\partial \lambda}$, is a function of ϵ as follows:

$$\begin{aligned}\frac{\partial \phi^*}{\partial \lambda} &= \frac{-I_T + \int_S e n_i v_i \partial S}{\int_S e n_e \mu_{e,\perp} r B \partial S} - \frac{\int_S e n_e \mu_{e,\perp} r B \left[\ln\left(\frac{n_e}{n_e^*}\right) - 1\right] \frac{k_b}{e} \frac{2}{3} \frac{\partial \epsilon}{\partial \lambda} \partial S}{\int_S e n_e \mu_{e,\perp} r B \partial S} \\ &= j_1 + j_2 \frac{\partial \epsilon}{\partial \lambda}\end{aligned} \tag{3.6}$$

where the coefficients j_1 and j_2 are described by:

$$j_1 = \frac{-I_T + \int_S e n_i v_i \partial S}{\int_S e n_e \mu_{e,\perp} r B \partial S} \tag{3.7a}$$

$$j_2 = -\frac{\int_S e n_e \mu_{e,\perp} r B \left[\ln\left(\frac{n_e}{n_e^*}\right) - 1\right] \frac{2}{3} \partial S}{\int_S e n_e \mu_{e,\perp} r B \partial S} \tag{3.7b}$$

Modifying Eq. (2.29) slightly, the electron velocity is described by:

$$\begin{aligned}u_{e,\hat{n}} &= \mu_{e,\perp} r B \left(\frac{\partial \phi^*}{\partial \lambda} + \left[\ln\left(\frac{n_e}{n_e^*}\right) - 1\right] \frac{2}{3} \frac{\partial \epsilon}{\partial \lambda}\right) \\ &= k_1 \frac{\partial \phi^*}{\partial \lambda} + k_2 \frac{\partial \epsilon}{\partial \lambda}\end{aligned} \tag{3.8}$$

where the coefficients k_1 and k_2 conform to:

$$k_1 = \mu_{e,\perp} r B \tag{3.9a}$$

$$k_2 = \frac{2}{3}\mu_{e,\perp} rB \left[\ln\left(\frac{n_e}{n_e^*}\right) - 1\right] \tag{3.9b}$$

Substituting Eq. (3.6) into Eq. (3.8), the following expression is obtained for $u_{e,\hat{n}}$:

$$\begin{aligned} u_{e,\hat{n}} &= k_1\left(j_1 + j_2\frac{\partial\epsilon}{\partial\lambda}\right) + k_2\frac{\partial\epsilon}{\partial\lambda} \\ &= k_1 j_1 + (k_1 j_2 + k_2)\frac{\partial\epsilon}{\partial\lambda} \end{aligned} \tag{3.10}$$

Finally, the electric field, $E_{\hat{n}}$, can be calculated as follows:

$$\begin{aligned} E_{\hat{n}} &= -\frac{\partial\phi}{\partial\hat{n}} \\ &= -\frac{\partial\phi^*}{\partial\hat{n}} - \frac{2}{3}\epsilon\frac{\partial\ln(n_e)}{\partial\hat{n}} - \frac{2}{3}\frac{\partial\epsilon}{\partial\hat{n}}\ln\left(\frac{n_e}{n_e^*}\right) \\ &= -rB\frac{\partial\phi^*}{\partial\lambda} - \frac{2}{3}rB\frac{\partial\ln(n_e)}{\partial\lambda}\epsilon - \frac{2}{3}rB\ln\left(\frac{n_e}{n_e^*}\right)\frac{\partial\epsilon}{\partial\lambda} \\ &= h_1\frac{\partial\phi^*}{\partial\lambda} + h_2\epsilon + h_3\frac{\partial\epsilon}{\partial\lambda} \end{aligned} \tag{3.11}$$

where coefficients h_1, h_2, and h_3 are described by:

$$h_1 = -rB \tag{3.12a}$$

$$h_2 = -\frac{2}{3}rB\frac{\partial\ln(n_e)}{\partial\lambda} \tag{3.12b}$$

$$h_3 = -\frac{2}{3}rB\ln\left(\frac{n_e}{n_e^*}\right) \tag{3.12c}$$

Computing the expression for $\frac{\partial\phi^*}{\partial\lambda}$ using Eq. (3.6), Eq. (3.11) simplifies to:

$$E_{\hat{n}} = h_1 j_1 + (h_1 j_2 + h_3)\frac{\partial\epsilon}{\partial\lambda} + h_2\epsilon \tag{3.13}$$

3.4.3.2 Discretized Electron Energy Equation

In this section, the terms in Eq. (3.5) are discretized for the numerical simulation. The time rate of change of electron energy becomes:

$$\begin{aligned}\int_V \frac{\partial}{\partial t}(n_e\epsilon)dV &= \int_V n_e\frac{\partial \epsilon}{\partial t}dV + \int_V \epsilon\frac{\partial n_e}{\partial t}dV \\ &= \frac{\partial \epsilon}{\partial t}\int_V n_e dV + \epsilon\int_V \frac{\partial n_e}{\partial t}dV \\ &= A_1\frac{\partial \epsilon_V}{\partial t} + A_2\epsilon_V \end{aligned} \tag{3.14}$$

The second term in Eq. (3.5) is a convective term. To numerically integrate this term, the divergence theorem is employed, and the expression for $u_{e,\hat{n}}$ from Eq. (3.8) is used:

$$\begin{aligned}\int_V \nabla\cdot\left(\frac{5}{3}n_e\epsilon\mathbf{u}_e\right)dV &= \int_S \left(\frac{5}{3}n_e\epsilon\mathbf{u_e}\right)\cdot\hat{n}dS \\ &= \int_S \frac{5}{3}n_e k_1 j_1 \epsilon dS + \int_S \frac{5}{3}n_e(k_1 j_2 + k_2)\epsilon\frac{\partial\epsilon}{\partial\lambda}dS \\ &= \left(\int_{S_1} -\frac{5}{3}n_e k_1 j_1 dS\right)\epsilon_{S_1} \\ &+ \left(\int_{S_1} -\frac{5}{3}n_e(k_1 j_2 + k_2)dS\right)\left(\epsilon\frac{\partial\epsilon}{\partial\lambda}\right)_{S_1} \\ &+ \left(\int_{S_2} \frac{5}{3}n_e k_1 j_1 dS\right)\epsilon_{S_2} \\ &+ \left(\int_{S_2} \frac{5}{3}n_e(k_1 j_2 + k_2)dS\right)\left(\epsilon\frac{\partial\epsilon}{\partial\lambda}\right)_{S_2} \\ &= A_3\epsilon_{S_1} + A_4\left(\epsilon\frac{\partial\epsilon}{\partial\lambda}\right)_{S_1} + A_5\epsilon_{S_2} + A_6\left(\epsilon\frac{\partial\epsilon}{\partial\lambda}\right)_{S_2}\end{aligned} \tag{3.15}$$

The third term in Eq. (3.5) is a diffusion term, and the divergence theorem is again employed to obtain:

$$\begin{aligned}\int_V \nabla\cdot\left(\frac{10\mu_{e,\perp}\epsilon}{9}\nabla\epsilon\right)dV &= \int_S\left(\frac{10}{9}n_e\mu_{e,\perp}\epsilon\nabla\epsilon\right)\cdot\hat{n}dS\\ &= \int_S\left(\frac{10}{9}n_e\mu_{e,\perp}\epsilon rB\frac{\partial\epsilon}{\partial\lambda}\hat{n}\right)\cdot\hat{n}dS\\ &= \left(\int_{S_1}-\frac{10}{9}n_e\mu_{e,\perp}rBdS\right)\left(\epsilon\frac{\partial\epsilon}{\partial\lambda}\right)_{S_1}\\ &+\left(\int_{S_2}\frac{10}{9}n_e\mu_{e,\perp}rBdS\right)\left(\epsilon\frac{\partial\epsilon}{\partial\lambda}\right)_{S_2}\\ &= A_7\left(\epsilon\frac{\partial\epsilon}{\partial\lambda}\right)_{S_1}+A_8\left(\epsilon\frac{\partial\epsilon}{\partial\lambda}\right)_{S_2}\end{aligned}\tag{3.16}$$

The fourth term in Eq. (3.5) is the ohmic heating term, and the volume integral is evaluated by substituting in $u_{e,\hat{n}}$ from Eq. (3.8) and $E_{\hat{n}}$ from Eq. (3.13):

$$\begin{aligned}\int_V n_e\mathbf{u}_e\cdot\mathbf{E}dV &= \int_V n_e\left(k_1j_1+(k_1j_2+k_2)\frac{\partial\epsilon}{\partial\lambda}\right)\\ &\cdot\left(h_1j_1+(h_1j_2+h_3)\frac{\partial\epsilon}{\partial\lambda}+h_2\epsilon\right)dV\\ &= \int_V n_ek_1j_1^2h_1+n_ek_1j_1(h_1j_2+h_3)+n_eh_1j_2(k_1j_2+k_2)\frac{\partial\epsilon}{\partial\lambda}\\ &+n_e(k_1j_2+k_2)(h_1j_2+h_3)\frac{\partial\epsilon}{\partial\lambda}\frac{\partial\epsilon}{\partial\lambda}+n_eh_2(k_1j_2+k_2)\frac{\partial\epsilon}{\partial\lambda}\epsilon\\ &+n_ek_1j_1h_2\epsilon dV\\ &= A_9+A_{10}\frac{\partial\epsilon_V}{\partial\lambda}+A_{11}\frac{\partial\epsilon_V}{\partial\lambda}\frac{\partial\epsilon_V}{\partial\lambda}+A_{12}\left(\frac{\partial\epsilon_V}{\partial\lambda}\epsilon_V\right)+A_{13}\epsilon_V\end{aligned}\tag{3.17}$$

The final term in Eq. (3.5) represents inelastic energy losses, and it is evaluated as:

$$\begin{aligned}\int_V n_e\epsilon\nu(\epsilon)dV &= \left(\int_V n_e\nu(\epsilon)dV\right)\epsilon_V\\ &= \left(\int_V n_e(\nu(\epsilon)_{e-Xe}+\nu(\epsilon)_{walls})+\nu(\epsilon)_{e-Xe^+}dV\right)\epsilon_V\\ &= A_{14}k_{e-Xe}(\epsilon_V)\epsilon_V+A_{15}\nu(\epsilon_V)_{walls}\epsilon_V+A_{16}k_{e-Xe^+}(\epsilon_V)\epsilon_V\end{aligned}\tag{3.18}$$

Note that if the mean electron energy lies between two different threshold energy levels, the energy loss coefficient is linearly interpolated between the two threshold values that correspond with the distinct energy levels.

Finally, the ODE for the electron energy combines all of the terms and divides by A_1 so that the following final form is obtained:

$$\begin{aligned}\frac{\partial \epsilon_V}{\partial t} = & \frac{-A_2}{A_1}\epsilon_V \\ & - \frac{A_3}{A_1}\epsilon_{S_1} - \frac{A_4}{A_1}\left(\epsilon\frac{\partial \epsilon}{\partial \lambda}\right)_{S_1} - \frac{A_5}{A_1}\epsilon_{S_2} - \frac{A_6}{A_1}\left(\epsilon\frac{\partial \epsilon}{\partial \lambda}\right)_{S_2} \\ & + \frac{A_7}{A_1}\left(\epsilon\frac{\partial \epsilon}{\partial \lambda}\right)_{S_1} + \frac{A_8}{A_1}\left(\epsilon\frac{\partial \epsilon}{\partial \lambda}\right)_{S_2} \\ & - \frac{A_9}{A_1} - \frac{A_{10}}{A_1}\frac{\partial \epsilon_V}{\partial \lambda} - \frac{A_{11}}{A_1}\frac{\partial \epsilon_V}{\partial \lambda}\frac{\partial \epsilon_V}{\partial \lambda} - \frac{A_{12}}{A_1}\left(\epsilon\frac{\partial \epsilon}{\partial \lambda}\right)_V - \frac{A_{13}}{A_1}\epsilon_V \\ & - \frac{A_{14}}{A_1}k_{e-Xe}(\epsilon_V)\epsilon_V - \frac{A_{15}}{A_1}\nu(\epsilon_V)_{walls}\epsilon_V - \frac{A_{16}}{A_1}k_{e-Xe^+}(\epsilon_V)\epsilon_V \end{aligned} \tag{3.19}$$

The loss coefficients (A14-A16) are subcycled and updated at the electron time step (200 electron time steps/global time step) while other coefficients are held constant over the global time step. However, the entire RHS of Eq. (3.19) is updated at each electron time step since the mean electron energy, ϵ, and therefore the gradients in the electron energy, are updated accordingly. Coefficients A_1 through A_{16} as well as the discretizations used within the simulation are denoted in Appendix A.

3.5 Modeling Neutral Particles and Ions

The PIC simulation used in this work was originally developed by Koo and Boyd, [44, 48] and the DK algorithm was originally developed by Hara *et al.* [7, 15]. In this section, the DK and PIC algorithms are described. Note that boundary conditions are detailed separately in Chapter IV. The discretized kinetic grid, shown in Fig. 3.6, is coupled with the electron λ grid (Fig. 3.4) for the full plasma simulation.

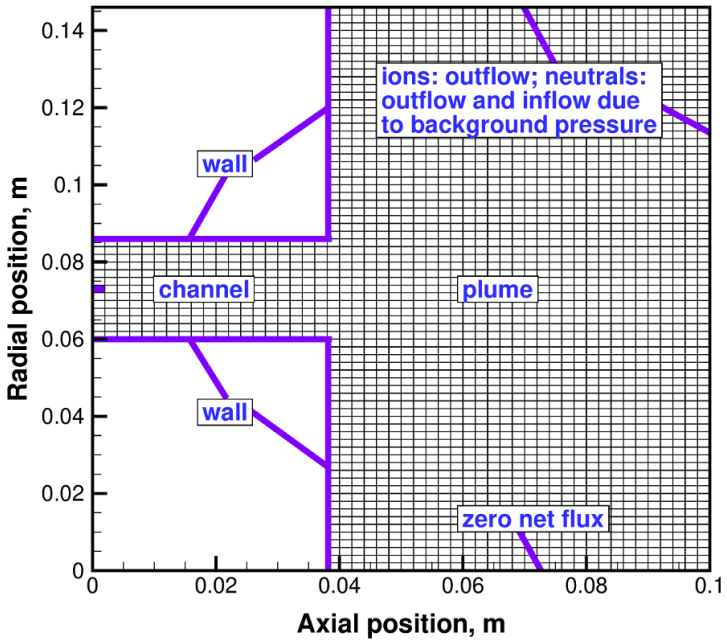

Figure 3.6: Kinetic simulation domain, highlighting boundary conditions.

Strictly speaking, the DK and PIC dimensionalities differ since the former numerical method contains two dimensions in physical and velocity space (2D2V) for both ions and neutral particles, while the latter method models axisymmetric neutral species (2D3V). Neither simulation considers the azimuthal velocity component for ions since the maximum ratio of $\frac{\mathbf{v}_i \times \mathbf{B}}{\mathbf{E}}$ is very small ($\leq 4\%$) for the conditions of interest [42] It is verified in Appendix B that the differences between the planar and axisymmetric algorithms for neutral particles are insignificant for the present work. Therefore, the conventional notation to describe an axial-radial (z, r) domain is used.

3.5.1 Discretized Direct Kinetic Model

In the 2D DK simulation, there are four dimensions: two in physical space and two in velocity space (2D2V). The two species include singly charged ions and neutral atoms, whose kinetic equations are described by Eqs. (2.38a) and (2.38b), respectively. A depiction of spatial and velocity grid discretizations is included in Fig. 3.7. Without the source term,

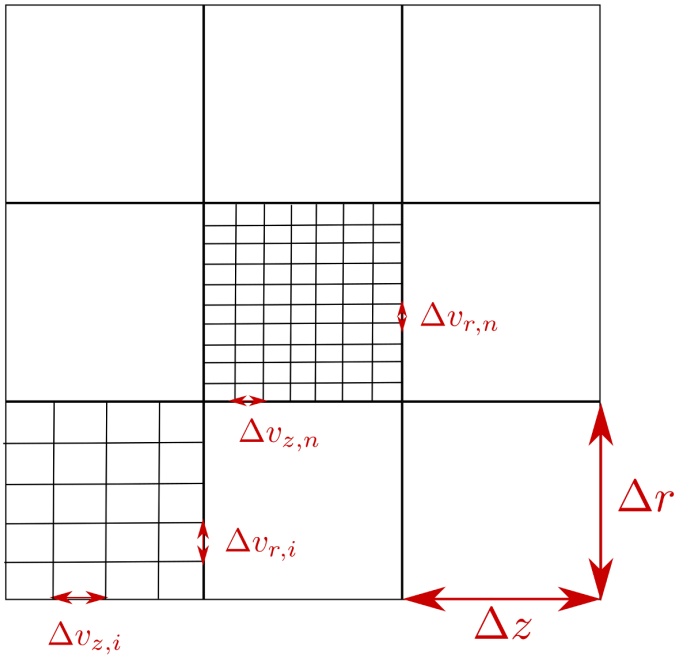

Figure 3.7: Representative spatial and velocity grid discretizations for neutral atoms and ions. Drawing not to scale.

the ion kinetic equation is integrated in time using a second-order accurate Runge-Kutta method without any dimensional splitting:

$$\frac{\partial f_i}{\partial t} + v_z \frac{\partial f_i}{\partial z} + v_r \frac{\partial f_i}{\partial r} + \frac{eE_z}{m_i}\frac{\partial f}{\partial v_z} + \frac{eE_r}{m_i}\frac{\partial f}{\partial v_r} = 0$$

$$\Longrightarrow$$

$$\frac{\partial f}{\partial t} + L[f(z, r, v_z, v_r)] = 0 \tag{3.20}$$

where $L[f(z, r, v_z, v_r)]$ consists of the physical and velocity advection terms. The second-order Runge-Kutta method can be written as:

$$f^* = f^q + \Delta t L(f^q) \tag{3.21}$$

so that

$$f^{q+1} = f^q + \frac{\Delta t}{2}[L(f^q) + L(f^*)] \tag{3.22}$$

where q indicates the time step. The same technique is applied for neutral atoms.

Spatial integration considers the discretized VDF, $f = f_{kz,kr,jz,jr}$, where k indicates a spatial index and j indicates a velocity index. The finite volume solution technique uses a modified Arora-Roe limiter to calculate the numerical flux of kinetic quantities through each cell interface. Two computational ghost cells adjacent to each boundary cell are available for information exchange. At simulation boundaries, zeroth order extrapolation of the VDF is used, implying that updates at the boundaries are of first order accuracy. The flux scheme and DK boundary conditions, including the injection technique, are discussed in detail in Chapter IV.

The source term in Eq. (2.38a) is accounted for via ionization collisions. To account for DK ionization events, the ionization rate is multiplied by the normalized distribution function in each Cartesian cell at each time step,

$$S_i(\mathbf{v}, \mathbf{z}, t) = \beta \dot{n}_{ion} \hat{f}_n(\mathbf{v}) \tag{3.23}$$

where β is +1 or -1, depending on whether an ion is created or a neutral atom is lost. For each ionization event, a neutral atom is deleted, and an ion with the identical velocity and physical location is created, conserving the total number of particles in the system.

For the DK method, mean properties in each cell including the density and velocity are found by taking moments of the VDF:

$$n(\mathbf{z}, t) = \int_{-\infty}^{+\infty} f(\mathbf{z}, \mathbf{v}, t) d\mathbf{v} \tag{3.24}$$

$$\mathbf{u}(\mathbf{z},t) = \int_{-\infty}^{+\infty} \mathbf{v}\hat{f}(\mathbf{z},\mathbf{v},t)d\mathbf{v} \tag{3.25}$$

where $\hat{f}$ is the normalized VDF ($\hat{f} = f/n$).

3.5.2 Discretized Particle-in-Cell Model

In the PIC simulation, singly charged ions and neutral atoms are modeled using a technique that simulates the motion of macroparticles via a second order, classical leapfrog scheme. Particle positions are calculated on integer time steps while velocities are calculated at half time steps relative to the particle positions per Eq. (3.26) and Eq. (3.27), respectively,

$$\mathbf{z}(t+\delta t) = \mathbf{z}(t) + \mathbf{u}\left(t + \frac{\delta t}{2}\right)\Delta t \tag{3.26}$$

$$\mathbf{u}\left(t + \frac{\delta t}{2}\right) = \mathbf{u}\left(t - \frac{\delta t}{2}\right) + \frac{e\mathbf{E}(t)}{m_i}\Delta t \tag{3.27}$$

Note that velocities are calculated in Cartesian coordinates, so after each position update, the neutral velocity vector must be rotated back to the $(z, r, \theta = 0)$ plane.

Macroparticles are weighted to the nodes of the Cartesian grid in order to evaluate the particle density. To accomplish this weighting, axial and radial shape factors are used. In the axial direction, shape factors are obtained via linear interpolation:

$$S_{kz} = \frac{z_{kz+1} - z}{z_{kz+1} - z_{kz}} \tag{3.28a}$$

$$\begin{aligned} S_{kz+1} &= \frac{z - z_{kz}}{z_{kz+1} - z_{kz}} \\ &= 1 - S_{kz} \end{aligned} \tag{3.28b}$$

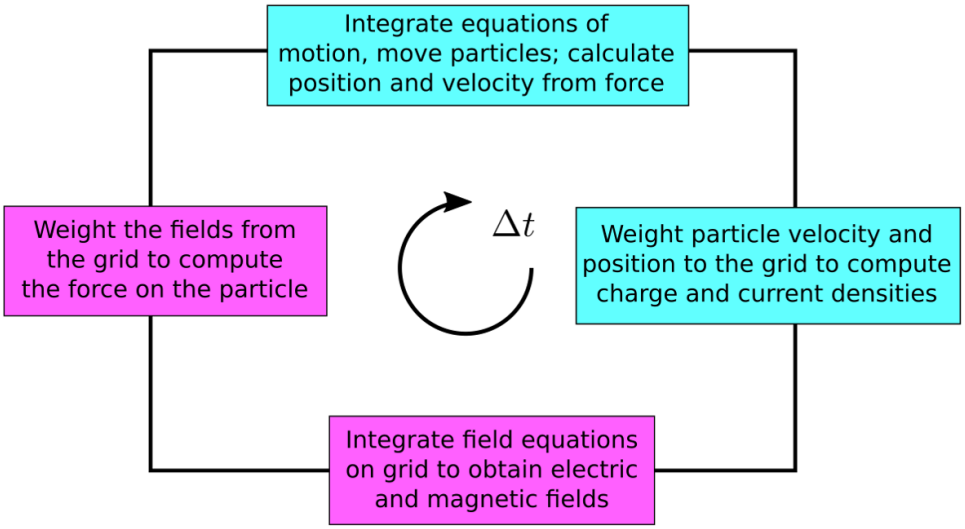

Figure 3.8: A typical PIC simulation cycle. Particle-related steps are shown in blue, while grid-related steps are shown in purple. [66]

In the radial direction, the following shape factors are applied: [48]

$$S_{kr} = \frac{(r_{kr+1} - r)(2r_{kr+1} + 3r_{kr} - r)}{2(r_{kr+1}^2 - r_{kr}^2)} \tag{3.29a}$$

$$\begin{aligned} S_{kr+1} &= \frac{(r - r_{kr})(3r_{kr+1} + 2r_{kr} - r)}{2(r_{kr+1}^2 - r_{kr}^2)} \\ &= 1 - S_{kr} \end{aligned} \tag{3.29b}$$

At a given node, the particle density is ascertained by taking the product of the macroparticle weight and the two relevant shape factors. A general PIC simulation cycle over a single time step is depicted in Fig. 3.8. Note that, in the HET simulation, the magnetic field is prescribed and therefore does not require an update at each time step.

Ionization collisions are calculated using the MCC model. [66] In the MCC model, source particles collide with a target "cloud", which implies that energy is not inherently conserved. However, if the collision frequency is not very high, then the target species

is negligibly affected by collisions, making the MCC model useful. The MCC algorithm calculates the probability of an electron-neutral collision from the ground state based on the local plasma density, electron energy, and time step. If a collision occurs, the neutral macroparticle is changed into a singly charged ion macroparticle with the same physical properties at the parent neutral macroparticle. In Koo's work, it was determined that in practice, due to the low ionization probability at small time steps, the number of ion macroparticles generated is too low for acceptable particle statistics, so a collision multiplier technique is applied. [48] The modified collision probability, P_c^*, is a function of the collision multiplier, γ, and the collision probability, P_C:

$$P_C^* = \gamma P_C \tag{3.30}$$

The multiplier can be increased if the total number of ion macroparticles in the domain is below the target value. The modified value, γ^*, is calculated as:

$$\gamma^* = \frac{\sqrt{\gamma P_C}}{P_C} \tag{3.31}$$

and the collision multiplier is modified accordingly. The majority of simulation results discussed in this work use a collision multiplier, $\gamma = 4$, which lies in the recommended range $2 \leq \gamma \leq 16$. [48]

The variable collision multiplier is known to influence the modeled physics to some extent. [48] Therefore, its usage is reviewed in the present study. The premise for the utilization of the multiplier is based on the fact that the number of ion macroparticles is too low for acceptable particle statistics. Therefore, if an acceptable number of neutral macroparticles are present in the simulation at all times, collision statistics should be acceptable, and the utility of the collision multiplier will be reduced. This is investigated in Chapter V.

CHAPTER IV

Direct Kinetic Boundary Conditions

In this chapter, conservative boundary conditions for the two-dimensional DK simulation are discussed in detail. DK boundary conditions are fairly straightforward to implement at open boundaries, but it requires some attention to ensure that the particle count is conserved at other types of boundaries. For example, in order to accurately calculate particle recombination at a wall boundary, the ion flux that passes through each individual boundary cell must be calculated accurately, stored, and converted to neutral VDF coordinates for particle re-entry into the domain. To ensure that the particle flux calculations at boundaries are straightforward, Section 4.1 reviews the flux calculation in phase space. Section 4.2 discusses DK boundary conditions including wall collisions and particle injection in the context of a hybrid-DK simulation of a HET discharge plasma. Section 4.3 discusses a sheath injection boundary condition that is unique to a DK plasma sheath simulation which is described in Chapter VI.

4.1 Flux Calculation in Phase Space

Considering the advection equation in one dimension, the discretized equation in physical, axial space can be written as a function of the flux, F, which passes through the kth cell's

interfaces, located at $k-1/2$ and $k+1/2$:

$$f_k^{q+1} = f_k^q - (F_{k+1/2} - F_{k-1/2}) \tag{4.1}$$

where $F = \frac{v_z \Delta t}{\Delta z} f = cf$ and c represents the Courant Friedrichs Lewy (CFL) number in physical space. f is not known at either cell interface, and the monotonic upwind scheme for conservation laws (MUSCL) become useful in estimating this property and thus calculating the flux through a cell interface. The MUSCL scheme enables the calculation of flux terms at higher than first order accuracy and is described in Reference [87]. To achieve numerical stability in the DK simulation, the CFL condition must be met, i.e. the total CFL number should always be less than one, namely,

$$\sum_i \left(\frac{\max |v_i| \Delta t}{\Delta z_i} + \frac{\max |a_i| \Delta t}{\Delta v_i} \right) \leq 1 \tag{4.2}$$

where v is the characteristic velocity, a is the characteristic acceleration, Δz and Δv are cell sizes in physical and velocity space, and i denotes the dimension.

According to the MUSCL scheme, the flux due to positive axial advection through the interface *k-1/2* can be described as:

$$F_{k-1/2}^{+} = cf_{k-1} + \frac{(1-|c|)c}{2}(f_k - f_{k-1})\Psi r_{k-1/2} \tag{4.3}$$

where Ψ is the nonlinear limiter function, and $r_{k-1/2}$ is the slope factor, which indicates the smoothness of the neighboring values. For this positive advection case, $r_{k-1/2}$ is dependent on the VDF in the *k*-th cell and the two adjacent cells upstream, as illustrated in Fig. 4.1. The slope factor is described by:

$$r_{k-1/2} = \frac{f_{k-1} - f_{k-2}}{f_k - f_{k-1}} \tag{4.4}$$

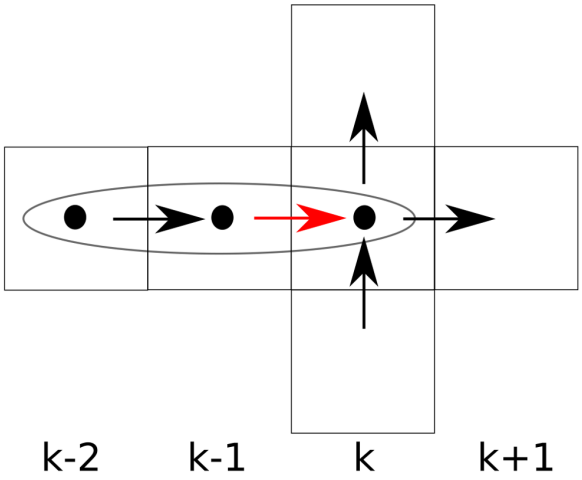

Figure 4.1: Finite volume stencil highlighting incoming flux to cell k at interface $k-1/2$.

The corresponding value of the Arora-Roe limiter, Ψ, can be described by: [88]

$$\Psi = \frac{1+c}{3}(r-1)+1. \tag{4.5}$$

The slope factor, r, is used to achieve monotonicity. For example, if r for the positive advection case is also positive, the second term on the right hand side of Eq. (4.3) contributes to the positive evolution of f. Otherwise, it acts as an anti-diffusive flux term to limit numerical oscillations. For the DK simulation, the Arora Roe limiter is modified, and there are three bounds, given by: [7]

$$\Psi(r) = \begin{cases} 0 & r < 0 \\ \min[2r, \Psi(r)] & 0 \leq r < 1 \\ \min[2, \Psi(r)] & r \geq 1 \end{cases} \tag{4.6}$$

At simulation boundaries, two ghost cells adjacent to each boundary cell are available for information exchange. At these locations, zeroth order extrapolation of the VDF is used, implying that updates at the boundaries are of first order accuracy. Since the same

information is extrapolated to both of the ghost cells adjacent to any boundary, this means that the slope factor is zero, and the flux through the boundary cell is dependent only on the VDF in the cell directly adjacent to the boundary. This is important, as it allows one to ensure strict particle conservation at simulation boundaries. It is worth noting that, if the electric field is non-negligible at a boundary, the advection in velocity space also becomes important, as it may significantly affect the VDF evolution in the boundary cell. This topic is not addressed for boundary condition application in a HET model since a zero-electric field condition is applied at wall boundaries in the device.

4.2 Boundary Conditions in the Hybrid-DK Simulation

In the hybrid-PIC simulation of a HET discharge plasma, it is relatively straightforward to implement boundary conditions. Since the method tracks macroparticles in physical space, it is simple to deduce whether or not a macroparticle has either left the domain or collided with a wall and requires recombination and/or reflection. DK boundary conditions are fairly straightforward to implement at open boundaries, but it requires some attention to ensure that the particle count is conserved during wall collisions. Additionally, it is known that DK methods resolve thermal distributions well but are not ideally suited for beam-type distributions unless the velocity discretization is sufficient to resolve the beam distribution of particles. [12] For this reason, the neutral injection scheme at the anode orifice is also examined in this section.

In the DK model, four types of boundary conditions are implemented at the edges of the simulation domain. For reference, the DK grid, highlighting boundary conditions, is reproduced from Fig. 3.6 and shown in Fig. 4.2. Boundaries include: an outflow condition for ions leaving the thruster domain; outflow with allowance for inflow of neutral particles if there is a nonzero background pressure; a specular reflection (zero net flux) boundary condition at the thruster centerline ($r = 0$); and wall boundaries at which neutral atoms

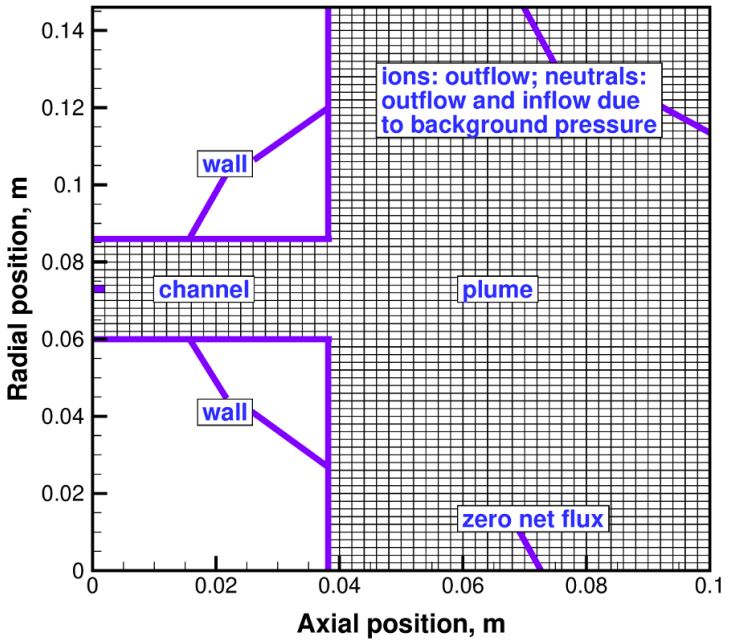

Figure 4.2: DK simulation grid, highlighting boundary conditions.

are diffusely reflected, and ions recombine to reflect diffusely as neutral atoms. Specular reflection is also allowed at the wall boundaries, but for consistency with the comparable hybrid-PIC simulation, it is assumed that particles accommodate completely to the wall temperature for both the DK and PIC simulations. This is considered to be a reasonable assumption since the surface roughness of the ceramic thruster channel walls tends to randomize the distribution of reflected particles.

For the positive axial outflow condition for ions, shown in Fig. 4.3, VDFs in positive, axial velocity space are extrapolated to adjacent ghost cells, and VDFs for negative, axial velocity space in the ghost cells are set to zero. This allows ions to exit across the boundary and ensures that no ions will re-enter the domain. If a finite background pressure is included, a non-zero number of neutral particles are allowed to enter the domain at the open outflow boundaries. This is accomplished by applying a non-zero VDF to the ghost cells such that that neutral atoms will enter the domain at the background pressure according to a biased half Maxwellian distribution at the background temperature, T_{bgnd}. Considering the

same velocity space for neutral particles as is shown in Fig. 4.3 with a finite background pressure, p_{bgnd}, the introduced background density, n_{bgnd}, corresponds to the ideal gas law:

$$n_{bgnd} = \frac{p_{bgnd}}{k_b T_{bgnd}} \tag{4.7}$$

A half Maxwellian VDF biased with axial velocity for $v_z < 0$ corresponds to:

$$f(v_z, v_r) = \begin{cases} \left(\frac{m_i}{2\pi k_b T_{bgnd}}\right) \exp\left(-\frac{m_i}{2k_b T_{bgnd}}(v_z^2 + v_r^2)\right) & v_z \leq 0 \\ 0 & v_z > 0 \end{cases} \tag{4.8}$$

Eq. (4.8) is normalized as:

$$\hat{f}(v_z, v_r) = \frac{f(v_z, v_r)}{\int_{v_{r,min}}^{v_{r,max}} \int_{v_{z,min}}^{0} f(v_z, v_r) dv_z dv_r} \tag{4.9}$$

and $f_{bgnd} = n_{bgnd}\hat{f}(v_z, v_r)$ is applied to the ghost cells for neutral injection into the system at each time step to satisfy the finite background pressure requirement. At the thruster centerline ($r = 0$), a zero net flux condition is applied, and particles that cross the centerline are specularly reflected back into the domain. This is accomplished by first extrapolating the VDF for $v_r < 0$ to the adjacent ghost cells and then performing a coordinate transform on the same portion of the VDF, mirroring it in positive velocity space.

4.2.1 Modeling Wall Collisions

At wall boundaries, ions recombine to neutral atoms and reflect diffusely, and neutral atoms simply reflect diffusely. All derivations in this section refer to the conservation of number density, but in reality, the number of particles in the simulation domain are conserved, since the calculations are performed in each physical cell. For the sake of simplicity, particle reflections at the inner channel wall ($r = 0.06$ m in Fig. 4.2) are considered for the derivations

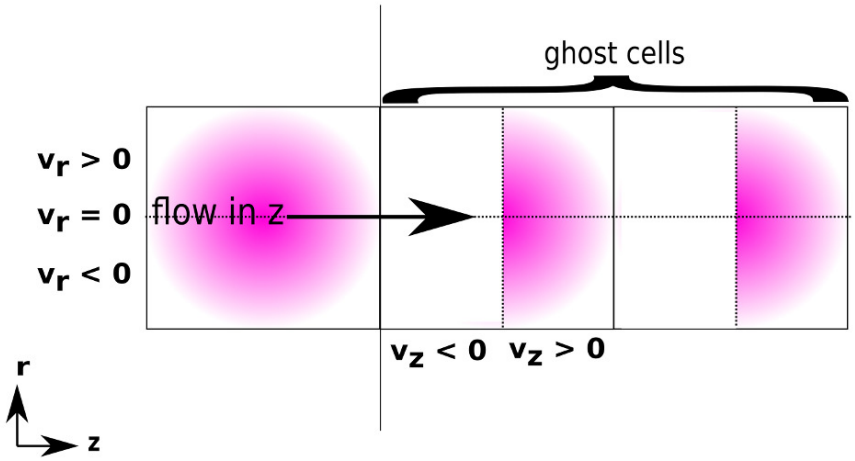

Figure 4.3: Example schematic of VDF extrapolation at an outlet boundary for ions. Positive ions leave through the boundary, and no particles re-enter the domain.

in this section.

For neutral particles, the outgoing VDF is simply extrapolated to the neighboring ghost cells so that particles are advected out of the simulation domain, i.e. they collide with the inner wall according to the first term in Eq. (4.3). The number of particles that fluxes through the interface over the course of a single time step corresponds to:

$$\Gamma_{n,out} = \frac{\int_t \int_{v_{r,min}}^{0} \int_{v_{z,min}}^{v_{z,max}} |v_r| f_{n,out}(v_z, v_r) dv_z dv_r dt}{\int dr} \tag{4.10}$$

where $v_{z,min}$ and $v_{z,max}$ represent the limits of velocity space in the z-direction, $v_{r,min}$ represents the lower limit of velocity space in the r-direction, and $f_{n,out}$ is the non-normalized VDF in the cell inside the domain, adjacent to the boundary. Since particles are advected in the negative r direction, toward the inner wall of the thruster, only negative velocity space ($v_r < 0$) is considered. The number of particles that flux out of the system is equal to the number of particles that re-enter the domain, i.e. $\Gamma_{n,in} = \Gamma_{n,out}$. The incoming particle flux is described by:

$$\Gamma_{n,in} = \frac{\int_t \int_{0}^{v_{r,max}} \int_{v_{z,min}}^{v_{z,max}} v_r f_{n,in}(v_z, v_r) dv_z dv_r dt}{\int dr} \tag{4.11}$$

where $f_{n,in}$ is dependent on the reflection (or emission) mechanisms, such as specular and diffuse reflections, and it conforms to:

$$f_{n,in}(v_z, v_r) = n_n \hat{f}_{n,in}(v_z, v_r) \tag{4.12}$$

where $\hat{f}_{n,in}$ is the normalized, reflected VDF. The reflected VDF into the domain at the inner channel wall ($v_r > 0$) is described by a half Maxwellian distribution at the wall temperature, assuming a perfectly diffuse reflection. The VDF can be written as:

$$f_{Maxwell}(v_z, v_r) = \begin{cases} \left(\frac{m}{2\pi k_b T_w}\right) \exp\left(-\frac{m}{2k_b T_w}(v_z^2 + v_r^2)\right) & v_r > 0 \\ 0 & v_r \leq 0 \end{cases} \tag{4.13}$$

where T_w is the wall temperature. This is normalized as:

$$\hat{f}_{n,in}(v_z, v_r) = \frac{f_{Maxwell}(v_z, v_r)}{\int_0^{v_{r,max}} \int_{v_{z,min}}^{v_{z,max}} f_{Maxwell}(v_z, v_r) dv_z dv_r} \tag{4.14}$$

Since $\hat{f}_{n,in}$ is known, Eq. (4.12) is simply inserted into Eq. (4.11), and n_n is calculated by setting equal the number of particles that flux out of and into the system.

The ion advection algorithm is conducted prior to the neutral advection algorithm over the course of a single time step so that the appropriate information can be stored and transferred to the neutral subroutine, and recombined neutrals can then be introduced into the simulation domain in the same manner as reflected neutrals. The primary challenge is to ensure that the number of particles advected out of the domain, subject to the ion CFL condition, is equal to the number of particles that return, subject to neutral advection. Additionally, it is necessary to consider the fact that advection in time conforms to a second-order Runge-Kutta method. This means that there are two steps for integration, and advection in r occurs twice over a single time step. The count of fluxed ions, $\Gamma_{i,out}$, is calculated via the

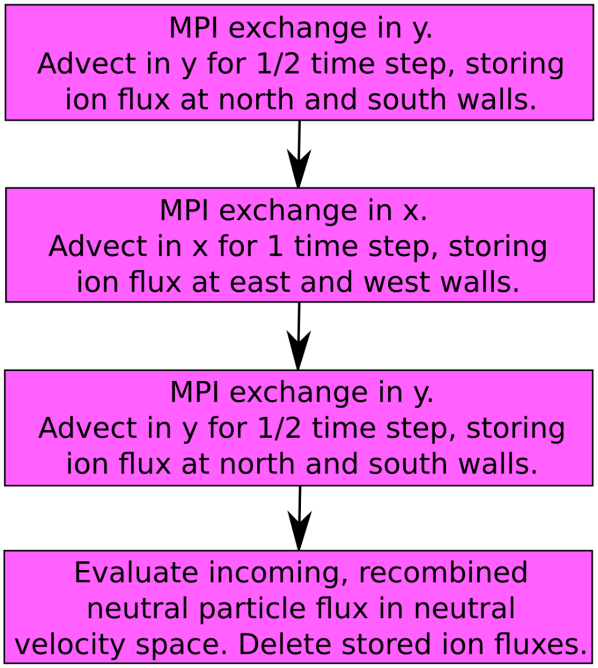

Figure 4.4: The sequence of events for ion advection and boundary condition implementation at the wall boundaries over a course of a single time step, assuming the CFL condition is met.

expression in Eq. (4.10) using the parameters for ion velocity space. It is summed over two integration steps and stored. The recombined density introduced to the domain over a full time step then conforms to:

$$n_{n,re} = \frac{\Gamma_{i,out}}{\int_t \int_0^{v_{r,max}} \int_{v_{z,min}}^{v_{z,max}} v_r \cdot \hat{f}(v_z, v_r) dv_z dv_r dt / \int dr} \tag{4.15}$$

so that $\Gamma_{i,out} = \Gamma_{n,re}$. The recombined neutral density is multiplied by the normalized distribution function, as in Eq. (4.12), to calculate the reflected VDF. The VDF for all reflected particles is described by:

$$f_{n,in}(v_z, v_r) = (n_n + n_{n,re}) \hat{f}_{n,in} \tag{4.16}$$

The sequence of events for ion advection at the wall boundaries over a single time step is shown in Fig. 4.4.

4.2.2 Neutral Injection at the Anode

In early comparisons of hybrid-PIC and hybrid-DK HET simulations, it became apparent in the results that the injection parameters for the two models may not correspond well with one another. [89] Thus, a study is conducted to ensure that they do. For the hybrid-DK simulation, the input parameters for neutral injection at the anode are the mass flow rate, $\dot{m}$, and the radial location of the anode injector, located at an axial position of $z = 0$. The anode injector includes an integer number of computational cells. A neutral density is assigned to the ghost cells adjacent to the inlet assuming that particles are injected at a thermal velocity corresponding to the anode inlet temperature, i.e.

$$n_{inlet} = \frac{\dot{m}}{m_i < v_z > A} \tag{4.17}$$

where $A = \pi(r_2^2 - r_1^2)$ is the cross sectional area of the slit through which the particles enter, and $< v_z >$ is the average velocity of a half Maxwellian distribution biased with axial velocity at the anode temperature. Strictly speaking, the inlet area should correspond to the two-dimensional DK domain, but instead it corresponds to that used in the axisymmetric PIC simulation so that the injection parameters are comparable.

The average input velocity is:

$$< v_z >= \int_{v_{r,min}}^{v_{r,max}} \int_0^{v_{z,max}} v_z \left(\frac{m_i}{2\pi k_b T_a}\right) \exp\left(-\frac{m_i}{2k_b T_a}(v_z^2 + v_r^2)\right) dv_z dv_r \tag{4.18}$$

where T_a is the anode reservoir temperature. The analytical values for the integrals in Eq. (4.18) are calculated using $I_1(a) = \frac{1}{2a}$ and $I_0(a) = \frac{1}{2}\left(\frac{\pi}{a}\right)^{\frac{1}{2}}$where $I_n(a) = \int_0^\infty x^n \exp(-ax^2)dx$, and the expression simplifies to: [6]

$$< v_z >= \sqrt{\frac{k_b T_a}{2\pi m_i}} \tag{4.19}$$

Thus, the flux of particles through the anode orifice into the simulation domain is:

$$\Gamma_{n,inlet} = \frac{n_{inlet} \int_t \int_{v_{r,min}}^{v_{r,max}} \int_0^{v_{z,max}} v_z \cdot f_{Maxwell}(v_z, v_r) dv_z dv_r dt}{\int dz} \tag{4.20}$$

The resultant particle flux correlates exactly with the standard particle flux calculation for free molecular flow with no stream velocity onto a surface, i.e. $\Gamma = \frac{n}{4}\sqrt{\frac{8k_bT}{\pi m}}$ per unit area, per unit time. [2]

In the hybrid-PIC model, the particle flux through the injection cell's interface is not directly calculated. Instead, the number of particles that ought to be in the vicinity of the anode over a single time step is calculated and generated at $z = 0$, randomly distributed within the height of the anode. Since the density calculation takes into account the volume of a cell, which is $V = \pi(r_2^2 - r_1^2)\Delta z$, the assigned inlet density should be consistent with that applied to the DK simulation. The most probable speed, c_{mp}, for the incoming particle distribution is calculated based on the anode reservoir temperature, $c_{mp} = \sqrt{2k_bT_a}$, and the standard PIC effusion subroutine ensures that particles are injected according to the method laid out by Bird et al, where the normal velocity component is in the axial direction, and the two tangential velocity components that result from this method are used to calculate v_r. [11]

Using the hybrid-DK and hybrid-PIC neutral injection techniques discussed in this section, reasonable agreement is obtained between the two models, as demonstrated in Fig. 4.5 which shows the average hybrid-DK and hybrid-PIC neutral densities and axial velocities along the UM/AFRL P5 HET channel centerline for a neutral-only simulation. Of particular importance is the agreement in the neutral density near the injection site located at $z = 0$. There is a discrepancy in the average axial velocity values, greatest near the anode, and this may be due to the fact that the single-cell DK injector slightly over-calculates properties at the centerline because the velocity space discretization is not fine enough to resolve the beam-type distribution accurately. This is described in Section 4.2.3.

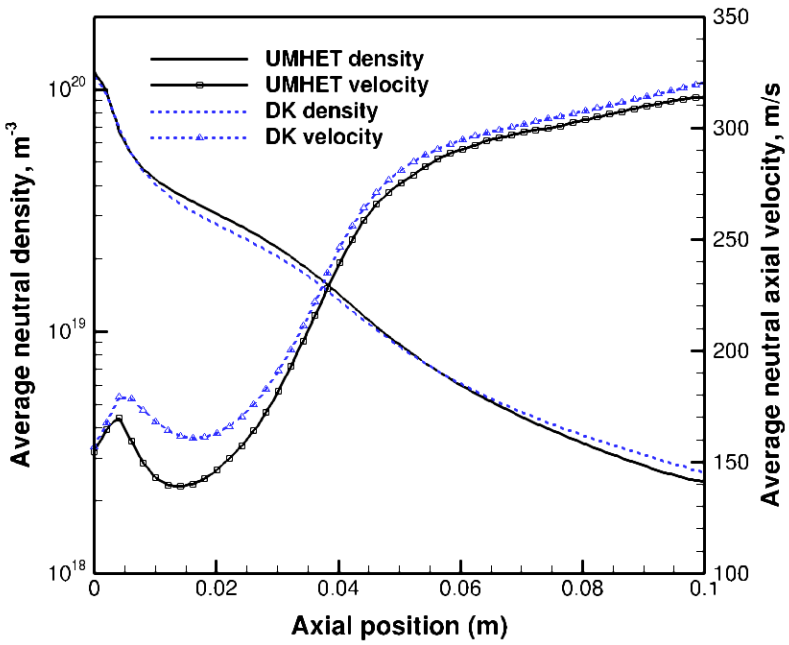

Figure 4.5: Average hybrid-DK and hybrid-PIC (UMHET) neutral densities and axial velocities along the UM/AFRL P5 thruster channel centerline at $t = 2.0$ ms with a sampling rate of 1 μs. The channel exit is located at an axial position of $z = 0.038$ m.

4.2.3 Neutral Injection and Grid Convergence

In this section, the effects of physical and velocity grid discretization in the presence of an incoming jet of neutral particles are examined. DK methods resolve thermal distributions well but are not ideally suited for beam-type distributions unless the velocity discretization is sufficient to resolve the beam distribution of particles. [12] In this section, it is demonstrated that, if an inlet is small compared to the domain size, the resolution of both physical and velocity space with respect to the inlet size are important. Cases are considered for which neutral atoms are injected from the left hand side of the domain through an inlet with a height of 2 mm. The inlet is comprised of one, two, or three cells with coarse or fine velocity grid discretization. The cases are referred to as Cases 1, 2, and 3, respectively, with *a* denoting coarse velocity bins and *b* denoting fine velocity bins. The case details and their associated computational times are shown in Table 4.1. Case 1 has a total of 2515 computational cells. Note that the time step, Δt, changes with cell size so that the

Table 4.1: Neutral injection simulation parameters.

	Δt	$\Delta z, \Delta r$	$\Delta v_z, \Delta v_r$	Wall time
Case 1a	1×10^{-6} s	(2, 2) mm	(25, 10) m/s	0.3 hr/ms
Case 1b	1×10^{-6} s	(2, 2) mm	(10, 4) m/s	2.0 hr/ms
Case 2a	5×10^{-7} s	(1, 1) mm	(25, 10) m/s	1.3 hr/ms
Case 2b	5×10^{-7} s	(1, 1) mm	(10, 4) m/s	5.8 hr/ms
Case 3a	3.33×10^{-7} s	(0.66, 0.66) mm	(25, 10) m/s	9 hr/ms
Case 3b	3.33×10^{-7} s	(0.66, 0.66) mm	(10, 4) m/s	52.6 hr/ms

CFL number is identical for all cases. All processes are parallelized using Message Passing Interface (MPI).

It is evident from the wall times in Table 4.1 that the computational time increases significantly when either physical or velocity space is refined. Note that Case 1 is run on 24 processors, whereas Cases 2 and 3 are run on 40 processors due to memory requirements. It is observed that the change from coarse to fine velocity space discretization for the same physical cell size increases the computational time by an average factor of 5.67 due to the additional computational load on each processor. However, the impact of increasing physical cell count on computational time is not linear. Considering the computational time for the same number of time steps, N, rather than the total wall time per ms of computational data, it is observed that computational time per N time steps increases by a factor of approximately 2 for the doubling of cells from Case 1 to Case 2, whereas the computational time increases by a factor of approximately 9 for the tripling of cells from Case 1 to Case 3 for either coarse of fine velocity bins. Since cases 2 and 3 are run on the same number of processors, it is likely that the processors are not optimized properly for Case 3 and the serial computational load is greatly increased; thus, additional processors should be allocated to optimize the simulation time. It is also important to point out that, in a full plasma simulation, Δt must be much smaller than the values used here to satisfy the CFL condition for ions. Therefore, it is essential to select a grid discretization that will allow for

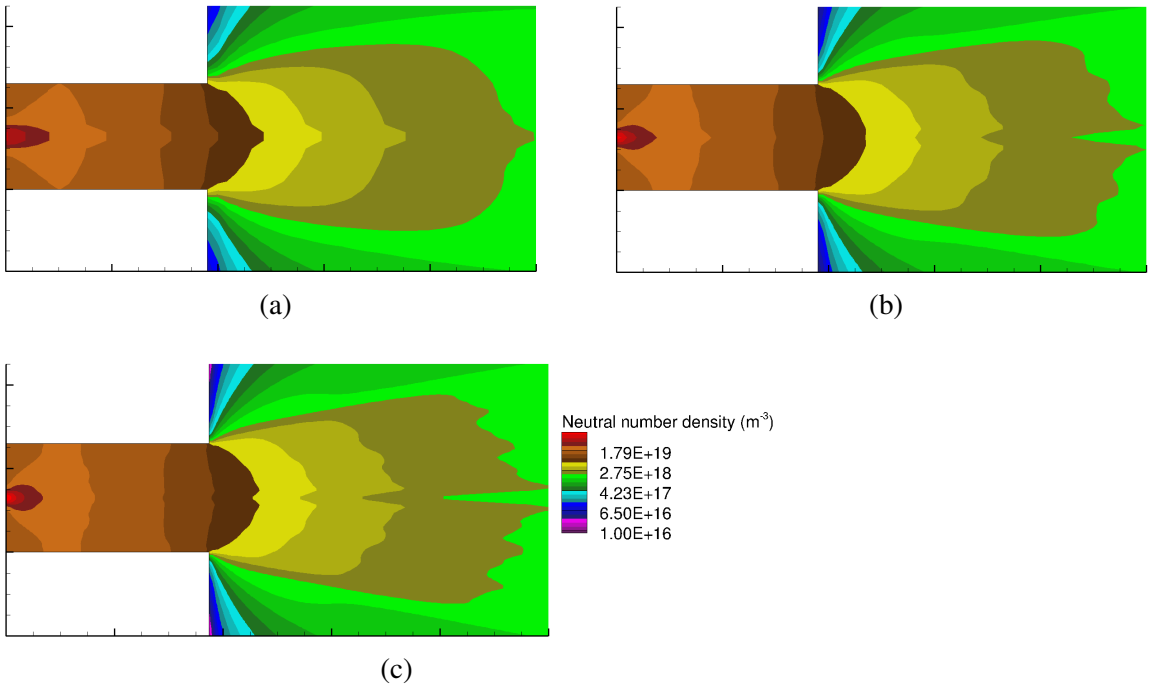

Figure 4.6: Steady-state neutral atom density contours with coarse velocity grid discretizations. (a) Case 1a with 1-cell injector, (b) Case 2a with 2-cell injector, and (c) Case 3a with 3-cell injector.

reasonable resolution but will not lead to intractable simulation times.

Steady state results for the neutral density contours with coarse velocity space in Cases 1-3 are shown in Fig. 4.6. For all cases with coarse velocity space (Figs. 4.6a, 4.6b, and 4.6c), the neutral density profile is not well resolved at the channel centerline, particularly in the plume region. For Case 1a with a single cell at the injector location (Fig. 4.6a), the density at the channel centerline is over-calculated. Particles injected with zero radial velocity will remain at the centerline, since the radially-adjacent cells do not contain any neutral particles moving radially toward the centerline to alter the VDF at that location. For Cases 2a and 3a (Figs. 4.6b and 4.6c), the density at the centerline in the plume region is under-calculated. Since multiple cells are used for injection, the radial flux between the cells at the centerline is non-zero, and the resultant number of particles that leave radially outward from the centerline is slightly over-calculated.

Results from cases 1b, 2b, and 3b with a larger number of velocity bins are shown

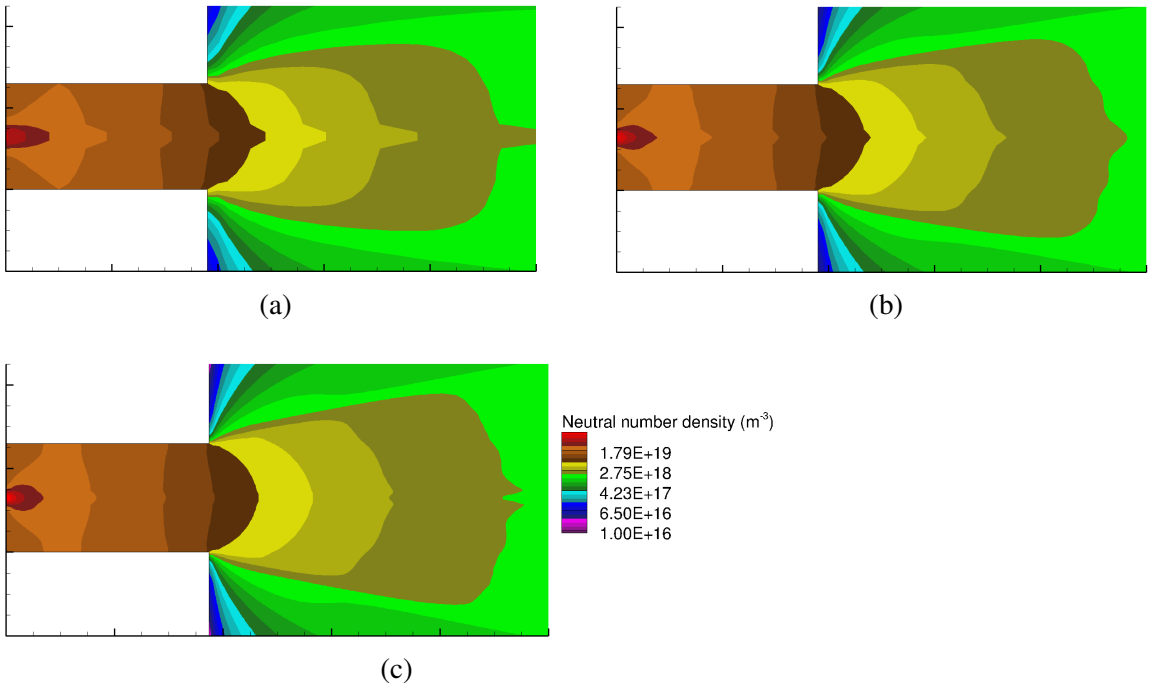

Figure 4.7: Steady-state neutral atom density contours with fine velocity grid discretizations. (a) Case 1b with 1-cell injector, (b) Case 2b with 2-cell injector, and (c) Case 3b with 3-cell injector.

in Figs. 4.7a, 4.7b, and 4.7c, respectively. Case 1b (Fig. 4.7a) actually has more neutral particles on centerline than the coarse case in Fig. 4.6a, implying that VDF resolution is not useful for this single-cell injector case. Finer VDFs, however, are useful for Cases 2b and 3b which are shown in Figs. 4.7b and 4.7c, respectively. The level of improvement is similar for the 2-cell and 3-cell injector cases. For the 2-cell case, the density at the centerline is no longer under-calculated (Fig. 4.7b).

To demonstrate the sensitivity to velocity bin size, VDFs in the plume region are compared in Fig. 4.8 for the 3-cell injector (Case 3). For this case, additional velocity bins result in an improved neutral density profile in Fig. 4.7c. The VDF in Fig. 4.8a corresponds to the density profile in Fig. 4.6c, and the VDF in Fig. 4.8b corresponds to the density profile in Fig. 4.7c. It is clear that the more highly resolved VDF in Fig. 4.8b has a much larger value, centered at ($v_r = 0$), which corresponds with more neutral particles at that location.

Based on the results for the injection cases, it appears that it is preferable to utilize two

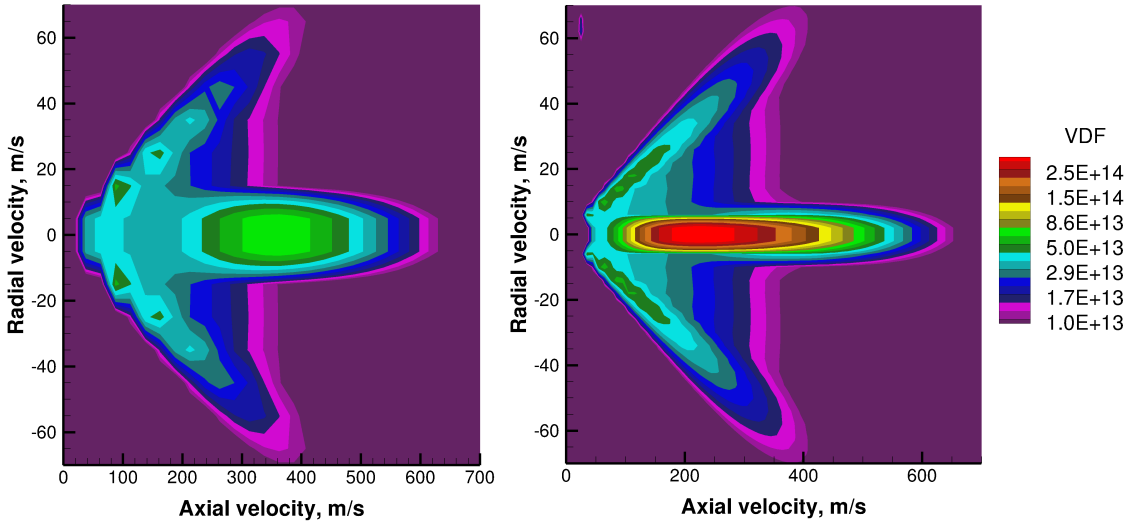

(a) (b)

Figure 4.8: Zoomed-in VDFs (arbitrary units) for the middle cell of the three-cell injector ($\Delta z = \Delta r = 0.66$ mm) near the right hand side of the domain at $z = 0.96$ m. Shown are (a) $\Delta v_z = 25$ m/s, $\Delta v_r = 10$ m/s and (b) $\Delta v_z = 10$ m/s, $\Delta v_r = 4$ m/s.

cells for neutral atom injection in the two-dimensional DK simulation if fine velocity space discretization for neutrals is possible, since this case (Case 2b) results in a reasonable distribution of neutral particles in Fig. 4.7b. To ascertain whether or not the two-cell injector containing cells of 1 mm height is superior to a single-cell injector with the same cell size (1 mm height), another case is simulated for which the cell size and velocity discretization from Case 2b are applied; however, only one cell is assigned for the inlet, and it is located at the centerline of the channel. The results in Fig. 4.9 confirm that the two-cell injector in Fig. 4.9a (Case 2b) resolves the neutral atom density downstream of the injector more accurately than the one-cell injector in Fig. 4.9b. Similar to Case 1, the one-cell injector over-calculates the density at the channel centerline.

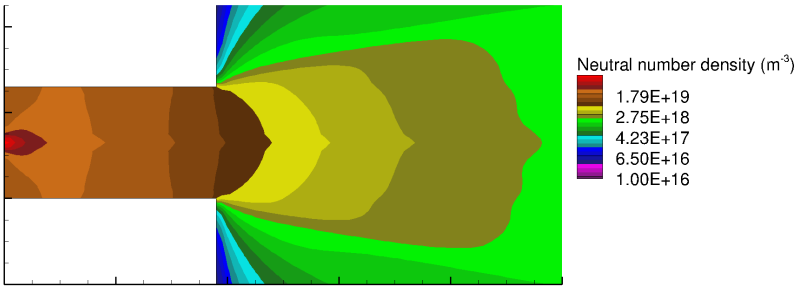

(a)

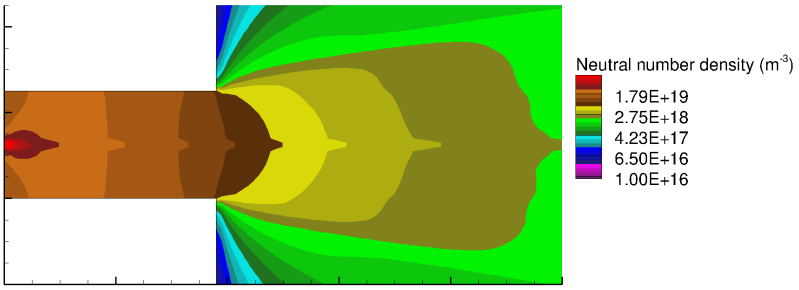

(b)

Figure 4.9: Neutral density contour comparisons for (a) a two-cell injector (Case 2b) versus (b) a one-cell injector with identical physical and velocity grid discretizations.

4.3 DK Boundaries for a Plasma Sheath Simulation

In Chapter VI, the theory, numerical method, implementation, and results are discussed for a two-dimensional plasma sheath model. In this section, the DK boundary conditions for this model are discussed. Briefly, the simulation domain is bounded by an electrically inhomogeneous, conducting wall on the left hand side ($\phi = V_{d1}$ and $\phi = V_{d2}$) and a quasineutral plasma at the sheath edge on the domain's right hand side. Between these two boundaries, an ion-attracting plasma sheath forms near the wall since there is a potential drop ($V_d < 0$). The simulation setup with boundary conditions is shown in Fig. 4.10. Electrons and ions are injected into the collisionless simulation domain on the right hand side (plasma sheath edge), and particles are absorbed at the wall on the left hand side, i.e. there is no secondary electron emission (SEE) or particle reflection back into the plasma. At the top and bottom of the domain, the plasma is relatively far from the discontinuity

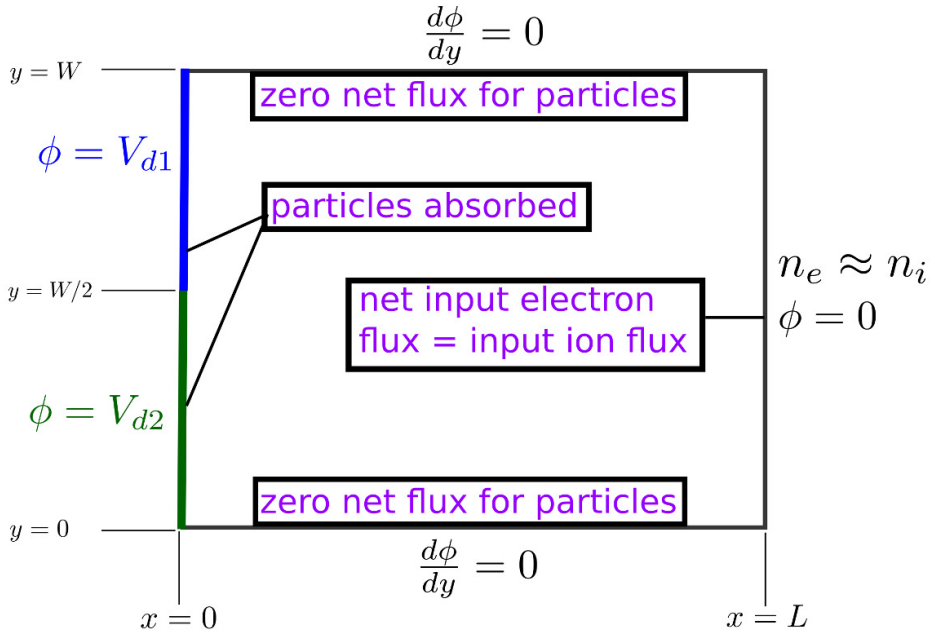

Figure 4.10: Plasma sheath domain. DK boundary conditions are highlighted in purple.

in the potential at $y = W/2$. Therefore, it is assumed that the potential has a zero-slope condition in the y-direction at these boundaries. To ensure that there is minimal impact from outward streaming particles, a zero net flux condition is set for ions and electrons at the upper and lower boundaries.

4.3.1 Controlling the Particle Flux at the Sheath Edge

The primary challenge for DK boundary conditions in the context of the plasma sheath simulation is to ensure that the incoming particle flux at the right hand side of the domain, i.e. the injection site, is appropriately regulated for both ions and electrons. Ideally, the injection site at the plasma edge will exhibit quasineutrality ($n_e = n_i$) in conjunction with a zero electric field condition. The electric field at the sheath edge, E_s, is determined by

the charge accumulated by the ion and electron fluxes, given by [7]:

$$E_s = \frac{Q}{\epsilon_0} = -\frac{e}{\epsilon_0}\int_{t'=0}^{t'=t}(J_{is} - J_{es})dt' \tag{4.21}$$

where Q is the charge accumulated at the sheath edge, J_{is} is the ion particle flux, and J_{es} is the electron particle flux. From Eq. (4.21), it is clear that if the incoming electric field should be zero, then the incoming particle fluxes must be identical. Ions and electrons enter the domain at the injection plane with half Maxwellian distributions at their respective ion and electron temperatures, biased with velocity in the x-direction. Due to their relatively high temperature and low mass compared to ions, electrons move very quickly. As such, to balance the fluxes at the entrance plane, a finite number of electrons leave the simulation domain. It is not possible to control the outgoing flux of electrons, but it is possible to regulate the incoming flux of electrons so that the net incoming flux of electrons is equal to the desired incoming flux of ions. Note that, to ensure that a finite electric field will not grow in the vicinity of this boundary, zeroth order extrapolation of the VDF is used for the two cells inside the simulation domain, directly adjacent to the boundary.

4.3.1.1 Incoming Ion Flux

The simulation domain is first populated with a quasineutral plasma everywhere. Consider first the ion species for the flux balance in a cell located at the plane for incoming particles. The desired total number density of ions in the boundary cell corresponds to n_{i0}. Most ions travel toward the wall with a negative velocity, but a small portion of ions may leave the domain through the boundary cell's right interface, corresponding to:

$$\Gamma_{i,out,right} = \frac{\int_t \int_{v_{yi,min}}^{v_{yi,max}} \int_0^{v_{xi,max}} v_{xi} \cdot f_{i,out}(v_{xi}, v_{yi}) dv_{xi} dv_{yi} dt}{\int dx} \tag{4.22}$$

where i is the subscript for ions. Ions that leave the domain should be re-injected so that the electric field cannot grow in the boundary cell. Taking into account the desired sheath

edge ion density and the density of ions that have fluxed out of the system, the total source density, $n_{s,i0}$, assigned to the ghost cell adjacent to the boundary cell at the sheath edge is described by:

$$n_{s,i0} = \frac{\Gamma_{i,out,right}}{\int_t \int_{v_{yi,min}}^{v_{yi,max}} \int_{v_{xi,min}}^{0} |v_{xi}| \cdot \hat{f}_i(v_{xi}, v_{yi}) dv_{xi} dv_{yi} dt / \int dx} + n_{i,0} \tag{4.23}$$

Thus, the incoming ion flux through the boundary cell interface over a single time step corresponds to:

$$\Gamma_{i,in} = n_{s,i0} \frac{\int_t \int_{v_{yi,min}}^{v_{yi,max}} \int_{v_{xi,min}}^{0} v_{xi} \cdot \hat{f}_i(v_{xi}, v_{yi}) dv_{xi} dv_{yi} dt}{\int dx} \tag{4.24}$$

4.3.1.2 Incoming Electron Flux

In the boundary cell, electrons may enter and exit through the left interface of the cell (toward the simulation domain), and they may also leave through the cell's right interface, exiting the simulation domain. Thus, the net outgoing electron flux from the boundary cell must consider all of these contributions so that it may be replenished by the appropriate incoming electron flux. These fluxes are described by the following expressions:

$$\Gamma_{e,out,right} = \frac{\int_t \int_{v_{ye,min}}^{v_{ye,max}} \int_{0}^{v_{xe,max}} v_{xe} \cdot f_{e,out,right}(v_{xe}, v_{ye}) dv_{xe} dv_{ye} dt}{\int dx} \tag{4.25a}$$

$$\Gamma_{e,out,left} = \frac{\int_t \int_{v_{ye,min}}^{v_{ye,max}} \int_{v_{xe,min}}^{0} |v_{xe}| \cdot f_{e,out,left}(v_{xe}, v_{ye}) dv_{xe} dv_{ye} dt}{\int dx} \tag{4.25b}$$

$$\Gamma_{e,in,left} = \frac{\int_t \int_{v_{ye,min}}^{v_{ye,max}} \int_{0}^{v_{xe,max}} v_{xe} \cdot f_{e,in,left}(v_{xe}, v_{ye}) dv_{xe} dv_{ye} dt}{\int dx} \tag{4.25c}$$

The net outgoing electron flux adds the contribution from the outgoing fluxes and subtracts the contribution from the incoming flux through the left interface of the cell. The incoming electron flux through the right interface of the boundary cell should replace the net loss of electrons in addition to the contribution of $n_{e0} = n_{i0}$ over a single time step. Thus, the incoming electron flux through the right face of the boundary cell corresponds to:

$$n_{s,e0} = \frac{\Gamma_{e,out,right} + \Gamma_{e,out,left} - \Gamma_{e,in,left}}{\int_t \int_{v_{ye,min}}^{v_{ye,max}} \int_{v_{xe,min}}^{0} |v_{xe}| \cdot \hat{f}_e(v_{xe}, v_{ye}) dv_{xe} dv_{ye} dt / \int dx} + \frac{n_{i,0} \int_t \int_{v_{yi,min}}^{v_{yi,max}} \int_{v_{xi,min}}^{0} |v_{xi}| \cdot \hat{f}_i(v_{xi}, v_{yi}) dv_{xi} dv_{yi} dt / \int dx}{\int_t \int_{v_{ye,min}}^{v_{ye,max}} \int_{v_{xe,min}}^{0} |v_{xe}| \cdot \hat{f}_e(v_{xe}, v_{ye}) dv_{xe} dv_{ye} dt / \int dx} \tag{4.26}$$

where the incoming ion flux (second term on the right hand side of Eq. (4.26)) is transformed from ion velocity space to electron velocity space.

4.4 Summary

This chapter discusses direct kinetic boundary conditions that are critical to the success of both the hybrid-DK simulation of a discharge plasma in a HET and to a two-dimensional DK plasma sheath simulation. The boundaries discussed in detail include wall collisions, particle injection from an anode orifice, and a zero-electric field condition at the edge of a plasma sheath. The methods discussed for these boundaries all require that the particle flux is properly calculated and controlled when possible in order to effectively and conservatively regulate the behavior of the plasma at a simulation boundary.

CHAPTER V

A Two-Dimensional Hybrid-Direct Kinetic Simulation of a Hall Thruster

The intent of the present chapter is to compare the hybrid-DK simulation with a comparable hybrid-PIC simulation and demonstrate that the DK algorithm reduces the level of statistical noise in the simulation results while obtaining similar time-averaged results. This comparison process is known as *benchmarking*. Benchmarking is useful to ascertain the performance of a new numerical method compared to an existing method, and it is particularly important for methods that model physically dynamic systems such as the HET. [20] Note that the equations and numerical implementation for this effort are discussed in Chapters II and III, and conservative boundary conditions are introduced in Chapter IV. In this chapter, the HET configuration is discussed in Section 5.1; the simulation setup and computational requirements are given in Section 5.2; and in Section 5.3, results are compared and analyzed for the DK and PIC simulations. Concluding remarks are presented in Section 5.4.

5.1 UM/AFRL P5 Hall Thruster

The P5 Hall thruster, developed jointly by the University of Michigan (UM) and the Air Force Research Laboratory (AFRL), is a SPT that has been used primarily for fundamental physics research. [90, 91] Although it has been characterized experimentally at certain

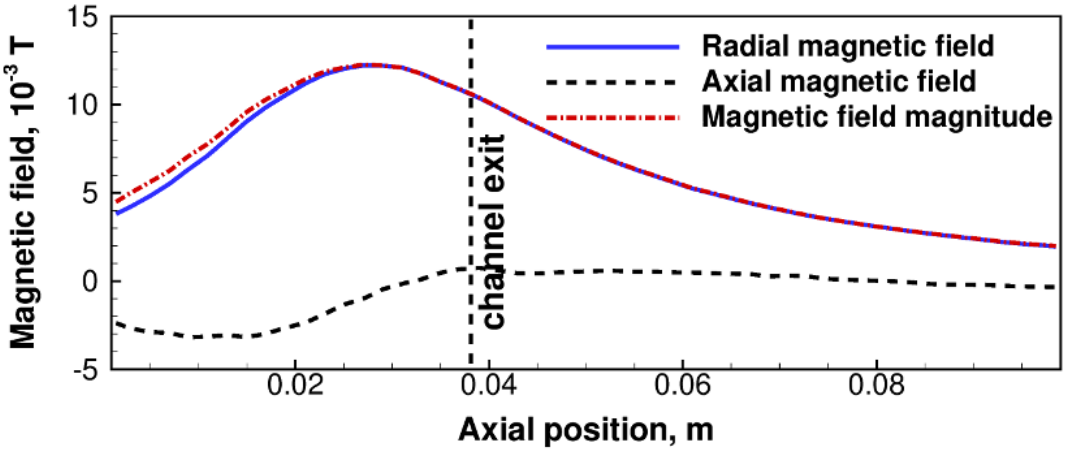

Figure 5.1: UM/AFRL P5 HET magnetic field along the thruster channel centerline.

operating conditions, it is utilized in the present work because it was the focus of Koo and Boyd's previous computational study, and a modified version of their hybrid-PIC simulation is used as the modeling technique to which the DK approach is compared. [44, 48]

Typical SPTs are configured so that the maximum magnetic field is located at or very near the thruster channel exit; near the anode, the magnetic field is typically very low. [25] The P5 magnetic field, shown in Fig. 5.1, is distinct because the maximum magnetic field is located approximately 1 cm axially upstream of the channel exit, and the magnitude of the field at the anode face is approximately 30% of the maximum value. The bulk of ionization occurs upstream of the location of the maximum magnetic field, where electron-neutral collisions are probable and the electron temperature is high enough to promote ionization. At the location of the maximum magnetic field, the Hall parameter is large, i.e. electron confinement is high, and the electron momentum transfer frequency is low. Because the magnetic field is high upstream of the channel exit, the expectation is that the computed ionization region as well as the maximum electric field for the P5 HET will also lie somewhat upstream of the channel exit. These assumptions are in part corroborated by experimental measurements. [90, 92] The P5 experimentally measured properties for a 3 kW power level are compared to those for the 6 kW H6 thruster, a thruster with a more

typical magnetic field configuration, in Fig. 5.2. The P5 maximum electron temperature is located upstream of the channel exit compared to the location of maximum electron temperature for the H6, and the P5 ionization region exhibits two distinct peaks inside the channel. The P5 plasma potential begins to decrease slightly inside the thruster channel and, overall, falls off much more gradually than the corresponding H6 potential.

In the present configuration, the thruster has a mass flow rate of 10.2 mg/s and operates at a discharge voltage of 300 V and a current of 10 A which results in a 3 kW power level. The simulation setup is simplified, as only singly charged ionization collisions are considered, and there is no focused effort to optimize the anomalous electron transport coefficients. Computed macroscopic thruster properties are not validated with experimentally-measured properties since the focus of the present work is to benchmark the two-dimensional hybrid-DK simulation against a comparable hybrid-PIC simulation, similar to the intent of Hara *et al* with respect to the one-dimensional DK algorithm. [15]

5.2 Simulation Setup and Computational Cost

As discussed in Chapter III, the DK simulation is computationally intensive compared to the PIC simulation. The former requires computational memory per cell on the order of $N_{v,z}N_{v,r}$ compared to $4N_p$ for the latter, where N_v is the number of grid points in velocity space and N_p is the average number of particles per cell. [7] The DK simulation is parallelized using MPI, and its domain is split into four spatial regions: the channel, the plume adjacent to the channel, the upper plume, and the lower plume, as shown in Fig. 5.3. Each region utilizes an identical number of processors, and information is exchanged between spatially adjacent processors. The simulation results discussed in this work are computed using a total of 24 processors, and the wall time is approximately 3.4 days per 1 ms of computational time. The serial PIC simulation takes approximately 14 hours to complete 1 ms of simulation time. Simulations are conducted using the University of Michigan's high

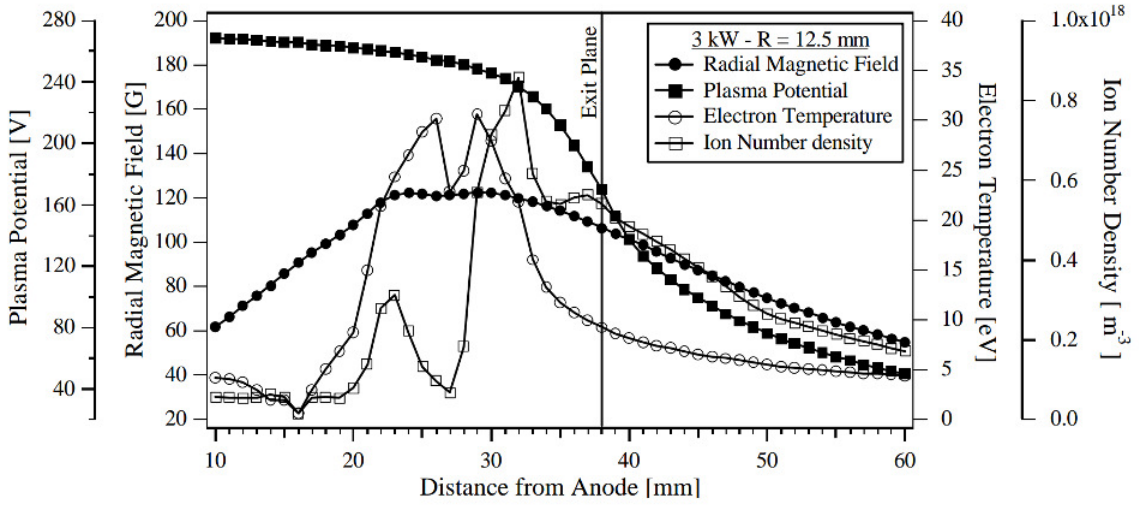

(a)

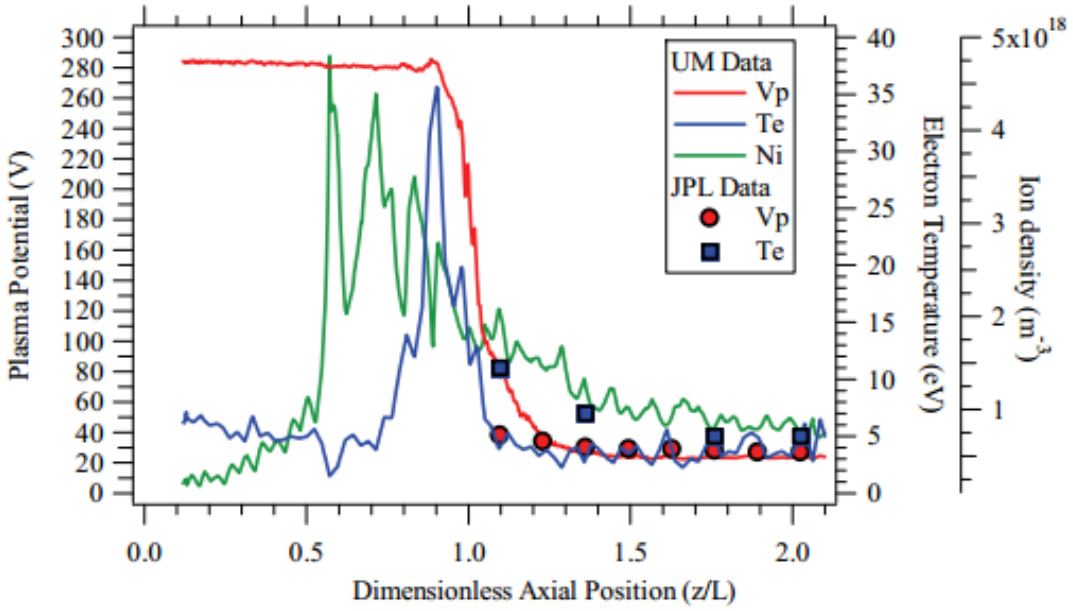

(b)

Figure 5.2: Experimentally measured plasma properties along the thruster channel centerline for the (a) 3 kW UM/AFRL P5 HET and (b) the 6 kW H6 HET. The plasma potential, electron temperature, and ion density are shown for each thruster configuration. Image (a) is reproduced from Reference [92] and Image (b) is reproduced from Reference [58].

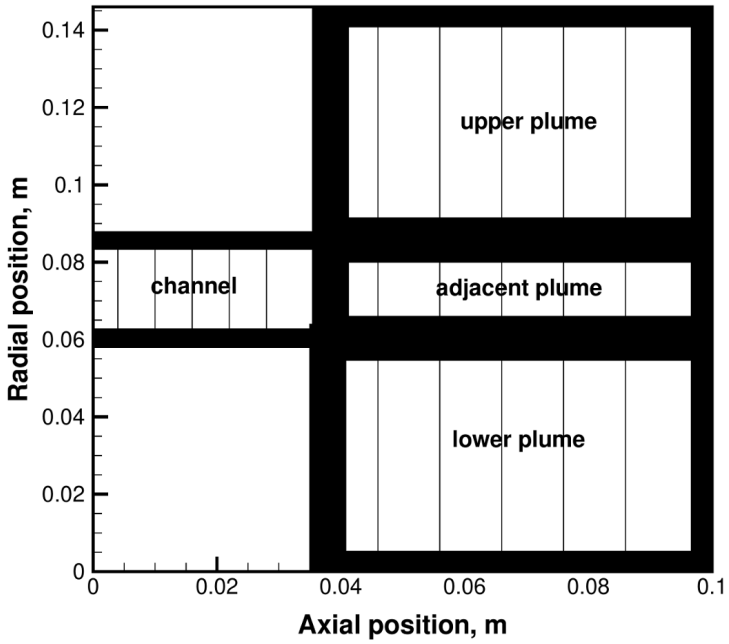

Figure 5.3: MPI processor setup for the hybrid-DK simulation. In this particular case, six processors are used in each group, and there are a total of four processor groups.

performance computing cluster.

A computational cost analysis can be conducted for the DK and PIC algorithms used in this work, providing an estimate of the CPU cost requirements for the two different methods. For the present DK simulation running on 24 processors, a global time step completes in approximately 2.16 s, as calculated in the data output files. The electron algorithm takes up approximately 0.4% of the total global time step, the neutral algorithm takes up approximately 26% of the time (verified in a neutral-only simulation), and the remainder of the time step is taken up by advection of the ion species, ionization, data storage, and MPI overhead. Since the physical cell count is identical for ions and neutral particles, the primary difference between the two lies in the distinct velocity bin counts for the two species. For neutral particles, there are 108 velocity bins in v_z and 240 velocity bins in v_r. For ions, there are 230 velocity bins in v_z and 140 velocity bins in v_r. Thus, ion velocity space contains approximately 24% more bins than neutral velocity space, implying that

the ion algorithm takes up approximately 32% of the total computational time step. Thus, approximately 43.6% of the global time step is devoted to MPI processes, data storage, etc. The multidimensional DK simulation always requires finite memory allocation, and it would be disingenuous to completely ignore the additional overhead cost. Therefore, it can be stated that the two-dimensional DK algorithm with neutral particles and ions, with physical and velocity space requirements similar to the case outlined here, uses between 1.2 s and 2.1 s of CPU time per time step, overall. In the simulation domain, there are 2515 physical cells, each containing 58,120 velocity bins. Thus, for the entire simulation, there are $2515 \times 58120 = 1.46 \times 10^8$ total grid points. This implies that the CPU cost per iteration per grid point is between 8.2×10^{-9} s and 1.4×10^{-8} s.

The hybrid-PIC simulation is entirely serial and thus does not devote overhead to parallelized processes, although there are data storage processes and memory allocation to consider. Assuming the simulation takes 14 hours to complete, a global time step completes in approximately 0.5 s. Using the same measure for the electron algorithm as in the DK case ($\Delta t_{electron} = 0.009$ s), the electron algorithm takes up approximately 1.8% of the global time step. For Case I, which is discussed in Section 5.3.1, a minimum of 600 macroparticles per cell are maintained in the thruster channel region, and a minimum of 140 macroparticles per cell are maintained in the plume adjacent to the channel. It is observed that these minimum values, overall, correspond reasonably well with the average number of particles per cell, particularly since the particle counts decrease below these values in the upper and lower portions of the plume. Thus, it can be assumed that there are approximately 370 particles per cell, on average. Assuming that ionization and computational overhead costs account for a maximum of 20% of the simulation time, the global PIC CPU cost per time step is between 0.39s and 0.49 s. Assuming there are a total of $370 \times 2515 = 9.3 \times 10^5$ macroparticles in the simulation domain, the CPU cost per macroparticle is between 4.2×10^{-7} s and 5.3×10^{-7} s. Therefore, the CPU cost per iteration per macroparticle per grid point is between 1.7×10^{-10} s and 2.1×10^{-10} s. This

implies that the computational cost of the multidimensional DK simulation is between 40 and 80 times higher than that of the multidimensional PIC simulation.

Simulation parameters of interest are displayed in Table 5.1. When possible, DK and PIC parameters are identical to ensure that the simulations are comparable. The Debye length in a HET is $\lambda_D \approx 1$ μm - 0.1 mm, and in this range, the quasineutral plasma assumption breaks down. The spatial resolution of the model is a fixed, uniform grid cell size of 2.0 mm $\times$ 2.0 mm, which is larger than the Debye length. Thus, Poisson's equation is ignored for both the DK and PIC cases, and quasineutrality is assumed everywhere in the domain. The time step, $\Delta t = 1.0 \times 10^{-8}$ s, is selected to satisfy the CFL condition for the DK simulation. An electron subcycling frequency divisor of 200 is utilized, corresponding to Koo and Boyd's previous work. [44] Minimum threshold values for the number density are required for the PIC simulation in case cells become devoid of macroparticles. A large number of macroparticles (counts are described in the case setups) are used to minimize the occurrence of this type of event. The minimum threshold density is not a requirement for the DK simulation, but the same condition is applied for consistency; the threshold values used correspond to those applied in Koo and Boyd's previous work. [44] The selected values should not affect the physical response, since they are below the minimum instantaneous, calculated density values.

For the PIC simulation, a fully-developed neutral flow consisting of approximately 1.8×10^5 macroparticles is introduced into the domain at the start of the simulation, and a total target number of 4×10^5 ions is set. Unless specified otherwise, three neutral macroparticles are injected into the simulation at the anode boundary at each time step, and the total neutral macroparticle count cannot exceed 1.5×10^6 at any point in time. Macroparticle weights are distributed to the nodes of the Cartesian grid using a combination of radial and axial shape factors that are described Section 3.5.2. The particle count in each cell varies over time. For reference, instantaneous snapshots of both ion and neutral particle counts are shown in Fig. 5.4. Generally, the plume contains fewer macroparticles than the channel,

Table 5.1: Hybrid-DK and PIC simulation parameters.

Parameter	**Value**
Channel length, mm	38
Channel diameter, mm	26
Axial domain length, mm	100
Radial (plume) domain height, mm	146
Cell size (physical space), mm	2.0 x 2.0
Number of cells	2515
Number of λ-lines	21
Global time step, s	1.0×10^{-8}
Electron time step, s	5.0×10^{-11}
Minimum plasma density, m^{-3}	5.0×10^{12}
Minimum neutral density, m^{-3}	5.0×10^{15}
Anode potential, V	275
Anode mass flow rate, mg/s	10.2

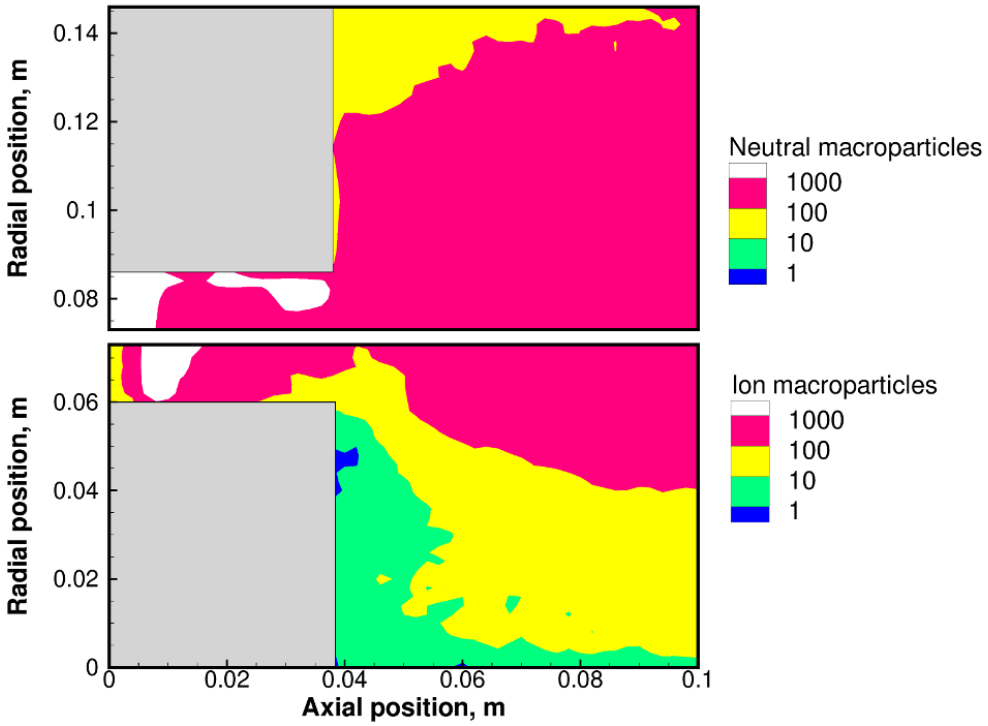

Figure 5.4: Sample instantaneous neutral and ion macroparticle counts per cell in the PIC simulation domain.

indicating that flow properties should exhibit the most numerical noise in the plume region. To obtain reasonable resolution with the PIC simulation using the same time step as the DK simulation, it is necessary to utilize a relatively large number of macroparticles. The parameters for DK velocity space are shown in Table 5.2. Note that the discretization for neutral velocity space matches the coarse discretization discussed in Chapter IV.

In both the DK and PIC simulations, the anode reservoir and channel walls are assumed to be at a temperature of 750 K, which falls within the range of experimentally measured temperatures in the acceleration channel and below the maximum design constraint temperature of approximately 970 K for BN-SiO_2 in efficient HET operation [93, 94]. It is presumed that the anode will reach thermal equilibrium at this temperature. At the anode side of the thruster, incoming neutral atoms are emitted from a slit opening with a height of 2.0 mm, centered at ($z = 0$ m, $r = 0.073$ m). The inlet neutral flow is assumed to be in the free molecular regime, as the Knudsen number is greater than 7 for a neutral density

Table 5.2: DK velocity space parameters.

Parameter	Value
$v_{n,z}$	$(-1.2, 1.5)$ km/s
$\Delta v_{n,z}$	25 m/s
$v_{n,r}$	$(-1.2, 1.2)$ km/s
$\Delta v_{n,r}$	10 m/s
$v_{i,z}$	$(-16, 30)$ km/s
$\Delta v_{i,z}$	200 m/s
$v_{i,r}$	$(-14, 14)$ km/s
$\Delta v_{i,r}$	200 m/s

of 10^{20} m^{-3}, assuming an injector slit height of 2 mm. The velocity of injected particles is described by a Maxwellian VDF biased with axial velocity. Note that for the DK and PIC simulations, wall collisions are not allowed at the inlet opening. If back-streaming particles travel into the inlet, they simply leave the simulation domain. While this may result in a slight decrease of mass overall, the inlet opening is quite small, and the resultant decrease in mass is negligible. For both cases, neutral particles fill up the domain via the anode injector prior to any plasma generation.

5.2.1 Electron Model Boundary Conditions

The near-anode region of a HET typically displays a relatively low electron temperature (3-6 eV), little or no electric field, a small applied magnetic field, and relatively high diffusion of electrons. Neutral particles from the anode injector move downstream toward the ionization region, and back-streaming ions travel toward the anode. [73] However, the quasi-one-dimensional electron model does not correctly recover the diffusion region. The model actively solves the electron fluid equations starting at the virtual anode location, which is slightly offset from the anode face in Fig. 5.5, and information upstream of the virtual anode is extrapolated.

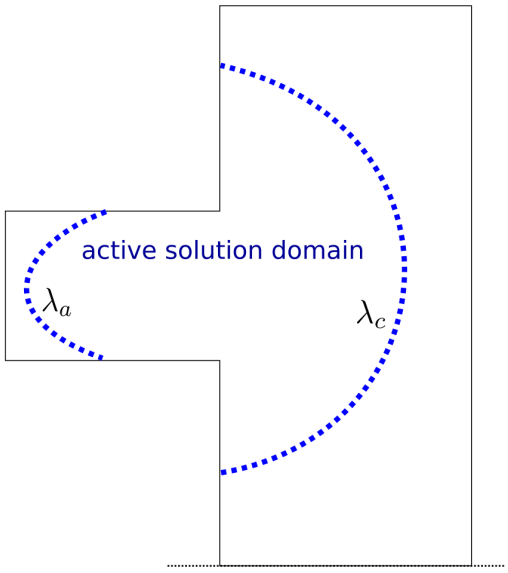

Figure 5.5: Representation of the active electron fluid solution domain, not drawn to scale.

Near the anode, the current contribution from electrons should be high compared to that from ions, since any positively-moving ions are slow, and back-streaming ions contribute negatively to the total current. The electron current density in Eq. (2.21) can be expressed as a function of λ as follows:

$$j_{e,\perp} = en_e\mu r B\left(-\frac{\partial\phi^*}{\partial\lambda} - \left[\ln\left(\frac{n_e}{n_e^*}\right) - 1\right]\frac{k_b}{e}\frac{\partial T_e}{\partial\lambda}\right). \tag{5.1}$$

If the electron temperature does not vary much in the near-anode region, and the potential is nearly constant, the value calculated via Eq. (5.1) is small, implying that the non-zero contribution from electron pressure in this region may not be accurately calculated via the quasi-one-dimensional approach. Of course, the electron current density can be increased in the near-anode region via a large cross-field electron mobility term, but it is not the purpose of the present work to optimize the electron transport quantities. As such, simulation boundary conditions that provide solution stability and reasonable plasma evolution are sought, and a configuration that allows for comparison between hybrid-PIC and hybrid-DK simulations for both high frequency and low frequency oscillatory responses is obtained.

It is worth pointing out that hybrid-PIC simulations may experience solution instabilities due to the treatment of the anode boundary condition, since the physics in the vicinity of the anode are not properly resolved. [78] One approach to limit ionization and temperature fluctuations in the vicinity of the anode is to apply Dirichlet boundary conditions for both the potential and electron temperature at the virtual anode and cathode locations. [44, 45] Often, threshold limits are applied to the plasma potential to ensure that it will not fluctuate beyond the discharge voltage limits at the anode and cathode anywhere in the domain, and ionization may not be permitted upstream of the anode λ-line. In this work, the hybrid-DK simulation is found to be sensitive to the applied boundary conditions and threshold limits, particularly if they are too restrictive, since the plasma properties are well resolved. If the plasma is constrained due to artificial plasma limiters, it will evolve to a non-physical solution.

For example, if the potential is constrained to values between the anode and cathode voltage limits, and a Dirichlet electron temperature boundary condition is applied at the anode, the solution may become over-constrained, and a small, non-realistic fluctuation in plasma properties may exist in the vicinity of the anode λ-line. [95] On the other hand, if a pure Neumann (zero-slope) boundary condition is applied for the electron temperature at the anode λ-line, the ionization rate may grow in the vicinity of the anode injector, causing the electron temperature to increase, resulting in more ionization. Without a properly modeled anode sheath or an energy loss mechanism to decrease the growth of the electron temperature, the growth will eventually result in simulation divergence.

It is found that a more realistic solution can be obtained, without any threshold values required for the plasma potential, when a Neumann (finite-slope) boundary condition is applied to the electron temperature at the anode λ-line. In the simulation's present configuration, the potential is fixed at the virtual anode and cathode locations and assumed to be constant upstream of the virtual anode and downstream of the virtual cathode. The electron temperature is fixed to a constant value at the virtual cathode, and a Neumann boundary

condition is applied at the virtual anode. Upstream of the anode and downstream of the cathode, the electron temperature decays to maintain a smooth solution and to limit ionization in the vicinity of the anode injector. However, ionization is allowed everywhere in the domain, whereas in Koo's original hybrid-PIC simulation, the ionization algorithm was typically disabled upstream of the anode λ-line. [48]

5.3 Results

To determine the level of agreement between the DK and PIC simulations, cases with both high and low frequency oscillatory responses are obtained by varying the input parameters. These sets of parameters (two cases) are chosen so that the DK and PIC simulations can be benchmarked, and both time-independent and transient plasma behavior can be analyzed. Although plasma processes are of interest, the primary purpose is to benchmark the hybrid-DK and hybrid-PIC simulations and demonstrate that the DK algorithm reduces the level of statistical noise in the simulation results while obtaining similar time-averaged results. For this reason, the contribution of variable anomalous electron transport is largely ignored, as it does not directly impact the kinetic algorithms that are under comparison.

Differences between input parameters of interest for the two cases are shown in Table 5.3. Within this section, Case I is referred to as the *high frequency* simulation, as it exhibits a dominant frequency response around 100 kHz, compared to the low frequency of approximately 7 kHz exhibited in Case II. The input parameters are selected so that different behavior will be exhibited for the two cases. In Case I, the domain is large and the Bohm mobility coefficient is constant throughout, so the electric potential falls gradually and spreads across most of the domain. The electron temperature is fixed at the anode face in this case and changes gradually with the electric potential, so there is no impetus for periodic ionization bursts and neutral replenishment which accompany a low-frequency mode. The solution domain for Case II is smaller than that for Case I to ensure that the axial

Table 5.3: Simulation benchmarking input parameters.

	Case I	**Case II**
Anode λ-line location	$z \approx 1.3$ cm	$z \approx 1.3$ cm
Cathode λ-line location	$z \approx 8.6$ cm	$z \approx 5.0$ cm
T_e at z = 0	1.33 eV	Neumann
T_e at cathode λ-line	0.67 eV	3.35 eV
α_w	0.4	0.2
α_b	0.006	0.0

electric field will be large, and Bohm mobility is not considered. A finite slope condition is applied to the electron temperature at the anode face in Case II, and the electron temperature is higher inside the channel, promoting cyclical ionization bursts, neutral depletion, and low frequency oscillations.

5.3.1 Case I: High Frequency Simulation

Since this case exhibits a high frequency response, it is used to examine the effect of numerical noise on the discharge current. Additionally, this case is utilized to determine the impact that a variable collision multiplier, discussed in Section 3.5.2, has on hybrid-PIC results.

5.3.1.1 Case I Simulation Setup

In Case I, the electron temperature between $z = 0$ and the anode λ-line is linearly interpolated. It is fixed to 1.33 eV at $z = 0$, and a Neumann boundary condition is applied to the electron temperature at the anode λ-line (located at approximately 1.3 cm). The maximum electron temperature at the anode λ-line is limited ($\left(\epsilon_{\lambda_{anode}+1}\right)_{max} = 10$ eV), which is necessary so that neither simulation will diverge to high, non-physical electron temperatures. Electron-wall collisions and Bohm mobility ($\alpha_b = 0.006$) are considered throughout the

Table 5.4: Sub-cases to examine the effects of the collision multiplier and macroparticle count on hybrid-PIC simulation results for Case I.

Sub-case	**Injected macroparticles/Δt**	$\gamma_{\mathbf{min}}$	$\gamma_{\mathbf{max}}$
Ia	3	4	$\frac{\sqrt{(4P_C)}}{P_C}$
Ib	200	4	$\frac{\sqrt{(4P_C)}}{P_C}$
Ic	200	1	1

domain. Since α_b is fixed, the Bohm mobility acts to increase the overall electron current everywhere in the domain.

5.3.1.2 Collision multiplier effects

As discussed in Section 3.5.2, a multiplier, γ, is implemented in the PIC collision algorithm so that a sufficient number of ion macroparticles are generated to achieve acceptable particle statistics. It follows that, if it is possible to generate a sufficient number of ion macroparticles without a multiplier, then its presence should not be required. In this section, the effects of the collision multiplier, γ, are examined in conjunction with the injected neutral macroparticle count to determine their impact on the resultant discharge current. The sub-cases used for this effort are highlighted in Table 5.4. γ_{min} represents the minimum value of the collision multiplier. If the total number of ion macroparticles in the domain is below the ion target, the multiplier is increased to γ_{max}.

In Fig. 5.6, the effects of eliminating the multiplier for Case I are elucidated. Case Ia is the base case, for which 3 neutral macroparticles are injected into the domain at each time step ($3/\Delta t$), and the prescribed collision multiplier is $\gamma_{min} = 4$. When the injected neutral macroparticle count is increased to $200/\Delta t$ in Case Ib, the level of numerical noise in the current amplitude as a function of time decreases, as shown in Fig. 5.6a and further highlighted in Fig. 5.6b. The numerical noise appears to decrease slightly between Cases Ib and Ic when the collision multiplier is removed altogether, as shown in Fig. 5.6a, but the effect of noise on the current is not notably different for either case in Fig. 5.6c. This

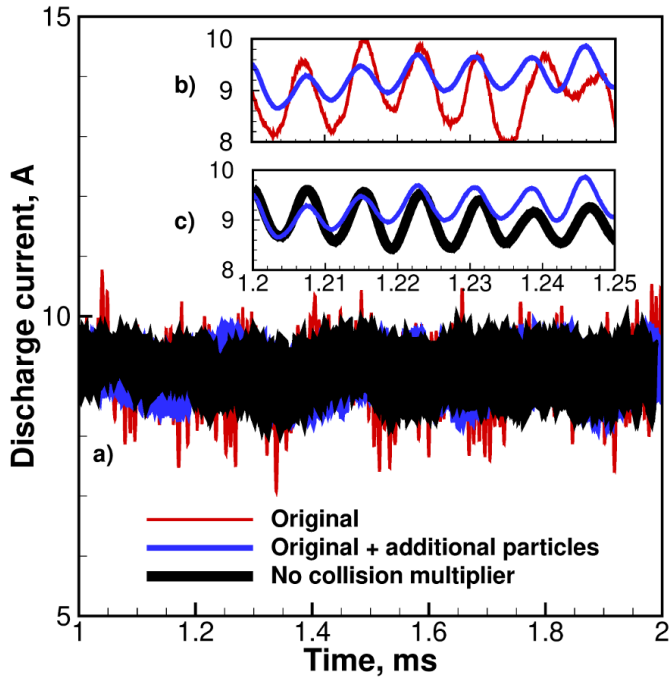

Figure 5.6: Case I discharge current vs time for three different sub-cases to view the effect of the variable collision multiplier on simulation results. In (a), the overall response for all three sub-cases is shown. In (b), highlighted current oscillations for the original case Ia (red) are compared to Case Ib (blue). In (c), Case Ib (blue) is compared to Case Ic (black).

indicates that the number of macroparticles in sub-cases Ib and Ic is statistically significant, and the collision multiplier does not have much of an effect on the response; therefore, it is not required. For reference, sub-case Ic contains at least 500 neutral macroparticles per cell inside the channel and 100 neutral macroparticles per cell in the plume region directly adjacent to the channel. Except for near the channel walls, a minimum of 100 ion macroparticles per cell is maintained inside the channel, and at least 40 ion macroparticles per cell are found in the plume adjacent to the channel. The macroparticle count decreases in the upper and lower portions of the plume, and the implications of this are discussed in Section 5.3.1.3.

According to the results for this case study, it is more accurate to include a sufficient number of neutral macroparticles in the domain for ionization collisions than it is to use a variable collision multiplier. However, if there are large scale fluctuations in the plasma response, a collision multiplier may be required in locations where neutral macroparticles are

largely depleted due to ionization and cannot be replenished in a timely manner. For such a case, γ should be allowed to vary as a function of macroparticle count locally rather than globally, and used with caution. A variable collision multiplier adds a factor of uncertainty and source of noise to the simulation beyond the statistical nature of the PIC algorithm itself and deserves further attention. However, additional efforts related to this are beyond the scope of this study.

5.3.1.3 Case I Results

Since Case Ic from Section 5.3.1.2 does not contain stochastic noise due to usage of a variable collision multiplier, it is used as the comparative PIC technique for the Case I benchmarking effort. The discharge current profiles shown in Fig. 5.7 have slightly different mean values of approximately 8.6 A and 9.0 A for DK and PIC results, respectively. The PIC response in Fig. 5.7b shows some deviation in the current amplitude, while the DK results oscillate coherently about the mean value. The PIC results have a primary frequency around 125 kHz, and the DK results exhibit two distinct oscillatory frequencies at 97 kHz and 194 kHz.

The power spectral density (PSD) values for the calculated DK and PIC discharge currents are compared in Fig. 5.8. If $X(f)$ is the one-dimensional discrete Fourier transform of a time-series $x(t)$ with length N, then the spectral estimate of the signal, $S_N(f)$, is: [31]

$$PSD(f) = S_N(f) = \frac{1}{N} X^*(f) X(f) \tag{5.2}$$

Without proper scaling on Eq. (5.2), the units are listed as Arbitrary units/Hz. At intermediate frequencies ($10^5 - 10^6$ Hz), the DK results exhibit sharp, relatively narrow peaks in the data. High frequency data is somewhat scattered. The PIC results exhibit a scattered signal for nearly all of frequency space, although the data is less scattered at the location of the dominant frequency mode (125 kHz). For DK results beyond the primary frequency values

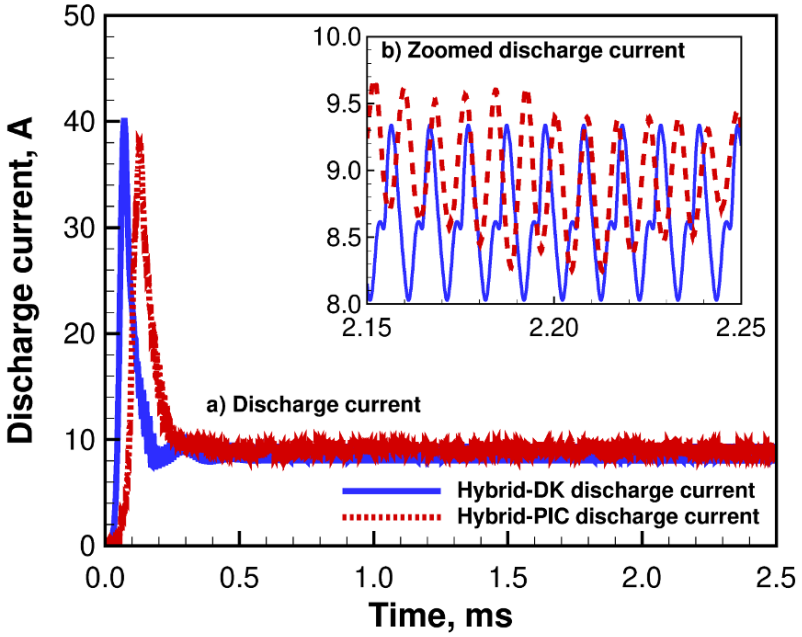

Figure 5.7: (a) Case I discharge current over 2.5 ms. (b) Zoomed discharge current over 0.1 ms.

of 97 kHz and 194 kHz, the distinct frequency modes with a lower PSD may be caused by numerical oscillations associated with DK-electron algorithm coupling as well as the finite discretization of both the physical and velocity grids. For example, it is known that undamped, high frequency numerical errors may occur due to the coupling of the electron pressure and ion pressure terms in a quasineutral plasma using the drift-diffusion approximation for the electron flux. [47] Since the electron algorithm is the same for the hybrid-DK and hybrid-PIC approaches, the expectation is that such frequencies would also be present in the PIC data. However, it appears that statistical noise tends to damp out the higher frequency modes in the PIC data. In some ways, this is advantageous; distinct modes due to grid-based noise are not necessarily present in the hybrid-PIC results. However, the level of statistical noise is quite high at at both low and high frequency levels. The DK method, on the other hand, does not damp out numerical noise due to numerical discretization or algorithm coupling, but it is capable of capturing high frequency modes that are attributed

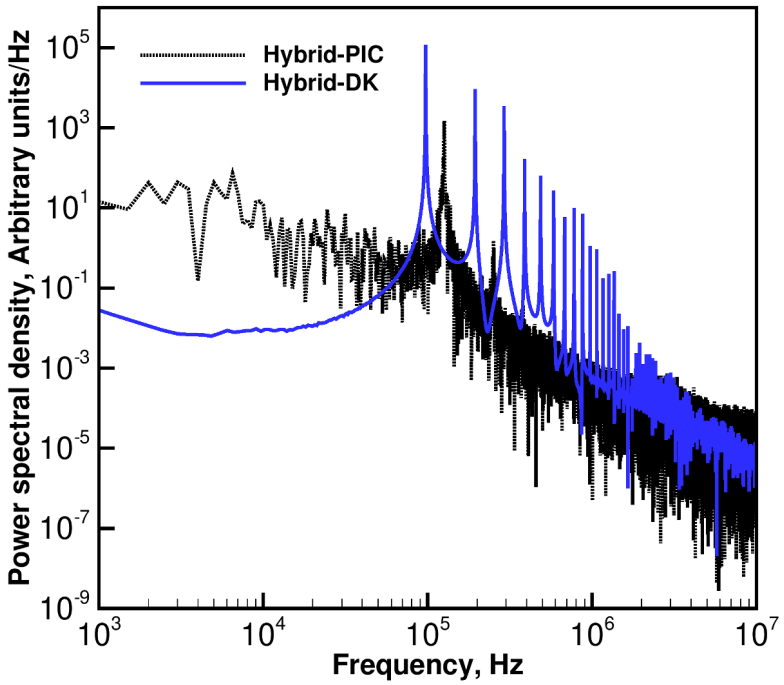

Figure 5.8: Case I discharge current oscillation spectra for hybrid-DK and hybrid-PIC data.

to physical processes.

The primary hybrid-DK (97 kHz and 194 kHz) and hybrid-PIC (125 kHz) frequencies are associated with the evolution of the thermalized potential at the anode and cathode λ-lines, which is shown in Fig. 5.9. The frequency response of the varying potential matches the frequency of the discharge current response. For both the DK and PIC cases, the thermalized potential at the anode λ-line in Fig. 5.9 oscillates, but its minimum value becomes limited at approximately 198 V. The limited potential corresponds with the saturation of the electron temperature ($\epsilon_{max} = 10.0$ eV). This limiting behavior is due to the numerical constraint in the electron temperature at the anode λ-line. However, the interesting point is that the DK and PIC solutions respond differently to the constraint. The thermalized potential, ϕ^*, is a function of the two-dimensional potential, the plasma density, and the electron temperature. Since both the two-dimensional potential and electron temperature are fixed at the cathode λ-line, ϕ^* at the cathode can vary only with plasma density. For the

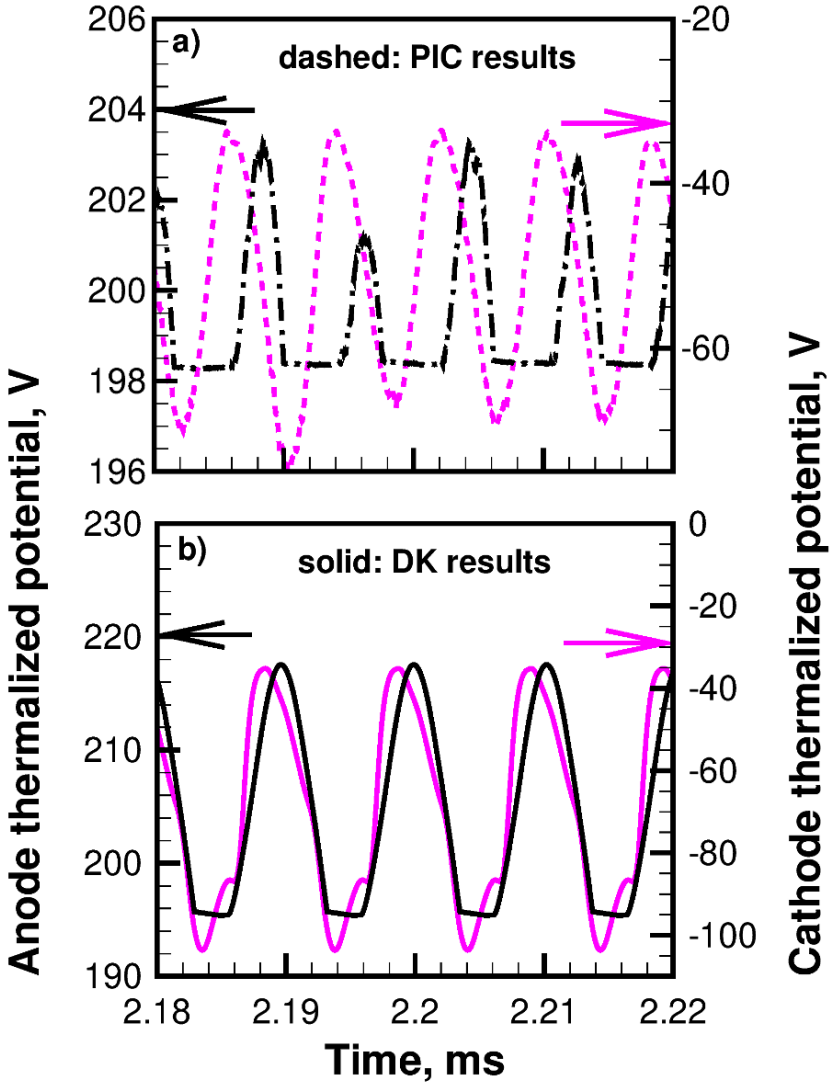

Figure 5.9: (a) Hybrid-PIC and (b) Hybrid-DK thermalized potential values at the anode and cathode λ-lines. Note that numerical scales for the potential values are distinct.

DK solution in Fig. 5.9b, the thermalized potential at the cathode λ-line undergoes a high-frequency oscillation to accommodate a sudden change in the plasma density at the cathode. This change in density at the cathode reflects the travel of ions from a small, secondary ionization zone created near the anode λ-line to accommodate local electron temperature saturation. Although the oscillatory behavior is generated via a numerical constraint, the high frequency behavior could be described by the ion transit time-oscillation. [96, 97] The oscillation, typically in the 100-500 kHz range, has a period on the order of the transit time of ions passing through the acceleration region and is associated with an oscillating electric field and the formation of a tail in the ion energy distribution function. The PIC solution in Fig. 5.9a does not exhibit the same behavior as the DK response. There is no distinct change in the cathode potential that corresponds to a change in behavior at the anode. The difference between the DK and PIC solutions may be attributed to the inability of the PIC simulation to capture rapid, localized changes in the plasma density, due to its stochastic nature.

The 194 kHz mode in the DK results is better understood through examination of the instantaneous plasma response. As mentioned previously, the mode is associated with a secondary ionization zone near the anode λ-line. This zone can be seen clearly in Fig. 5.10a, which shows the varying ionization rate at the channel centerline over the course of a single (97 kHz) oscillation. The secondary ionization zone forms in the vicinity of $z = 0.2$ m. The PIC response in Fig. 5.10b includes an an increase in the ionization rate at the same location, but there is no secondary zone associated with a high frequency mode. Both data sets have a sampling interval of 0.1 τ, where τ is the period of the oscillation. The difference between the DK and PIC responses is further demonstrated in contours showing the evolution of the axial electric field and electron temperature in Figs. 5.11 and 5.12, respectively. At approximately 0.2 τ in Fig. 5.11a, the DK electric field in the vicinity of the anode ($z < 0.02$ m) decreases abruptly. This is because the thermalized potential at this time instance becomes limited, thereby limiting the local potential and decreasing the local

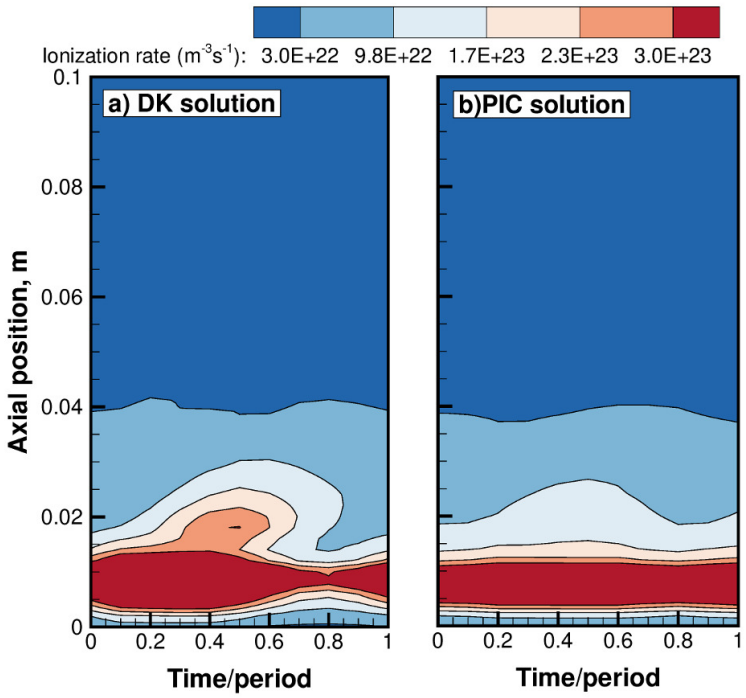

Figure 5.10: (a) Hybrid-DK and (b) hybrid-PIC ionization rate along the thruster channel centerline over the course of a single (97 kHz) oscillation.

electric field. When the electric field decreases locally, slow ions contribute to an increase in the ionization rate, and the electron temperature in Fig. 5.12a must accommodate to local changes. The PIC response in the electric field, shown in Fig. 5.11b, is more subtle, and the electron temperature in Fig. 5.12b accommodates slightly.

Time-averaged hybrid-DK and hybrid-PIC plasma properties are shown in Fig. 5.13. A sampling interval of 1 μs is used for data collection. The PIC neutral and ion density profiles at the thruster channel centerline in Fig. 5.13a show reasonable agreement with corresponding DK properties. Ionization rates in Fig. 5.13b are nearly identical. The average electron temperature and potential profiles for the two simulations in Fig. 5.13c also exhibit similar trends, although the DK electron temperature is slightly higher near the channel exit and in the plume region. There is a small discrepancy in the average axial ion velocity, which is shown at two locations (channel centerline, centerline-5.0 mm) in Fig. 5.13d, and this difference corresponds with the slight difference in the potential profiles in Fig. 5.13c.

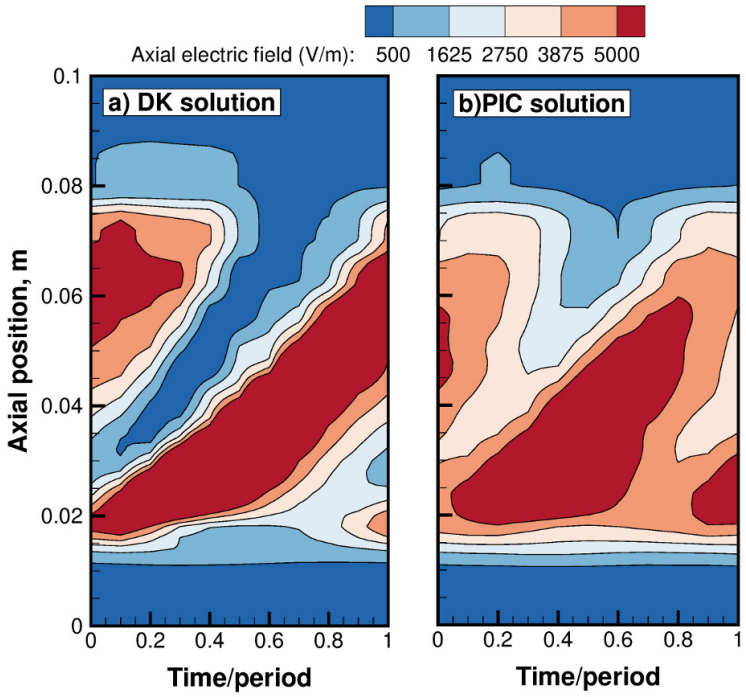

Figure 5.11: (a) Hybrid-DK and (b) hybrid-PIC axial electric field along the thruster channel centerline over the course of a single (97 kHz) oscillation.

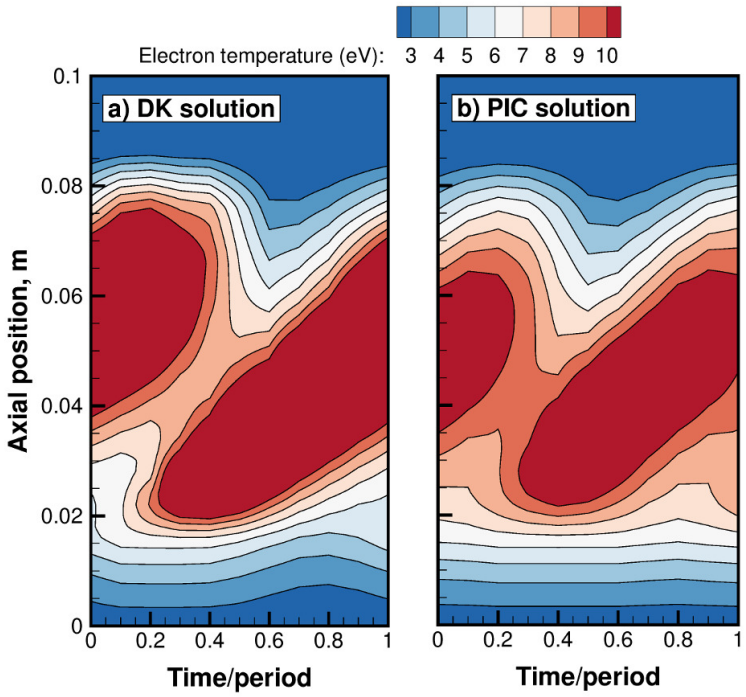

Figure 5.12: (a) Hybrid-DK and (b) hybrid-PIC electron temperature along the thruster channel centerline over the course of a single (97 kHz) oscillation.

Some of the differences in the DK and PIC plasma response, particularly in the downstream properties, may be attributed to the lack of resolution of PIC ions in the plume, adjacent to the thruster pole pieces. Adjacent to the pole pieces, the potential often falls somewhat below 0 V. This is due to the dependence of the two-dimensional potential on the electron temperature and plasma density at this location, i.e. $\phi(\lambda, r) = f(T_e(\lambda), n_e(\lambda, r))$. The plasma density near the pole pieces is typically low compared to the plasma density along the centerline of the thruster channel, i.e. in the plume adjacent to the channel. However, the electron temperature near a pole piece decreases and increases in accordance with the electron temperature at the thruster channel centerline since it is constant along a λ-streamline. If the electron temperature is small, the two-dimensional potential in the vicinity of the pole piece may become negative if the plasma density is also low, resulting in a negative electric field that causes ions to stream toward the pole piece. Although the evolution of the electric field at this location is not markedly different for DK and PIC responses, the PIC simulation often reaches its minimum threshold ion density near the pole piece and cannot sufficiently resolve the effects of the electric field at that location. This is demonstrated by the low PIC ion density in Fig. 5.14b compared to the DK ion density in Fig. 5.14a. The low ion density adjacent to the pole piece is associated with a lack of ion macroparticles. In response to the axially-moving ions traveling toward the pole piece in the DK case, the losses increase, and the electron temperature also increases. Since the electron temperature is constant along magnetic field stream lines, the changes at the pole piece are coupled to the changes along the centerline of the thruster outside the channel exit, and this contributes to the higher DK electron temperature along the centerline in Fig. 5.13c.

Case I does not necessarily emulate the behavior of a typical HET. However, this case benchmarks a high-frequency hybrid-DK simulation with a hybrid-PIC simulation and highlights the clarity of the output in the DK results compared to the PIC results, particu-

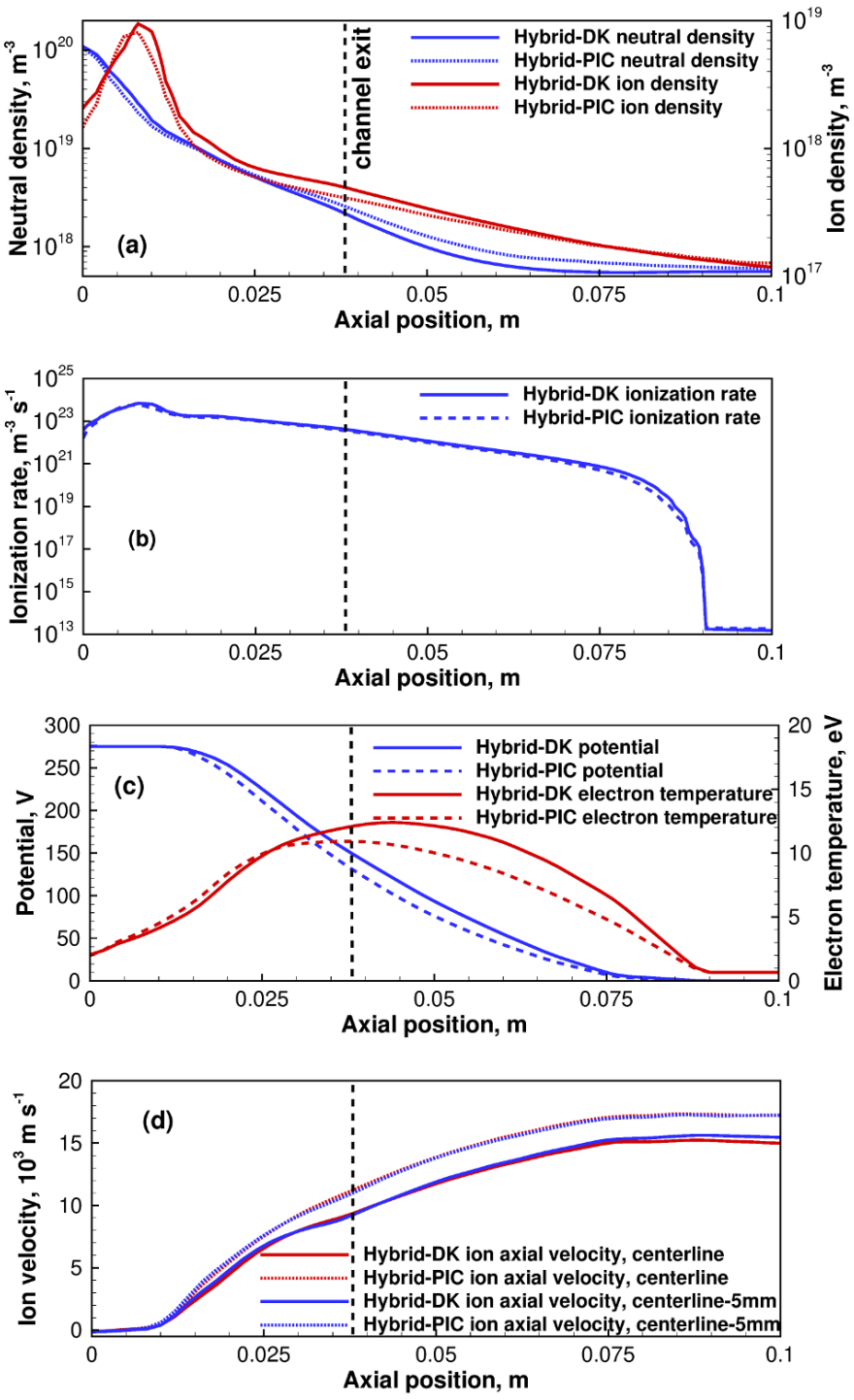

Figure 5.13: Case I DK and PIC average properties along the thruster channel centerline at t = 2.5 ms. Shown are (a) neutral and ion densities, (b) ionization rates, (c) potential and electron temperature profiles, and (d) ion axial velocities along the thruster channel centerline and 5 mm below the centerline.

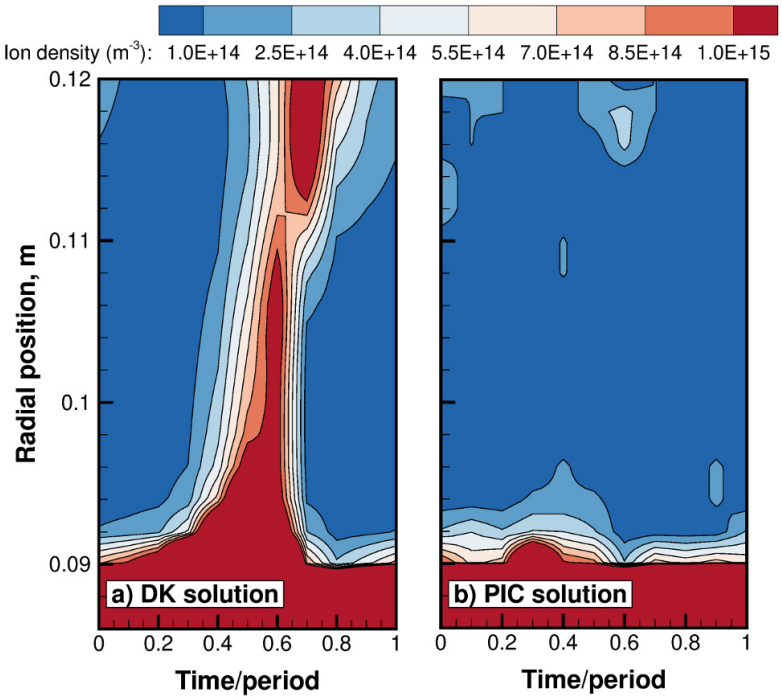

Figure 5.14: (a) Hybrid-DK and (b) hybrid-PIC ion density along the upper pole piece over the course of a single (97 kHz) oscillation.

larly evident in the discharge current, in which coherent oscillations are clearly seen in the DK response due to the lack of stochastic noise. With a large macroparticle count, the numerical noise in the PIC algorithm is greatly reduced, but it is not eliminated. Furthermore, this case highlights the sensitivity of the DK algorithm compared to the PIC algorithm, as evidenced by a second high frequency mode, and it also highlights the importance of sufficient resolution of plasma properties not only in the primary location for the plasma discharge but also in the plume of the thruster, adjacent to the pole pieces.

5.3.2 Case II: Low Frequency Simulation (<10 kHz)

HETs typically exhibit repetitive, low frequency oscillations known as *breathing mode* oscillations. Electron dynamics are known to play an important role in this mode. Hara *et al.* examined the role of the electron temperature in this process, [29] and Dale and Jorns experimentally observed the relationship between anomalous electron transport and the

low frequency mode and determined that the anomalous collision frequency profile varies significantly over a breathing cycle. [37] During a breathing mode cycle, neutral particles are depleted as ionization occurs. The current remains low until there is a sufficient ion population inside the channel, and then ions are accelerated out of the thruster, increasing the ion current. As ions leave the channel, the electron temperature decreases in the thruster, neutral particles are replenished by gas injection, and the cycle repeats.

5.3.2.1 Case II Simulation Setup

For Case II, numerical parameters are selected to generate a breathing mode oscillation. In theory, a variable electron transport model may be useful to this end. However, to simplify this case, Bohm transport is neglected, and only electron-wall collisions are considered. To ensure that the potential drop does not spread too far downstream, the cathode is shifted closer to the channel exit compared to Case I, as described in Table 5.3.

A simple anode sheath model is considered, similar to that used by Fife, and the Boltzmann relation is applied for the calculation of the electron density inside the sheath. [42] Using classical electrode theory in the limit of a collisionless, thin sheath, the total current can be written as a function of the sheath potential:

$$I_T = Aen_e \left[\exp\left(\frac{e\phi_a}{k_b T_e}\right) \sqrt{\frac{k_b T_e}{2\pi m_e}} - \exp\left(-\frac{1}{2}\right) \sqrt{\frac{k_b T_e}{m_i}} \right], \tag{5.3}$$

where A is the anode area, and ϕ_a is the potential drop at the anode. This expression assumes that the ion Bohm condition is met at the sheath edge. Rearranging the expression in Eq. (5.3), the sheath potential drop at the anode can be written as:

$$\phi_a = \frac{-k_b T_e}{e} \ln \left[\left(\frac{I_T}{Aen_e \sqrt{\frac{k_b T_e}{2\pi m_e}}} \right) + \exp\left(-\frac{1}{2}\right) \sqrt{\frac{2\pi m_e}{m_i}} \right]. \tag{5.4}$$

It is further assumed that the sheath is one-dimensional. Sufficient oscillatory behavior is

achieved when the electron temperature upstream of the anode λ-line corresponds to the relationship in Eq. (5.5):

$$T_e(\lambda) = T_e(\lambda_a)\exp(-0.1(\lambda_a - \lambda)). \tag{5.5}$$

This relationship ensures that the temperature will decay slightly upstream of the anode λ-line. This condition promotes variation in the electron temperature over time and in space for this particular thruster setup, promoting cyclical ionization sufficient for benchmarking.

It is likely that the anode sheath is important to limit the electron current in Case II. It is observed that the hybrid-PIC simulation becomes devoid of neutral macroparticles inside the channel at certain instances in time without applying such an anode sheath model, rendering the PIC results non-physical. Since the simplified anode sheath model allows for back-streaming ions and limits the ionization rate in the near-anode region, it is implemented in the boundary cells at the left hand side of the domain in Case II.

Additionally, the electron-wall collision frequency is lowered from $\alpha_w = 0.4$ to $\alpha_w = 0.2$, and although not shown here, this promotes greater variation in the discharge current amplitude, indicating that the balance between the electron collision frequency and inelastic energy losses is important. Note that hybrid-PIC results in this section use a variable collision multiplier which is necessary to ensure that, with the cyclical creation and depletion of ion macroparticles, there are always a sufficient number of macroparticles in the domain.

5.3.2.2 Case II Results

In Fig. 5.15a, two oscillations are highlighted for the hybrid-DK and hybrid-PIC discharge current responses. The time instances are shifted between the hybrid-PIC and hybrid-DK results so that dynamic oscillations are comparable. A Fourier analysis of the total data reveals a low frequency of 6.4 kHz in the DK case, whereas the PIC data exhibits a low

frequency oscillation around 7.0 kHz. The mean DK current for the data set is 6.3 A, while the PIC current is slightly higher at 6.8 A. The ion and electron contributions to the current are compared in Fig. 5.15b over three oscillatory periods. There is no significant difference between the DK and PIC data. The peaks and troughs of the DK current are slightly more pronounced than in the PIC results, and the difference in the average current indicates that the troughs in the DK current are consistently of lower amplitude than the troughs in the PIC current. This may be attributed to the fact that the neutral macroparticle count in the channel is relatively low following an increase in ion current, since neutral particles have been largely ionized. This, coupled with the usage of a variable collision multiplier, may artificially increase the ion current when it should be low.

Time-averaged DK and PIC plasma properties are shown in Fig. 5.16 with a sampling interval of 1 μs. The DK and PIC densities in Fig. 5.16a and electron properties in Fig. 5.16b are similar, overall. For the DK results, it appears that the location of the anode and cathode λ-lines, the extrapolation of plasma properties outside of the active solution domain, and possibly behavior near the pole pieces slightly affect the evolution of plasma properties on the channel centerline, as evidenced by the difference in shape of the average electron temperature profile between DK and PIC results in Fig. 5.16b. Inside the channel, the PIC ion density is lower than the corresponding DK ion density, even though the depletion rate of PIC neutral particles is slightly larger. The smaller PIC density is supported by the fact that the ionization rate near the anode face is higher for the PIC case (as reflected by the ion densities near the anode in Fig. 5.16a), meaning that there are more backstreaming ions to the anode sheath and thus, larger losses. Since the average potential drop in Fig. 5.16b is the same for the DK and PIC cases, the conclusion is that the PIC algorithm does not sufficiently resolve the ion density gradient in the vicinity of the anode sheath, likely due to the usage of a collision multiplier in conjunction with a finite number of macroparticles.

To highlight the deterministic nature of the DK algorithm, the evolution of DK and PIC

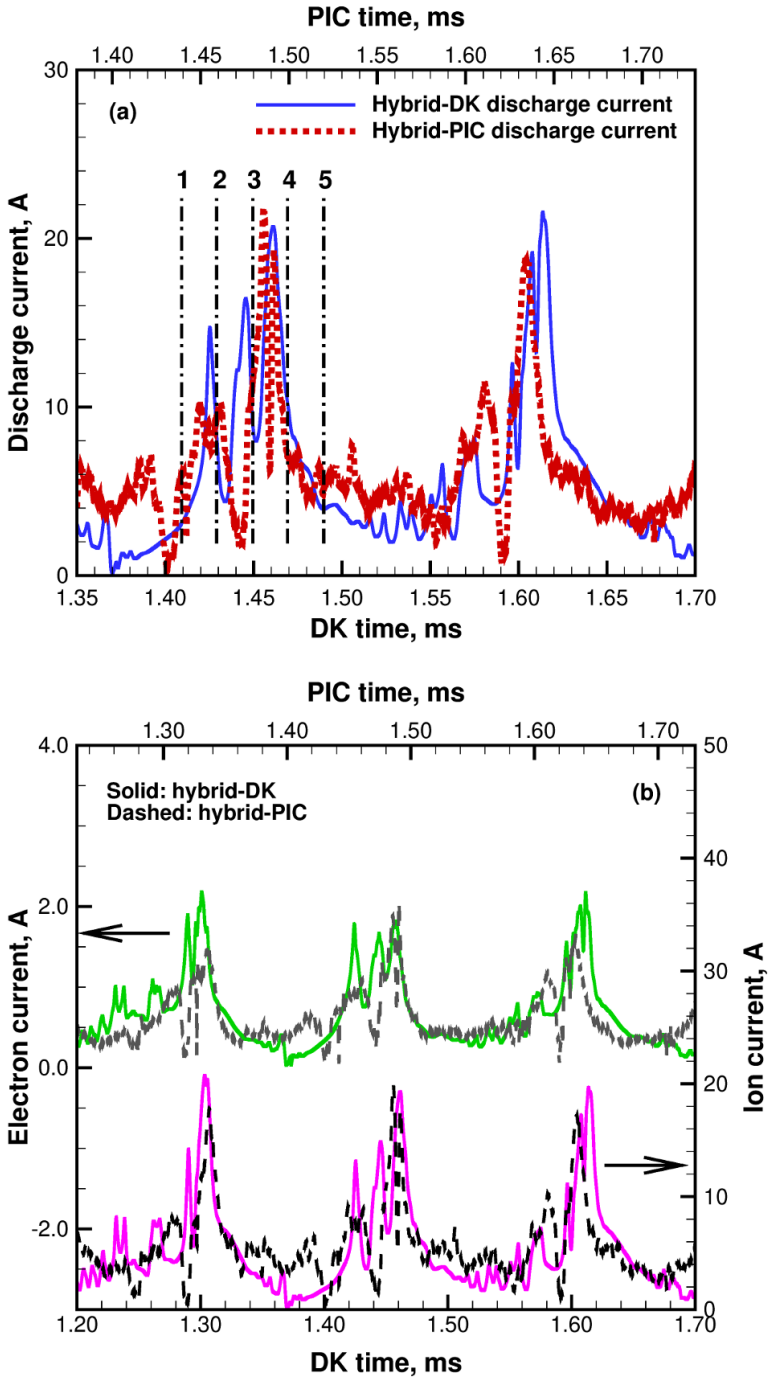

Figure 5.15: Case II discharge current vs time. In (a) two distinct discharge oscillations are shown, with time instances highlighted for one oscillation. In (b), the electron and ion current components are shown for three oscillations.

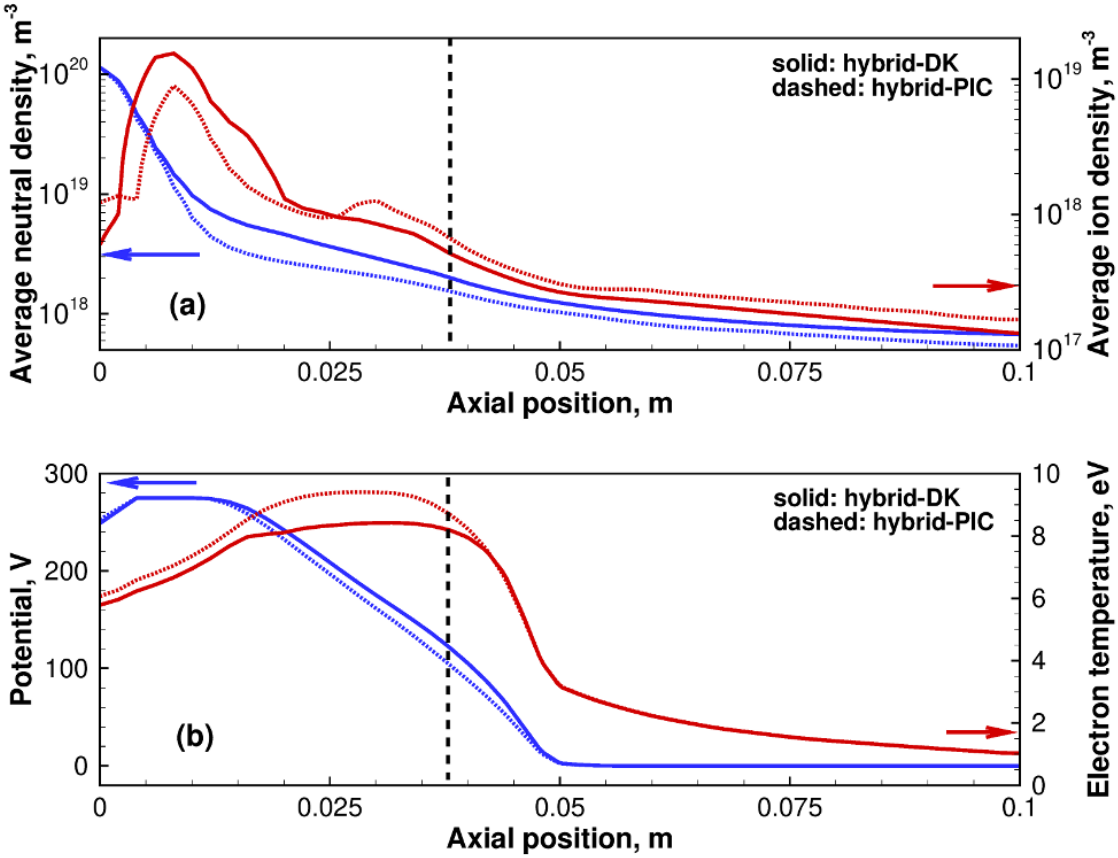

Figure 5.16: Case II DK and PIC time-averaged properties along the thruster channel centerline at 3.0 ms. Shown in (a) are neutral and ion densities and in (b) the potential and electron temperature.

neutral and plasma densities are compared over a single current oscillation. The time instances for comparison (points 1-5) are shown in Fig. 5.15a. In Fig. 5.17, neutral particles inside the channel are depleted at different rates for each time instance, with maximum particle depletion occurring at slightly different radial locations along the thruster channel centerline. The values of the neutral density should not be identical between the two cases since the current response is not exactly the same. Point 4 shows the lowest number of neutral particles for both the DK and PIC cases, and this corresponds well with an initial decay in the discharge current after the ionization burst occurs in Fig. 5.15a. The neutral particles are replenished inside the channel when the current is low. PIC results are reasonably free of noise inside the channel where the macroparticle count is high, but there is some numerical noise present in the plume, whereas corresponding DK results are free from numerical noise. The corresponding evolution of the ion density at the centerline is shown in Fig. 5.18. Numerical noise is especially evident in the PIC response in Fig. 5.18b. The PIC ion density trends exhibit smoothing inside the channel, which may be an artifact of excess numerical viscosity, a known issue for the PIC method. [98]

5.4 Summary and Conclusion

In this chapter, a two-dimensional, hybrid-direct kinetic (DK) simulation is benchmarked against a hybrid-particle-in-cell (PIC) simulation with an identical quasi-one-dimensional fluid electron algorithm. Both the discharge current profiles and the plasma properties match reasonably well between the two simulations, indicating that the benchmarking effort is successful, and that the performance of the two-dimensional DK algorithm is acceptable compared to the PIC algorithm.

To achieve simulation agreement, a boundary condition for the DK simulation that satisfies particle conservation at wall boundaries is developed in Chapter IV. The DK simulation is found to be more sensitive than the PIC simulation due to the anode boundary

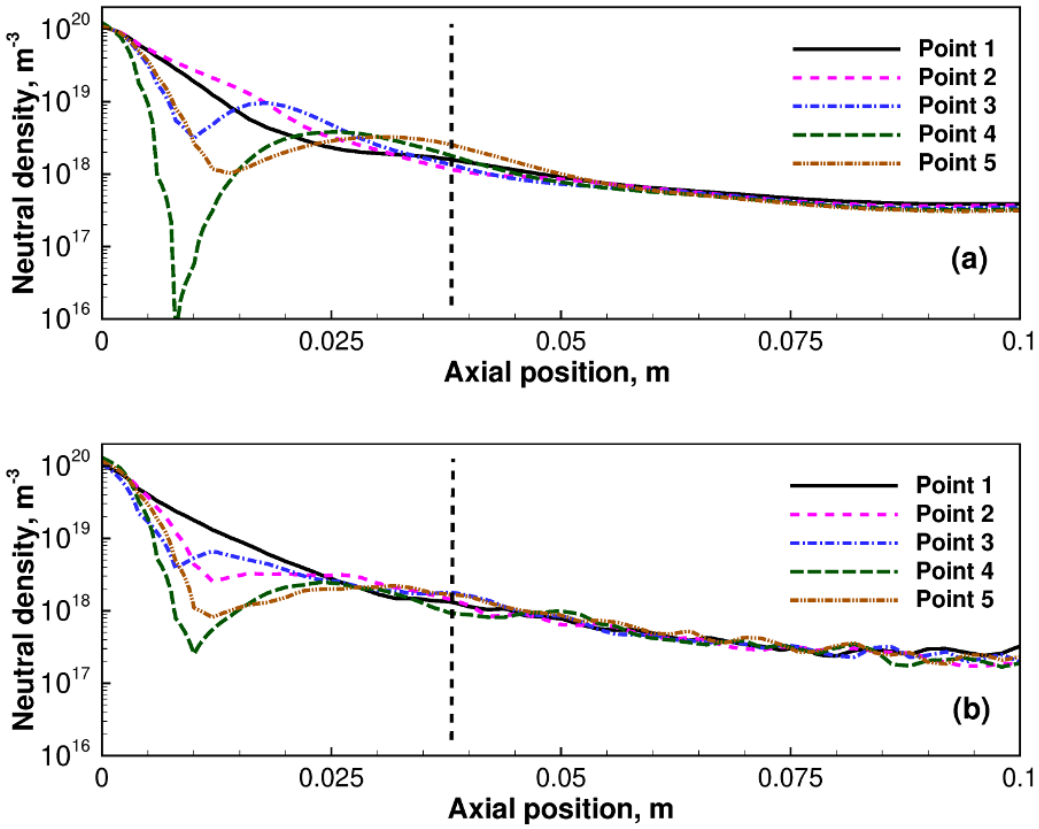

Figure 5.17: (a) Hybrid-DK and (b) hybrid-PIC neutral densities along the thruster channel centerline at different time instances.

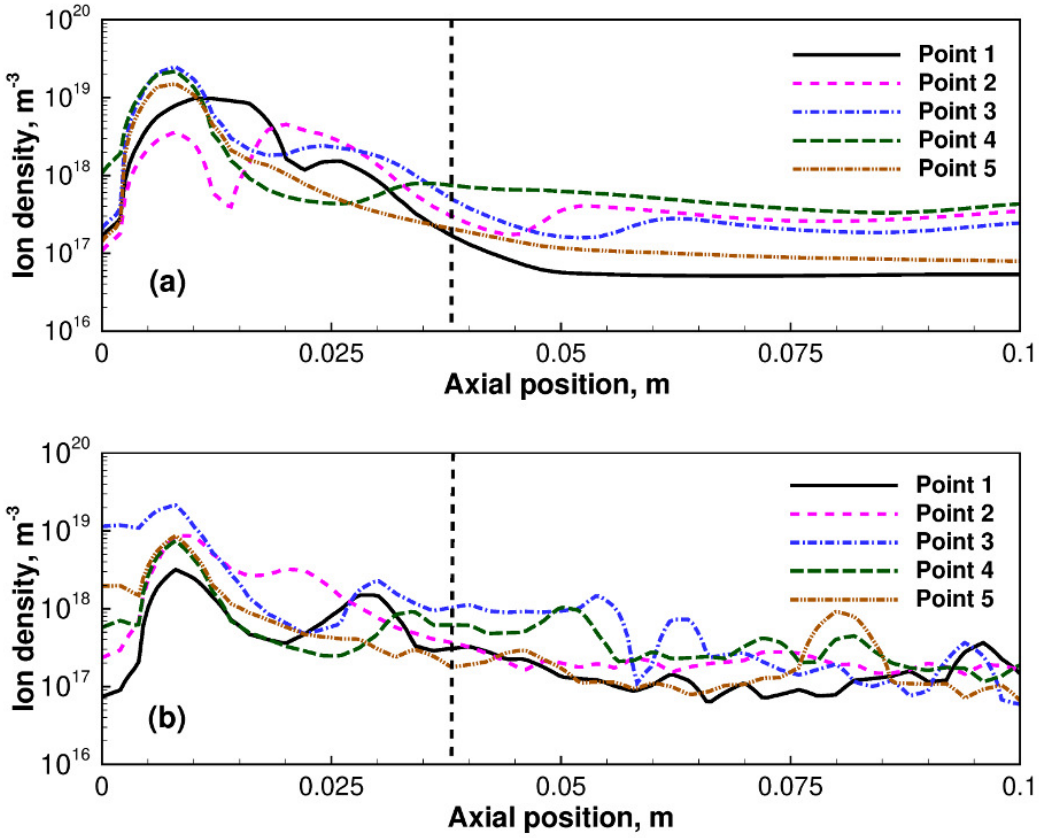

Figure 5.18: (a) Hybrid-DK and (b) hybrid-PIC ion densities along the thruster channel centerline at different time instances.

condition, since the plasma properties are well-resolved at the anode location. Even with a large number of macroparticles in the PIC simulation, the DK simulation is comparatively more computationally intensive and has a computational wall time approximately six times larger than that for the PIC simulation.

Results indicate that the DK algorithm greatly reduces the level of statistical noise produced by the PIC kinetic method. This is particularly evident in the lack of stochastic noise in the DK discharge current profile compared to the PIC current profile for a highly oscillatory case. Furthermore, the DK simulation captures a high frequency response that is not present in the PIC simulation, indicating that it is capable of responding to small changes in the electron dynamics. Lastly, the transient evolution of DK plasma properties in a low frequency case is more distinct, and plasma gradients are better resolved when compared to similar evolution of PIC plasma properties. In the future, efforts are required to validate the hybrid-DK simulation against experimental results, and to do so, it will be necessary to increase the fidelity of the quasi-one-dimensional electron algorithm to account for variable anomalous electron transport and secondary electron emission at the thruster channel walls, taking into account a variable sheath potential at the dielectric channel walls. Also, a more physically accurate description of the near-anode region will be required. Due to its high computational cost, the value of the DK simulation may partially lie in its ability to inform the required resolution of a PIC simulation to adequately model physical phenomena that are of interest.

CHAPTER VI

Two-Dimensional Plasma Sheath Model

6.1 Introduction and Motivation

In traditional SPTs, the anode is composed of a conducting material such as stainless steel, and channel walls are made of an insulating material such as boron nitride. Often, the anode surface is coated with a dielectric material which results in a change in the electrical properties in the near-anode region of the thruster channel. [99] While a plasma sheath, or a layer of non-zero electrical charge, forms at both conducting and insulating surfaces, the behavior of the sheath is inherently different at these two locations. At an insulating surface, the potential floats, and the net current to the surface is zero. A conducting surface, however, can draw a net current, and the potential is fixed. The emission characteristics of these two types of materials are very different, i.e. secondary electron emission (SEE) is lower for conducting materials than it is for insulating materials due to a lack of free electrons in the insulating material. With fewer free electrons, there are fewer electron-electron interactions, resulting in a larger mean escape depth for insulators ($\approx 10 - 50$ nm) than for conductors ($\approx 0.5 - 1.5$ nm). [100]

Plasma-wall interactions are very important in the Hall thruster, in part because high rates of erosion at the channel walls have historically limited the service lifetime of the device. [39] Due to magnetic shielding in newer thruster configurations, erosion of the channel walls has been significantly reduced. This is due to the fact that the electric field

intensity near the walls is lowered, reducing ion bombardment. [40] That said, recent studies show that the movement of the acceleration zone in magnetically shielded thrusters may result in increased erosion of thruster pole pieces, since the movement of the potential contours at the edge of the plasma beam causes high energy ions to accelerate radially toward the pole pieces. [41] Furthermore, the adaptive thruster has recently been proposed. This device would be capable of changing the main discharge type by actively adapting the channel wall parameters. Theoretically, this would be accomplished by synthesizing required nanomaterials in the thruster's own discharge and then depositing them onto specific locations inside the channel, modifying the channel wall surface characteristics by direct interactions with its own channel plasma. [101] As additional complexities are added to HET materials, it is important to characterize plasma-wall interactions accurately so that spatial and temporal plasma properties in the vicinity of the thruster surfaces are well understood. While a large body of work has been conducted for one-dimensional kinetic plasma sheath models, [12, 102, 103, 104] the insight into two-dimensional kinetic effects due to the variation of plasma properties in the vicinity of the sheath is limited.

The intent of this chapter is to provide a proof-of-concept two-dimensional DK model of a plasma sheath that highlights slight spatial differences inside the sheath as a result of electrically disparate, adjacent materials. Although the setup is not identical, inspiration for this work is drawn from Kim and Economou's work for a combined fluid/Monte Carlo simulation of a two-dimensional radio frequency (RF) sheath over a flat surface with an insulator/conductor interface in contact with a high density plasma. [105] While relevant to HETs, a non-uniform plasma sheath may also form in a number of other device, for example at the interface between a silicon wafer and the substrate holding the wafer in a plasma reactor. Section 6.2 provides a brief overview of plasma sheath theory. In Section 6.3, a one-dimensional plasma sheath is modeled within the two-dimensional DK framework to verify that the simulation is set up properly, and results correspond reasonably well with analytical predictions. Section 6.4 provides a proof-of-concept model of the two-dimensional

plasma sheath, and Section 6.6 comments on the challenges that are encountered in this work. Inclusion of additional physics of interest, such as secondary electron emission, is left for future work.

6.2 Theory

A sheath forms over any surface in contact with a plasma to balance the electron and ion currents lost from the plasma. For a conducting material, the potential of the material is fixed due to an internal electrical circuit, and the difference between the plasma potential and the material, or wall, potential determines the current balance. For an insulating material, the total current at each surface point must be zero, and a plasma sheath forms to maintain the appropriate charge balance to satisfy this condition at the surface. Plasma sheaths may be either ion-attracting or electron-attracting. In the former case, the wall potential is negative with respect to the plasma potential, attracting ions and repelling electrons, whereas in the latter case, the wall potential is positive, thereby attracting electrons and repelling ions. Electron-attracting sheaths are more rare than ion-attracting sheaths since electron extraction typically leads to an increase in the plasma potential, causing the sheath to become electron-repelling. However, a stable electron-attracting sheath may form in some devices including hollow-anode plasma sources, wire discharges, and possibly Hall thrusters. [106]

For any plasma sheath, SEE is an important phenomenon that occurs when ions, electrons, or photons impact the surface with sufficient energy to result in the emission of a secondary electron from the surface. In the case of a monotonic, ion-attracting sheath with electron emission, the total current will saturate when the ratio of secondary to primary electron flux reaches a certain, critical value. As a result, a potential well forms next to the wall, reducing the flux of primary electrons to the wall and reflecting back to the wall a portion of secondary electrons, thus limiting the electron emission and resulting in a non-

monotonic sheath structure. [50] This region of alternating positive and negative space charge is known as a space charge limited (SCL) sheath and is sometimes also referred to as a double sheath. [107]

In a plasma, the electric field can be written as $\mathbf{E} = -\nabla\phi$, and Gauss's Law reduces to the Poisson equation which describes the potential field as a result of the charge distribution. If the permittivity is constant, the Poisson equation is described by:

$$\nabla^2\phi = \frac{-e(n_i - n_e)}{\epsilon_0}. \tag{6.1}$$

When coupled with the appropriate boundary conditions, Eq. (6.1) is used to evaluate the potential and therefore the electric field everywhere in the domain. The positive electric field accelerates ions and electrons in different directions; it is inserted into the collisionless Vlasov equations for ion and electron species, and VDFs can be evaluated in phase space. In two dimensions, the kinetic expressions for ions and electrons are described by:

$$\frac{\partial f_i}{\partial t} + v_x\frac{\partial f_i}{\partial x} + v_y\frac{\partial f_i}{\partial y} + \frac{eE_x}{m_i}\frac{\partial f_i}{\partial v_x} + \frac{eE_y}{m_i}\frac{\partial f_i}{\partial v_y} = 0 \tag{6.2a}$$

$$\frac{\partial f_e}{\partial t} + v_x\frac{\partial f_e}{\partial x} + v_y\frac{\partial f_e}{\partial y} - \frac{eE_x}{m_e}\frac{\partial f_e}{\partial v_x} - \frac{eE_y}{m_e}\frac{\partial f_e}{\partial v_y} = 0 \tag{6.2b}$$

where i and e are subscripts for ions and electrons, respectively. Since there are no collisions, the ion and electron fluxes are constant throughout the sheath.

6.2.1 One Dimensional Plasma Sheath

For analytical purposes, consider a one-dimensional, ion-attracting sheath for which $x = 0$ is the wall and $x = L$ is the sheath edge. At the sheath edge, ions attain a speed greater than or equal to the sonic condition. This is known as the *Bohm criterion*, and the ion speed, u_0, is greater than or equal to the ion acoustic speed, $c_s = \sqrt{k_b T_e/m_i}$. Assuming that the

plasma density at the sheath edge, n_0, is constant, the following relationship for the ion density applies:

$$n_i = n_0 \left(1 - \frac{2e\phi}{k_b T_e M^2}\right)^{-1/2} \tag{6.3}$$

where $M = \frac{u_0}{c_s}$ is the ion Mach number. Eq. (6.3) can be derived from the ion continuity and energy conservation equations. The ion flux, $J_i = n_o u_0$, is constant since there are no collisions. The analytical ion VDFs in the sheath are obtained from a Bohm-velocity shifted Maxwellian distribution, namely: [7]

$$f_i(x, v_x) = \begin{cases} n_0 \left(\frac{m_i}{2\pi k_b T_i}\right)^{1/2} \exp\left[-\frac{m_i}{2k_b T_i}\left(\sqrt{v_x^2 + \frac{2e\phi}{m_i}} - u_0\right)^2\right] & v_x \leq -\sqrt{\frac{2e|\phi|}{m_i}} \\ 0 & v_x > -\sqrt{\frac{2e|\phi|}{m_i}} \end{cases} \tag{6.4}$$

Electrons travel much more quickly than ions due to their relatively low mass and typically higher temperature. For $|e\phi_w/k_b T_e| \gg 1$, the quasineutral condition holds at the sheath edge, $n_{e0} \approx n_0$, and the electron density can be approximated to follow the Boltzmann relation:

$$n_e = n_0 \exp\left(\frac{e\phi}{k_b T_e}\right) \tag{6.5}$$

The electron VDF inside the sheath can be given as: [7]

$$f_e(x, v_x) = \begin{cases} n_{e0} \left(\frac{m_e}{2\pi k_b T_e}\right)^{1/2} \exp\left[-\frac{m_e}{2k_b T_e}\left(\sqrt{v_x^2 + \frac{2e\phi}{m_e}}\right)^2\right] & v_x \leq v_c \\ 0 & v_x > v_c \end{cases} \tag{6.6}$$

where n_{e0} is the electron density at the sheath edge, $v_c = \sqrt{2e(\phi - \phi_w)/m_e}$ is the cutoff

velocity of truncated electrons due to the potential drop in the sheath, and the wall potential, $\phi_w < 0$. While ion velocities are typically less than zero (i.e. ion species travel exclusively toward the wall), electrons take on a range of both negative and positive velocities to satisfy the potential drop in the sheath. For a conducting surface, $\phi_w < 0$ is fixed, and the total current density, or the flux of the charge density, can be evaluated as $j_{tot} = j_i + j_e = eJ_i - eJ_e$, assuming that only singly charged ions are present in the plasma. For an insulating surface, $J_e = J_i$, and ϕ_w is obtained via the flux balance of charges as:

$$\phi_w = -\frac{k_b T_e}{e} \ln\left(\frac{1}{\sqrt{2\pi m_e/m_i}}\right) \tag{6.7}$$

6.3 Quasi-One Dimensional Plasma Sheath

To verify that the two-dimensional sheath simulation is set up properly, a conducting, ion-attracting plasma sheath without any variation of properties in the y-direction is simulated. It requires some care to implement conservative boundary conditions for the DK solver, particularly at the injection site; thus the DK boundary conditions are discussed in detail in Chapter IV.

6.3.1 Quasi-One Dimensional Plasma Sheath Simulation Setup

At the plasma edge of the sheath ($x = L$), the potential is set to zero, and $\phi = (\phi_w < 0)$ is applied at the wall ($x = 0$). The non-dimensionalized potential, $\Phi_w = e\phi/(k_b T_e) = -1.56$ V. The top and bottom of the domain are set with periodic boundary conditions for both the potential solver and the DK solver. HYPRE, a library of linear solvers available for parallelized processes, is used to calculate the potential everywhere in the domain. The rectangular simulation domain for this case, discretized by processor number, is shown in Fig. 6.1. The computational domain is $L = 30\lambda_D$ and $W = 0.2\lambda_D$. The grid is discretized as $\Delta x = 0.17\lambda_D$ and $\Delta y = 0.10\lambda_D$; $\Delta v_{x,i} = 0.025 c_s$ and $\Delta v_{y,i} = 0.100 c_s$ for ions; and

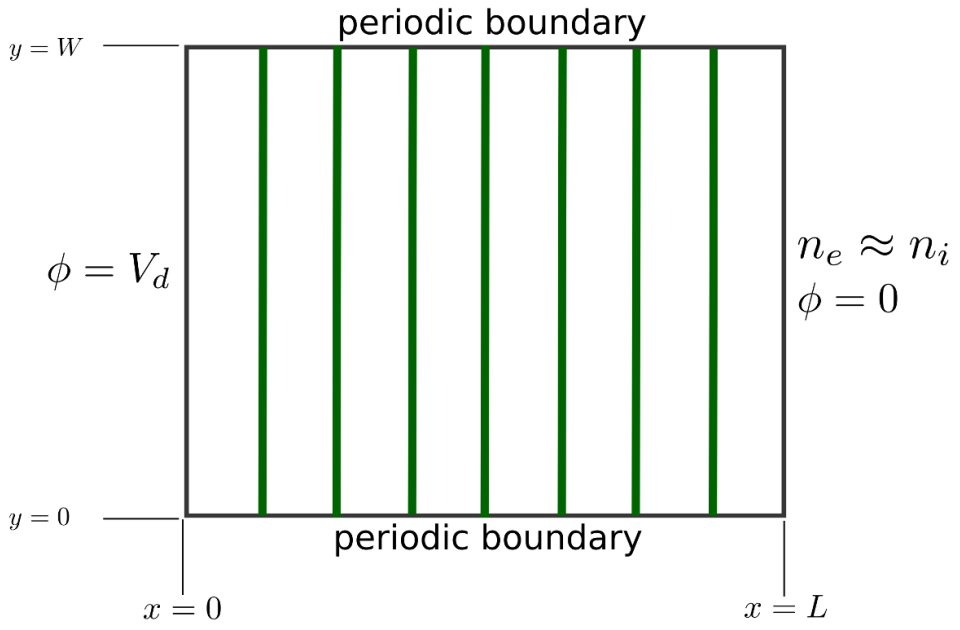

Figure 6.1: Quasi-one-dimensional plasma sheath domain highlighting processor arrangement. Image not to scale.

$\Delta v_{x,e} = 0.020 v_{th,e}$ and $\Delta v_{y,e} = 0.100 v_{th,e}$ for electrons. Note that $v_{th,e} = \sqrt{\frac{k_b T_e}{m_e}}$ is the electron thermal speed, and while properties in the y-direction must be discretized, it is not necessary to satisfy the ion CFL condition spatially in y since properties are fixed, and the VDF is not transported in this direction. Velocity space extents are $(v_{xi,min}, v_{xi,max}) = (-10c_s, 2c_s)$ and $(v_{xe,min}, v_{xe,max}) = (-6v_{th,e}, 5v_{th,e})$, and the time step is $\omega_{pe}\Delta t = 8 \times 10^{-3}$, where ω_{pe} is the electron plasma frequency. Injected ions are hydrogen molecules and are relatively close in temperature to electrons, i.e. $T_i = (2/3)T_e$. However, the plasma has a low overall temperature with $T_e = 1.5$ eV.

Particles are injected into the simulation domain with a Maxwellian distribution biased in the x-direction at the respective species's temperature at $x = L$. A zero-electric-field boundary condition is applied (discussed in Chapter IV), and quasineutrality is reasonably maintained ($n_i \approx n_e \approx 10^{16}$m^{-3}) in the boundary cells. Particles that reach the wall are absorbed, and nothing is reflected back into the simulation domain. The potential solver is

of second-order accuracy and utilizes a five-point stencil. Thus, Eq. (6.1) becomes:

$$\frac{\partial^2\phi}{\partial x^2} + \frac{\partial^2\phi}{\partial y^2} = -\frac{e}{\epsilon_0}(n_i - n_e) \tag{6.8}$$

and is discretized as follows:

$$\frac{\partial^2\phi}{\partial x^2} \approx \frac{\phi(k-1,j) - 2\phi(k,j) + \phi(k+1,j)}{\Delta x^2} \tag{6.9a}$$

$$\frac{\partial^2\phi}{\partial y^2} \approx \frac{\phi(k,j-1) - 2\phi(k,j) + \phi(k,j+1)}{\Delta y^2} \tag{6.9b}$$

where k represents the index in x and j represents the index in y. The Cartesian domain is discretized in an identical fashion for both the DK and Poisson solvers so that information exchange between the two solvers is straightforward. Both solvers calculate cell-centered, macroscopic quantities, and the Poisson solver uses a parallel semicoarsening multigrid (SMG) solver to solve the linear system of equations. [108] The simulation runs on a total of eight processors to $t \approx 21/\omega_{pi}$, where ω_{pi} is the ion plasma frequency, with a wall time of approximately 69 hours.

6.3.2 Quasi-One Dimensional Plasma Sheath Simulation Results

Time-varying, non-dimensionalized profiles of the ion velocity in x, electron and ion densities, and the plasma potential are shown as a function of x-position in Figs. 6.2, 6.3, and 6.4, respectively. These properties are shown at $\{50000, 100000, 150000\}$ iterations, which corresponds to $\{7/\omega_{pi}, 14/\omega_{pi}, 21/\omega_{pi}\}$. The last time instance (150,000 iterations) is determined to be near steady state since the variation in the velocity in the location at which ions achieve the sonic condition is less than 0.8% over a 5000 time step interval. For reference, early in the simulation, the variation in velocity was approximately 15% over the same time interval.

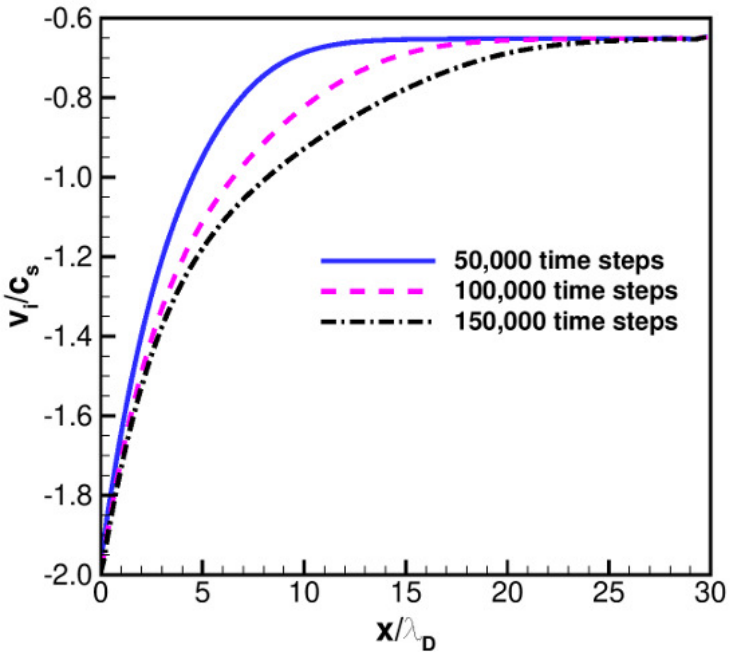

Figure 6.2: Time-varying ion velocity as a function of x-position in the quasi-1d plasma sheath.

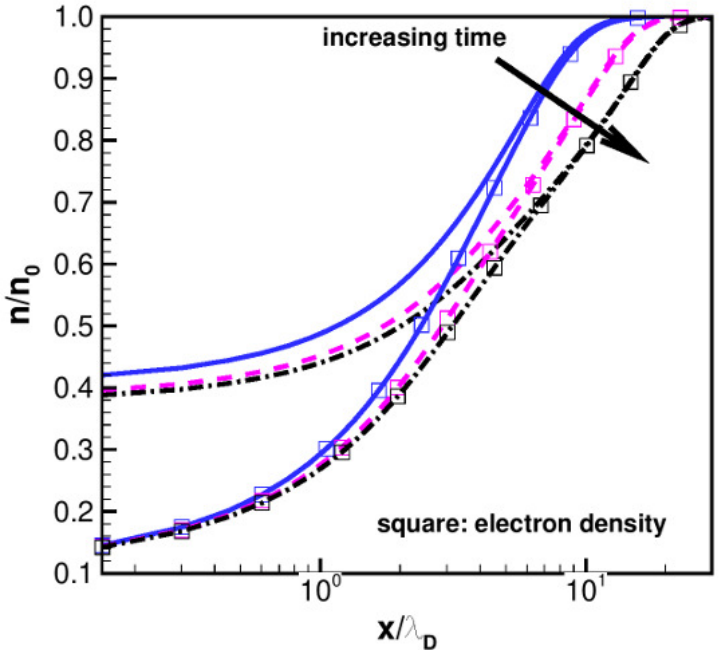

Figure 6.3: Time-varying ion and electron densities as a function of x-position in the quasi-1d plasma sheath.

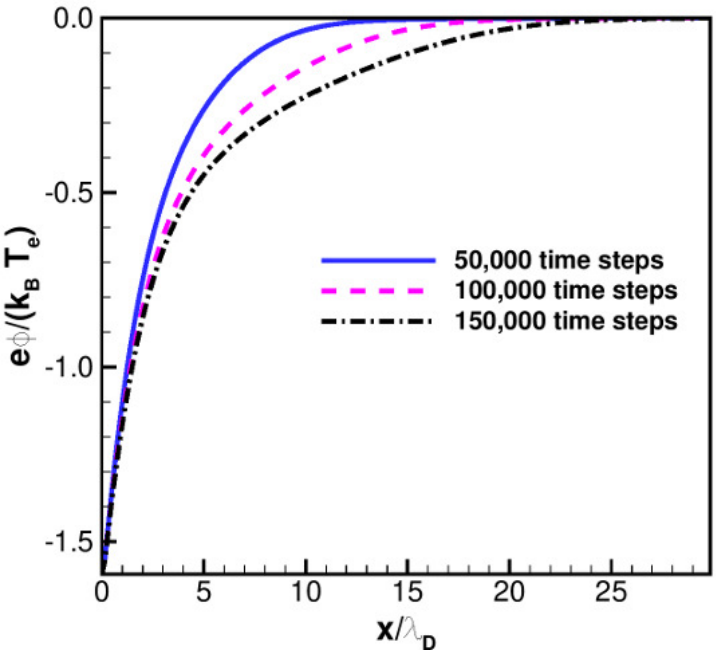

Figure 6.4: Time-varying potential as a function of x-position in the quasi-1d plasma sheath.

It is observed that the zero-field boundary condition works reasonably well at $x = L$, as there is negligible variation in the potential at that location, and the species' densities in Fig. 6.3 are within 1.0% of n_0. From Fig. 6.2, it is apparent that ions enter from the edge of the domain at $x = L$ with an average speed of approximately $0.65c_s$. Because ions enter the domain with a velocity below the ion acoustic speed, the sheath edge is not located at $x = L$. Instead, ions accelerate through a presheath-type structure, for which the plasma is nearly quasineutral (as shown in Fig. 6.3), and attain the Bohm velocity around $x = 8\lambda_D$ at steady state. The plasma potential in Fig. 6.4 decreases slightly up to the sheath edge ($x > \approx 8\lambda_D$) and then falls off abruptly inside the sheath. It is worth noting that the majority of this presheath-type structure has been avoided in one-dimensional simulations by Hara and Hanquist, perhaps due to the fact that their sheath simulations applied particle conservation within the domain. Hence, rather than injecting a density of n_0 at $x = L$, ions that passed through the boundary at $x = 0$ were re-injected at the subsequent time step. [12] As a

result, a source-type structure near $x = L$ formed, and ions were more quickly accelerated to reach the Bohm condition. This approach was not selected for the present work because of concern that the flux at the injection plane for the full two-dimensional case would vary spatially in the y-direction due to disparate wall fluxes caused by a variable wall potential. However, it is likely that such an approach is preferred for the one-dimensional case. Alternatively, it may be possible to shift the boundary cell VDF by the Bohm velocity so that particles enter the domain in a pre-accelerated state.

Because of the existence of a presheath-type structure in the results, it is somewhat difficult to compare computational results directly with plasma sheath theory. However, it is possible to verify that the electron flux to the wall is within a reasonably expected range and also that the truncated electron VDF corresponds with theoretical expectations. In each wall boundary cell, the electron flux to the wall (per unit area, per unit time) is calculated as $J_e \approx 4.10 \times 10^{20}$ m^{-2}s^{-1}. The analytical value of of the electron flux is calculated by taking the moment of the truncated electron VDF in Eq. (6.6):

$$J_e = \frac{n_{e0}}{4}\sqrt{\frac{8k_bT_e}{\pi m_e}}\exp\left(\frac{e\phi_w}{k_bT_e}\right) \tag{6.10}$$

From Eq. (6.10), the electron flux is calculated as approximately $J_e \approx 4.17 \times 10^{20}$ m^{-2}s^{-1}, indicating that the computational results agree with the theory within 2%.

Ion and electron VDFs are captured at a location near the wall ($x \approx 0.25\lambda_D$) and also at a location slightly removed from the wall ($x \approx 2.2\lambda_D$). These results are displayed in Fig. 6.5 and Fig. 6.6, respectively. Although the y-velocity is not particularly relevant for the problem at hand, it is also included to display the full two-dimensional output. It is clear from the plots that electrons take on a truncated VDF at both locations, as some electrons are repelled from the wall, and ions move only in the $-x$ direction toward the wall, as expected. Ions at $x \approx 0.25\lambda_D$ travel with a velocity that exceeds the acoustic speed. According to plasma theory, the truncated electron velocity, $\tilde{v}_c = v_c/v_{th,e} = \sqrt{2(\Phi - \Phi_w)}$,

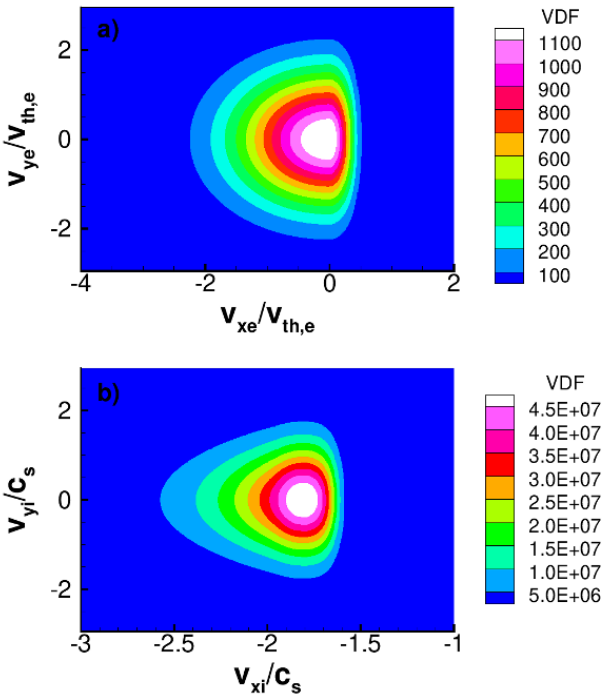

Figure 6.5: VDFs with arbitrary units at $x \approx 0.25\lambda_D$. In (a), the electron VDF is shown, and in (b), the ion VDF is shown.

where all properties are non-dimensionalized. The maximum electron VDF in Fig. 6.5 is located at an x-velocity of $v_{xe}/v_{th,e} = 0.53$, which corresponds exactly with the theory, using $\Phi(x) = -1.42$ V and $\Phi_w = -1.56$ V.

6.4 Two Dimensional Plasma Sheath

With reasonable results obtained for the quasi-one-dimensional case, a full two-dimensional simulation is constructed with a slight variability in the wall potential. Limitations based on available computational power and memory are encountered for this full kinetic case, limiting the scope of the physical parameters. However, it is intended to be a proof-of-concept model, and the results contain information of interest.

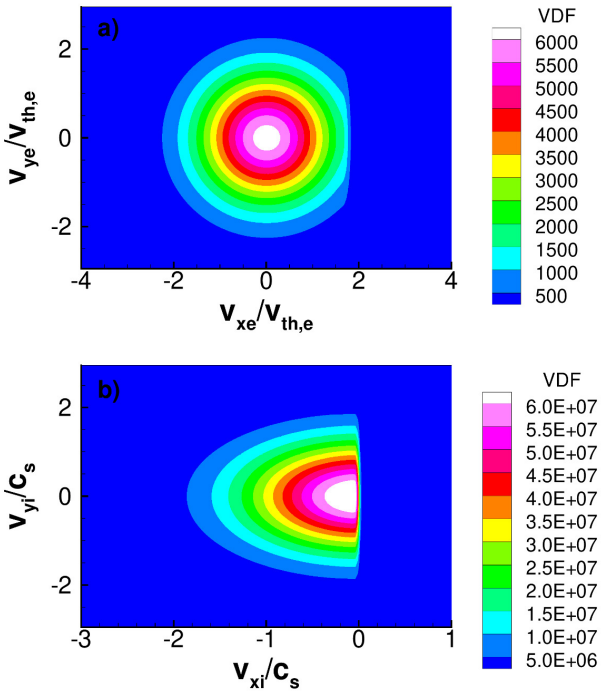

Figure 6.6: VDFs with arbitrary units at $x \approx 2.2\lambda_D$. In (a), the electron VDF is shown, and in (b), the ion VDF is shown.

6.4.1 Two Dimensional Plasma Sheath Simulation Setup

Due to discretization in y, the two-dimensional case requires substantially more physical and velocity bins than the quasi-one-dimensional case. Therefore, to satisfy memory requirements, the domain is decomposed in both the x and y directions, i.e. there are several processors used in both the x and y directions, and information must be exchanged between all adjacent processors. The boundary conditions are similar to those for the quasi-one-dimensional case, but there are some differences that are highlighted in Fig. 6.7. Namely, the wall potential is distinct between the top and bottom half of the wall on the left hand side. A pure Neumann (zero-slope) boundary condition in y is applied for the potential values calculated at the top and bottom of the domain, as it is assumed that the plasma there is far enough from the potential discontinuity located at $W/2$ that the radial electric field is negligible. To avoid odd behavior in the potential at the corners of the boundaries, a first-order accurate boundary condition is applied to the potential at $x = 0$ and $x = L$;

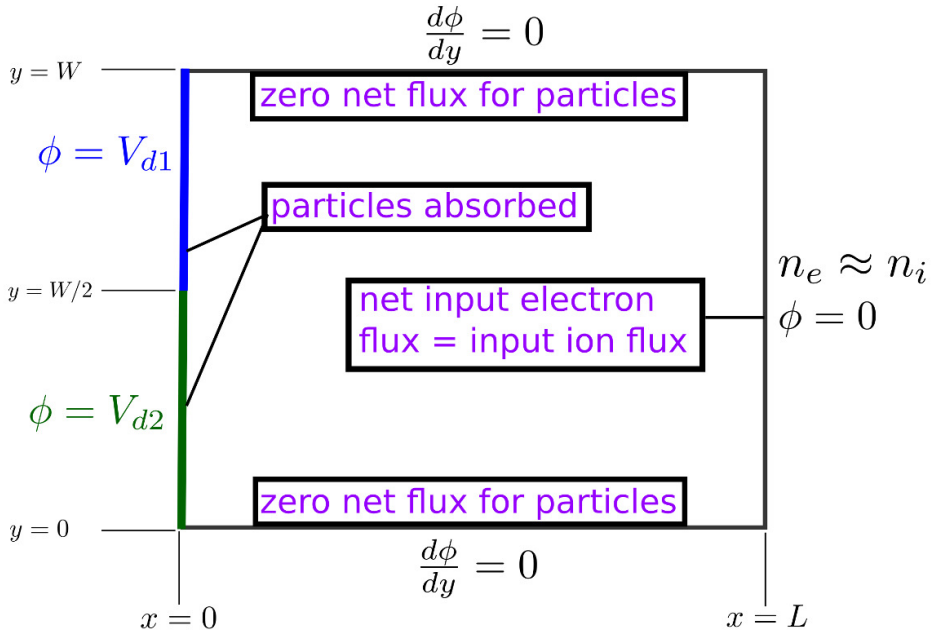

Figure 6.7: Two-dimensional plasma sheath domain, highlighting boundary conditions. Image not to scale.

at the top and bottom of the domain ($y = 0$ and $y = W$), second-order accurate boundary conditions are applied for the potential. Rather than apply a periodic boundary condition for the ion and electron VDFs at $y = 0$ and $y = W$, a zero-net flux condition is applied so that any particles that leave the domain are specularly reflected back into the domain. Since the top and bottom boundaries are located far from the discontinuity in the potential and the radial electric field is zero at the top and bottom boundaries, it is not expected that many particles with significant components of y-velocity will reach these locations. Provided that the y-velocity components are relatively small, the specular reflection mechanism will ensure that particles continue to travel in the x-direction toward the wall.

Unfortunately, memory requirements for the full case are prohibitive. As such, two-dimensional case parameters that are similar to those used in the quasi-one-dimensional case are applied when possible, but some differences are necessary. At the sheath edge ($x = L$), the potential is set to zero; $\phi = V_{d2}$ is applied at ($x = 0, y < W/2$), and

$\phi = V_{d1} = 0.9V_{d2}$ is applied at ($x = 0, y \geq W/2$). The computational domain is $L = 15\lambda_D$ and $W = 10\lambda_D$. The grid is discretized as $\Delta x = 0.18\lambda_D$ and $\Delta y = 0.16\lambda_D$; $\Delta v_{x,i} = 0.025c_s$ and $\Delta v_{y,i} = 0.025c_s$ for ions; and $\Delta v_{x,e} = 0.025v_{th,e}$ and $\Delta v_{y,e} = 0.020v_{th,e}$ for electrons. Velocity space extents in x are: $(v_{xi,min}, v_{xi,max}) = (-6c_s, 2c_s)$ and $(v_{xe,min}, v_{xe,max}) = (-6v_{th,e}, 3v_{th,e})$. In y, velocity extents are: $(v_{yi,min}, v_{yi,max}) = (-2c_s, 2c_s)$ and $(v_{ye,min}, v_{ye,max}) = (-3v_{th,e}, 3v_{th,e})$. The time step is $\omega_{pe}\Delta t = 8 \times 10^{-3}$. Ions are hydrogen molecules, and $T_i = (1/2)T_e$ with $T_e = 1.0$ eV.

6.4.2 Two Dimensional Plasma Sheath Simulation Results

The two-dimensional DK simulation is run on a total of 96 processors, utilizes approximately 180 GB of memory, and is run up to $t \approx 40/\omega_{pi}$ in approximately 11.5 days of wall time. Domain parameters, including the physical domain size, temperature range, and simulation memory allocation, have been optimized as much as possible to obtain the present results. The simulation is not yet at total steady state in these results, mainly due to the fact that numerical diffusion in velocity space is high. This is in part because y-velocity space has a somewhat coarse discretization. The coarse discretization in velocity space causes electrons to take on a large range of velocities initially (i.e. many electrons near the sheath edge have a large, positive velocity in x), and due to insufficient resolution of velocity space, it takes much more time for the sheath structure to form compared to the quasi-one-dimensional case. It should be noted that the overall simulation results do move toward a steady state condition, but because the average electron velocity at $x = L$ is still positive at $t \approx 40/\omega_{pi}$, it is not possible to say with certainty when a steady state condition will be reached. Particles are injected into the domain at $x = L$ with a Maxwellian distribution at the particle temperature, biased with x-velocity. The implication is that y-velocity space must span a range large enough to accommodate the VDF. However, since there is no electric field in y at the sheath edge, the VDFs require a very fine velocity discretization to accommodate small changes in in velocity in the y-direction. With the present memory re-

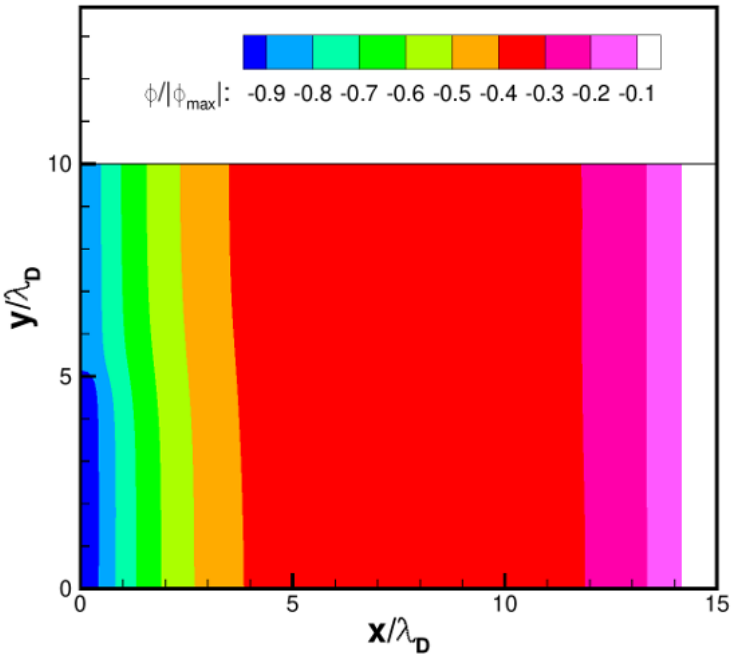

Figure 6.8: Instantaneous potential contour plot for the two-dimensional plasma sheath at $t \approx 40/\omega_{pi}$. The potential is normalized by the maximum potential in the domain.

quirements and computational limitations, it is not possible to achieve the desired velocity grid size in y with fixed velocity bin sizes.

In spite of computational limitations that hinder the desirable resolution of plasma properties, results are reasonable enough to warrant analysis and discussion. The instantaneous, normalized potential contours at $t \approx 40/\omega_{pi}$ are shown in Fig. 6.8. For this case, there is a slight source sheath located near $x = L$. The potential is reasonably constant throughout the remainder of the simulation domain to a point near the wall, where the potential falls to satisfy the ion-attracting sheath condition. The potential fall is somewhat gradual, as a steady state condition has not been completely obtained.

In Fig. 6.9, ions in the vicinity of the potential discontinuity at $y = W/2$ can be seen streaming slightly downward, toward the more negative potential V_{d2}, located at $y < W/2$. In this figure, instantaneous ion velocity streamlines are overlaid on a contour plot of the radial electric field at $t \approx 40/\omega_{pi}$. Since the potential difference between V_{d1} and V_{d2} is small ($V_{d1} = 0.9V_{d2}$), the ion radial velocity in Fig. 6.9 is multiplied by a factor of ten to

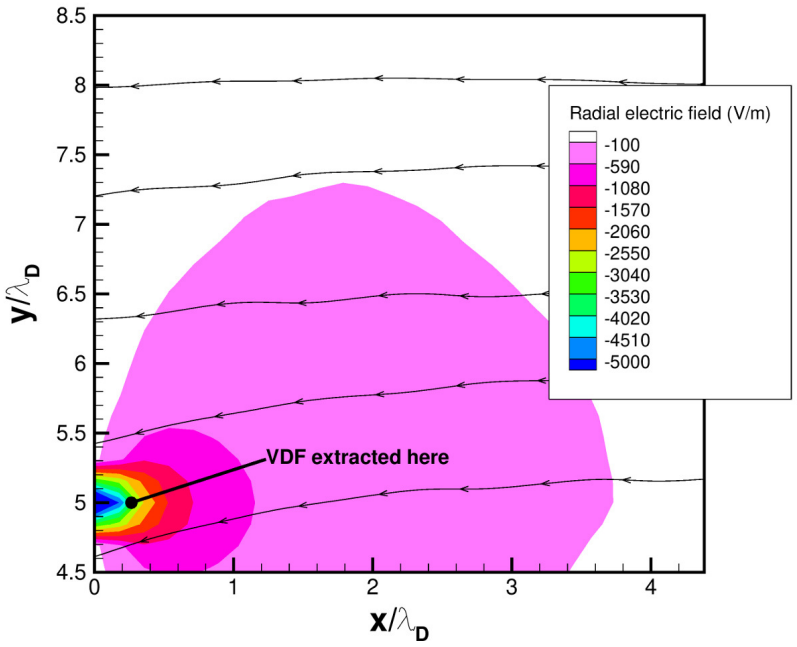

Figure 6.9: Ion velocity streamlines overlaid on a contour plot of the radial electric field. To exaggerate the effect, since the potential difference is small, v_{yi} is multiplied by a factor of ten. Note that $y/\lambda_D = 5$ corresponds to $y = W/2$.

exaggerate the effect of the larger sheath potential located at $y < W/2$. At approximately $y/\lambda_D = 8$, velocity streamlines have little to no component of negative y-velocity, indicating that the two-dimensional effects have a span of approximately $3\lambda_D$ in y for this case. As expected, the radial electric field is largest in the vicinity of the potential discontinuity.

Electron and ion VDFs located near the potential discontinuity ($x = 0.27\lambda_D, y = W/2$) are extracted from the location highlighted in Fig. 6.9 and shown in Fig. 6.10. Note that the top half of the physical cell is located above $y = W/2$, and the lower half of the cell is located below $y = W/2$, where the potential discontinuity is located. Particularly for the electron VDF in Fig. 6.10a, it is possible to see that the portion of the VDF in negative y-velocity space (i.e. particles traveling downward, toward the more negative potential) displays a larger spread of velocities for $v_x > 0$ compared to the VDF in positive y-velocity space, since the larger potential drop for $y < W/2$ corresponds with more repelled electrons. Since particles are located very near the wall, the ion VDF in Fig. 6.10b displays

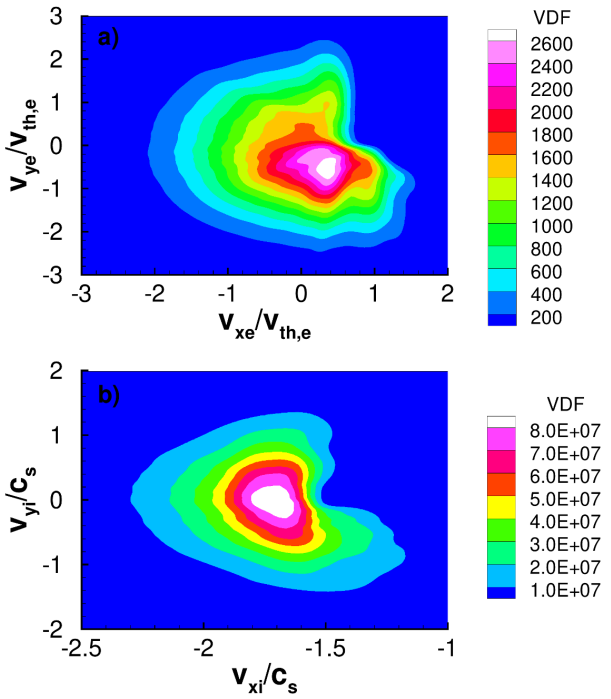

Figure 6.10: VDFs with arbitrary units at ($x = 0.27\lambda_D, y = W/2$), i.e. located near the potential discontinuity. In (a), the electron VDF is shown, and in (b), the ion VDF is shown.

velocities with magnitudes greater than the ion acoustic velocity, as particles must be accelerated sufficiently to enter the sheath at this location. The spread of velocities in x is also slightly larger for ions in negative y-velocity space.

Electron and ion VDFs are also sampled directly downstream of the potential discontinuity at ($x = 2.0\lambda_D, y = W/2$). These results, displayed in Fig. 6.11, indicate that the electron and ion VDFs are not heavily influenced by two-dimensional effects at this location, as they are mostly symmetric in velocity space. There is some distortion in both the electron and ion VDFs, i.e. the VDFs are not perfectly symmetric about $v_y = 0$, and while some of the distortion is likely numerical, it may also indicate that the VDF is beginning to evolve at this spatial location so that it will match the one shown near the wall in Fig. 6.10. Numerical distortion is primarily present in the macroscopic plasma properties themselves. For example, the normalized electron density in Fig. 6.12, while overall reasonable, exhibits some numerical artifacts in the y-direction. The numerical artifacts are primarily exhibited in the form of density oscillations in the y-direction.

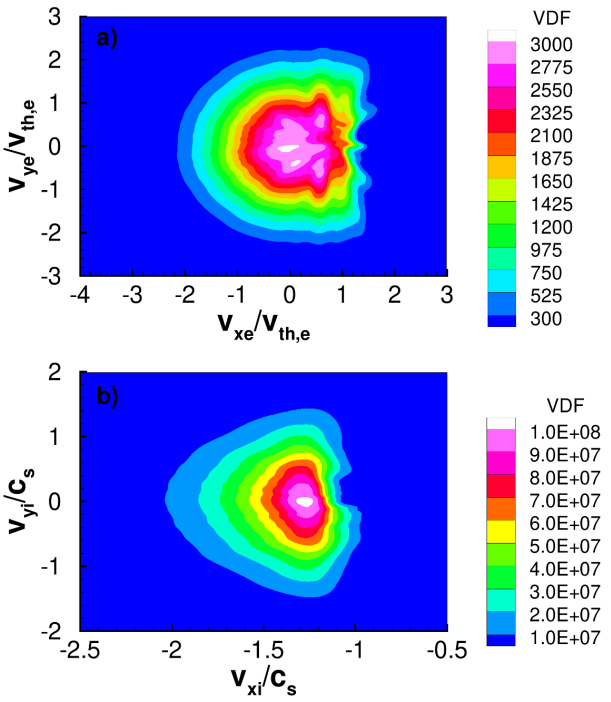

Figure 6.11: VDFs with arbitrary units at $(x \approx 2.0\lambda_D, y = W/2)$, i.e. directly downstream of the potential discontinuity. In (a), the electron VDF is shown, and in (b), the ion VDF is shown.

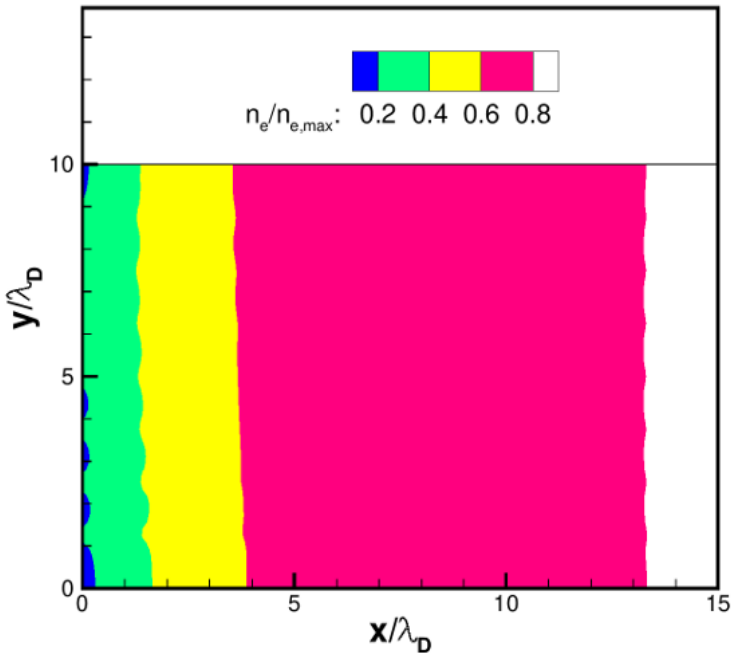

Figure 6.12: Instantaneous electron density contours for the two-dimensional plasma sheath at $t \approx 40/\omega_{pi}$. The density is normalized by the maximum density in the domain.

6.5 Summary

The chapter is intended to provide a proof-of-concept model of a two-dimensional DK plasma sheath that highlights slight spatial differences inside the sheath as a result of electrically different, adjacent materials. To accomplish this goal, a one-dimensional sheath is first built in the two-dimensional DK framework, and results are verified with theoretical expectations. Then, the full two-dimensional sheath is modeled. A proof-of-concept model shows that two-dimensional effects are present in the vicinity of the discontinuous plasma potential, resulting in a finite quantity of ions that gain a y-component of velocity and stream toward the more negative wall potential. The electron and ion VDFs both clearly exhibit changes due to two-dimensional effects.

6.6 Discussion of Challenges that were Encountered

Computational requirements make it challenging to fully resolve the two-dimensional kinetic plasma sheath. Results indicate that it is necessary to make some alterations to the model in order to consider full plasma sheath physics, including SEE processes, which would require the addition of another electron species. Specifically, the simulation allocates a large amount of memory to velocity space discretization for each species. This, in conjunction with a large number of serial operations to update the VDFs on each processor, results in an intractable simulation at large scales.

In Chapter IV, it is observed that the simulation time increases significantly for a neutral-only HET simulation if processors are not doubled when the Cartesian cell count is doubled (and the velocity bin size is unchanged). If, on the other hand, the processor count is doubled when the physical cell count is doubled, the simulation time for an identical number of computational steps (not total t), also doubles. This implies that the serial computational load increases by a factor of approximately two when the physical cell count doubles, assuming that the processor count is close to optimal. Therefore, to achieve the

same simulation time, i.e. adjusting the CFL condition, the optimized simulation time increases by a factor of approximately four (when the physical cell count is doubled). For the same test cases, it is observed that halving the size of each velocity bin (without changing the processor count) increases the total computational load and time by a factor of approximately six. For this reason, sufficient but somewhat coarse physical and velocity grids are selected for the full plasma simulation in Chapter V.

The two-dimensional plasma sheath simulation contains $320 \times 160 = 51200$ velocity bins for ions in each cell and $360 \times 300 = 108000$ velocity bins for electrons, resulting in a total of 159200 velocity bins. Each physical sub-domain contains $7 \times 8 = 56$ physical cells. The HET hybrid-DK simulation discussed in Chapter V contains $108 \times 240 = 25920$ velocity bins for neutral atoms and $230 \times 140 = 32200$ velocity bins for ions, resulting in a total of 58120 velocity bins. The size of each physical sub-domain varies slightly, but inside the channel, each processor is allocated $3 \times 13 = 39$ physical cells. Thus, the plasma sheath velocity bin count is higher by a factor of approximately 2.75, and the physical cell count is also higher by a factor of approximately 1.4. Thus, if the sheath simulation in its present state were to achieve a performance similar to the HET simulation (not accounting for the extra serial load that is incurred by doubling the cell count), the processor count would need to be at least doubled from 96 processors to 192 processors.

However, one of the primary challenges with the DK sheath simulation results is related to present velocity discretization, which is not fine enough to account for small y-velocities. Rather than applying a finer discretization to all of velocity space, one possible solution may be to utilize adaptive meshing techniques, which were briefly mentioned in Chapter III. Adaptive mesh refinement (AMR) has been used in a variety of systems to minimize computational overhead. [63, 109] Such techniques utilize an adaptive mesh that evolves as the characteristic of the VDF develops, allowing for higher resolution in those parts of phase space that require it to achieve the desired accuracy. High order numerical schemes ensure that regions with a coarse mesh are still well-resolved. Furthermore, work

by Wettervik et. al demonstrated a typical speed-up factor of approximately seven for a one-dimensional system. [63] Such techniques are promising for the two-dimensional DK simulation but will be left for future work.

CHAPTER VII

Conclusions

This thesis has been primarily concerned with the two-dimensional modeling of a discharge plasma via the direct kinetic (DK) method. This chapter provides a summary of the work contained in this thesis and presents the most important conclusions from each chapter. Then, the author's unique contributions are recorded, and future studies that may enhance the presented work through further research are recommended.

7.1 Dissertation Summary

In Chapter I, the general motivation for this dissertation was provided, and the characteristics of a plasma were introduced. An overview of numerical modeling techniques for gases and plasmas was presented, and the concept of space propulsion was reviewed. The physical processes surrounding the Hall effect thruster were detailed, and present research challenges associated with the device were highlighted. Specific research objectives for the dissertation work were outlined, and the goal of the thesis was made clear: to improve the state-of-the art modeling methods for the Hall effect thruster and to better understand the capabilities and limitations of the herein utilized modeling techniques, which include hybrid-DK and hybrid-PIC methods.

In Chapter II, the equations that govern the motion of the species that make up the discharge plasma in a HET were derived. The magnetic field configuration and its relationship to the electron simulation grid was described, and the electron fluid equations were detailed

at length. Kinetic equations that govern more massive ions and neutral particles were also discussed. Other important concepts including current conservation, relevant particle collisions, and electron transport mechanisms were outlined.

In Chapter III, techniques for solving the equations from Chapter II were described. The hybrid-DK and hybrid-PIC numerical methods were introduced, and these distinct Eulerian and Lagrangian methods were described in detail. The DK and PIC methods were compared and contrasted, highlighting areas of importance including computational size requirements and numerical error. Existing hybrid-PIC HET simulations were reviewed, and the general simulation framework was described. Then, the fluid electron algorithm was detailed, and finally, kinetic ion and neutral algorithms for both the discretized DK and PIC models were characterized.

Chapter IV discussed the development and implementation of conservative boundary conditions for the two-dimensional DK simulation. Specifically, wall collisions and particle injection were considered with respect to the hybrid-DK simulation of the discharge plasma in a Hall effect thruster. A sheath injection boundary condition, unique to a DK plasma sheath simulation, was also described in detail. The methods discussed for these boundaries all required that the particle flux be accurately calculated for each species in question, controlled when required, and that transformation in velocity space for different species be applied properly, taking into account the specific numerical integration scheme.

In Chapter V, a hybrid-DK simulation was benchmarked with a comparable hybrid-PIC simulation, and it was demonstrated that the DK algorithm reduced the level of statistical noise in the simulation results while obtaining similar time-averaged results compared to the PIC simulation. The equations from Chapter II and numerical methods from Chapter III, in conjunction with newly developed, conservative boundary conditions from Chapter IV, culminated in a two-dimensional, hybrid-DK simulation of a Hall effect thruster discharge plasma. Both the DK and PIC discharge current profiles and the time-averaged plasma properties matched reasonably well between the two simulations, indicating that

the benchmarking effort was successful, and that the performance of the two-dimensional DK algorithm was acceptable compared to the PIC algorithm. The DK simulation was found to be more sensitive than the PIC simulation to electron boundary conditions since the plasma properties are well-resolved everywhere in the domain. Furthermore, the DK simulation captured a high frequency response that was not present in the PIC simulation, indicating that it is capable of responding to small changes in electron dynamics. Even with a large number of macroparticles in the PIC simulation, the DK simulation was comparatively more computationally intensive, with a wall time approximately six times larger than that for the PIC simulation. It was predicted that the computational cost of the two-dimensional DK algorithm itself was nearly two orders of magnitude higher than that of the PIC algorithm. Due to its high computational cost, the value of the DK simulation was determined to lie at least partially in its ability to inform the required resolution of a PIC simulation to adequately model physical phenomena that are of interest.

Chapter VI considered the verification and development of a two-dimensional DK model for a collisionless plasma sheath. Such a sheath may form in a HET plasma as well as in a variety of other discharge plasmas. The intent of this chapter was ultimately to provide a proof-of-concept model of a two-dimensional DK plasma sheath that highlighted slight spatial differences inside the sheath as a result of electrically different, adjacent wall materials. After discussing plasma sheath theory, a verification case for a one-dimensional plasma sheath was modeled, and results corresponded reasonably well with analytical predictions. A proof-of-concept, two-dimensional plasma sheath model indicated a capability for high resolution results and showed expected slight differences in plasma properties due to an electrically-inhomogeneous surface. However, the simulation was both computationally intensive as well as expensive, and it was not possible to attain the desired resolution for the velocity space discretization everywhere due to DK memory requirements. For this reason, it was recommended that such a simulation undergo adaptive grid modification in future work.

7.2 Contributions

This dissertation work was ultimately focused on furthering state-of-the-art Hall thruster models, utilizing a high fidelity, two-dimensional, direct kinetic simulation technique. High-fidelity modeling is an important component of HET research since such computational models are useful and necessary to investigate the physical processes that affect a thruster's performance, efficiency, and lifetime limitations. To that end, the following, specific contributions are included in this dissertation:

- A two-dimensional, hybrid-DK simulation of a Hall thruster channel and its near-field plume was created and developed. This massively parallelized simulation was computationally intensive to test. Based on sensitivities to the electron algorithm, including boundary conditions and electron transport coefficients, many test simulations and parameter updates were conducted to achieve a stable simulation.

- An existing two-dimensional, hybrid-PIC simulation was modified for a comparative DK-PIC study, and some corrections were made to the existing hybrid-PIC model. Extensive test cases were simulated to ensure that macroparticle counts were sufficient for reasonable comparison with deterministic DK results. A study on the limitations of the MCC collision algorithm was conducted.

- Conservative kinetic boundary conditions for the DK algorithm were developed and implemented for particle-wall collisions in a Hall thruster. At a wall boundary, an accurate particle flux was calculated for each species, controlled when required, and a transformation in velocity space was applied for recombination, taking into account the numerical integration scheme. Additionally, DK particle injection techniques and limitations were examined and modified to ensure that said techniques were consistent with PIC injection techniques.

- To the extent possible within the quasi-one-dimensional electron simulation frame-

work, anode boundary conditions were developed. This was necessary to provide solution stability and reasonable plasma evolution for both the DK and PIC simulations since the resolution of the near-anode region was increased from prior hybrid-PIC simulations.

- The hybrid-DK simulation was benchmarked with a comparable hybrid-PIC simulation, using the UM/AFRL P5 Hall thruster, and it was demonstrated that the DK algorithm reduced the level of statistical noise in the simulation results while obtaining similar time-averaged results compared to the PIC simulation. The DK simulation captured a high frequency response that was not present in the PIC simulation, indicating that it is capable of responding to small changes in the electron dynamics.

- A two-dimensional, collisionless DK plasma sheath model was created, verified, and developed. To that end, a conservative kinetic boundary condition was developed for particle injection at the sheath edge. Limitations of the two-dimensional algorithm due to computational memory requirements were encountered and discussed.

7.3 Future Work

Although the state-of-the-art HET simulation technique was improved in this work, there is much that can be done in the future to further the DK approach to HET modeling. A seemingly natural step is to expand the HET benchmarking study into a simulation validation, i.e. comparing simulation results to experimentally-measured plasma properties in a HET. There are several steps that are required to achieve this. Some of these steps were carried out over the course of this work, but the author chose not to pursue them further for some important reasons which will be described later in this section. Nonetheless, if the existing hybrid-DK simulation were to be used for validation purposes, the following items would be desirable to complete the validation process:

- The method to calculate the current discussed in Chapter II assumes that the potential is fixed at the virtual anode and cathode locations. Strictly speaking, the anode potential is not fixed, since a potential drop is often present due to the formation of a plasma sheath. A Newton-Raphson solver can be used to implement a solution technique for the discharge current that is dependent on the value of the anode sheath potential, as outlined in Reference [110].

- It is necessary to include the contribution of the wall plasma sheaths inside the HET channel, as they affect the behavior of the plasma discharge. This will likely involve a modification of DK boundary conditions.

- Additional species and collision types may be added to the simulation, i.e. doubly charged ions and neutrals excited via charge exchange collisions. It is important to note that each of these additional species requires its own velocity space discretization and therefore increases the computational memory requirements for the overall simulation.

- A parameterization study may be performed to examine the impact that the variation in anode potential, gas flow rate, and other input parameters have on dynamic DK properties, such as the ion VDFs.

In the present work, the indication was that the quasi-one-dimensional fluid electron algorithm was of low fidelity compared to the two-dimensional DK algorithm used for ions and neutral atoms, and it was challenging to impose effective electron boundary conditions that did not lead to non-physical behavior in the DK domain. As such, it was determined that further evolution of the DK portion of the hybrid simulation may not be advisable. Instead, the electron algorithm should be upgraded to a fully two-dimensional model, enabling the proper resolution of near-anode plasma properties. Since it is likely that the DK method is capable of capturing highly oscillatory behavior caused by electron motion, a higher order electron algorithm is a particularly reasonable measure. Then, some of the

above listed measures can be incorporated into the simulation. Additionally, it is important to note that many hybrid-PIC simulations have applied time-averaged, variable electron transport models and effectively tuned these models until they closely matched experimental measurements. Based on the high computational cost for the DK model, this kind of tuning method does not make sense unless a good machine learning technique can be applied. It is also worth noting that, if dynamic electron transport processes are assumed for future simulations, it may be necessary to consider the DK method rather than the PIC method so that high frequency oscillations due to the electron algorithm are not damped out by statistical noise due to the PIC algorithm. Although it is computationally costly, the DK method is capable of capturing highly oscillatory behavior.

Aside from the HET study, a two-dimensional DK plasma sheath simulation was verified and developed. The eventual intent of this work is to obtain noiseless results that can be used to extract interesting information about the two-dimensional kinetic effects in the vicinity of a plasma sheath. However, results indicated that it is necessary to make some alterations to the model in order to consider full plasma sheath physics, including SEE processes, which would require the addition of another electron species. One of the primary challenges with the DK sheath simulation was related to the discretization of velocity space. Rather than applying a finer discretization to all of velocity space, one solution might be to utilize adaptive meshing techniques for the multi-dimensional DK method in the future.

AMR has been used in a variety of systems to minimize computational overhead. [63, 109] The general idea of adaptivity is to represent a complex system by reducing the number of elements, thereby decreasing computational time and memory requirements for the simulation. This typically requires a trade-off between numerical volume (computer memory, number of operations, etc) and implementation complexity (data structures and algorithms). [111] For grid-based methods, AMR techniques typically utilize an adaptive mesh that evolves as the characteristic of the VDF develops, allowing for higher resolution in those parts of phase space that require it. High order numerical schemes ensure

that regions with a coarse mesh are still well-resolved. In recent years, AMR techniques have undergone development for simulations that model weakly collisional plasmas, but ultimately, it is a relatively new area of research. Challenges of extending such techniques from simulations of gas dynamics to weakly collisional plasma simulations are primarily associated with distinct scales between electron and heavy particle transport. [112] Work by Wettervik et. al demonstrated a typical speed-up factor of approximately seven for a one-dimensional system of a collisionless plasma. [63] Roytershteyn and Delzanno introduced a parallelized, three-dimensional spectral plasma solver and applied the method to a problem of turbulence in weakly collisional plasmas, reproducing the expected statistical properties of magnetic and electron fluctuations observed in PIC simulations. [113] The DK simulation is capable of providing excellent resolution of plasma properties, but it is computationally expensive. Therefore, it may benefit from the application of a technique such as AMR. Once could even imagine a fully adaptive DK simulation of a HET in which the hybrid fluid-kinetic approach is not utilized; the simulation would instead adapt between fluid and direct kinetic techniques for all the involved species, utilizing adaptive mesh and algorithm refinement methods. Such a model certainly would not be a trivial undertaking, but algorithm development techniques in conjunction with the availability of computational power may make such a project realizable in the future.

APPENDIX A

Terms and Discretizations in the Electron Energy Fluid Equation

Tables A.1 and A.2 list the various terms and discretizations that are incorporated into the discretized electron energy equation, discussed in Chapter III. Note that the fully discretized electron energy equation is described by the following expression:

$$\begin{aligned}\frac{\partial \epsilon_V}{\partial t} = & \frac{-A_2}{A_1}\epsilon_V \\ & - \frac{A_3}{A_1}\epsilon_{S_1} - \frac{A_4}{A_1}\left(\epsilon\frac{\partial \epsilon}{\partial \lambda}\right)_{S_1} - \frac{A_5}{A_1}\epsilon_{S_2} - \frac{A_6}{A_1}\left(\epsilon\frac{\partial \epsilon}{\partial \lambda}\right)_{S_2} \\ & + \frac{A_7}{A_1}\left(\epsilon\frac{\partial \epsilon}{\partial \lambda}\right)_{S_1} + \frac{A_8}{A_1}\left(\epsilon\frac{\partial \epsilon}{\partial \lambda}\right)_{S_2} \\ & - \frac{A_9}{A_1} - \frac{A_{10}}{A_1}\frac{\partial \epsilon_V}{\partial \lambda} - \frac{A_{11}}{A_1}\frac{\partial \epsilon_V}{\partial \lambda}\frac{\partial \epsilon_V}{\partial \lambda} - \frac{A_{12}}{A_1}\left(\epsilon\frac{\partial \epsilon}{\partial \lambda}\right)_V - \frac{A_{13}}{A_1}\epsilon_V \\ & - \frac{A_{14}}{A_1}k_{e-Xe}(\epsilon_V)\epsilon_V - \frac{A_{15}}{A_1}\nu(\epsilon_V)_{walls}\epsilon_V - \frac{A_{16}}{A_1}k_{e-Xe^+}(\epsilon_V)\epsilon_V \end{aligned} \tag{A.1}$$

Table A.1: Terms in the Electron Fluid Energy Equation

Term	Value
A_1	$\int_V n_e dV$
A_2	$\int \frac{\partial n_e}{\partial t} dV$
A_3	$\int_{S_1} -\frac{5}{3} n_e k_1 j_1 dS$
A_4	$\int_{S_1} -\frac{5}{3} n_e (k_1 j_2 + k_2) dS$
A_5	$\int_{S_2} \frac{5}{3} n_e k_1 j_1 dS$
A_6	$\int_{S_2} \frac{5}{3} n_e (k_1 j_2 + k_2) dS$
A_7	$\int_{S_1} -\frac{10}{9} n_e \mu_{e,\perp} r B dS$
A_8	$\int_{S_2} \frac{10}{9} n_e \mu_{e,\perp} r B dS$
A_9	$\int_V n_e k_1 j_1^2 h_1 dV$
A_{10}	$\int_V n_e k_1 j_1 (h_1 j_2 + h_3) + n_e h_1 j_2 (k_1 j_2 + k_2) dV$
A_{11}	$\int_V n_e (k_1 j_2 + k_2)(h_1 j_2 + h_3) dV$
A_{12}	$\int_V n_e h_2 (k_1 j_2 + k_2) dV$
A_{13}	$\int_V n_e k_1 j_1 h_2 dV$
A_{14}	$\int_V n_e n_a dV$
A_{15}	$\int_V n_e dV$
A_{16}	$\int_V n_e n_{Xe^+} dV$

Table A.2: Discretizations in the Electron Fluid Energy Equation

Term	Discretization
ϵ_V	ϵ_i
ϵ_{S_1}	$\frac{\epsilon_i + \epsilon_{i-1}}{2}$
ϵ_{S_2}	$\frac{\epsilon_i + \epsilon_{i+1}}{2}$
$\left(\epsilon \frac{\partial \epsilon}{\partial \lambda}\right)_{S_1}$	$\frac{\epsilon_i + \epsilon_{i-1}}{2} \frac{\epsilon_i - \epsilon_{i-1}}{\lambda}$
$\left(\epsilon \frac{\partial \epsilon}{\partial \lambda}\right)_{S_2}$	$\frac{\epsilon_i + \epsilon_{i+1}}{2} \frac{\epsilon_{i+1} - \epsilon_i}{\lambda}$
$\frac{\partial \epsilon_V}{\partial \lambda}$	$\frac{\epsilon_{i+1} - \epsilon_i}{2\lambda}$

APPENDIX B

Neutral Atom Simulations in Planar and Axisymmetric Domains

The hybrid-DK simulation utilizes two dimensions in velocity space for both neutral particles and ions. Since the hybrid-PIC simulation uses an axisymmetric configuration for neutral particles (2D3V), it is verified that the alternate approaches are compatible for benchmarking. Planar (2D2V) and axisymmetric (2D3V) neutral atom simulations are performed using MONACO, a DSMC solver. The simulation domain is nearly identical to that used to model the UM/AFRL P5 Hall thruster in Chapter V. The thruster channel has a length of 3.8 cm, and particles are injected into the domain at the thruster channel centerline ($r = 7.25$ cm).

Results in Figs. B.1 and B.2 exhibit flow properties at a steady state condition. In Fig. B.1, there is a small difference in the neutral density near the axis of symmetry for the domain ($r = 0$). However, the velocity streamlines overlaid on the simulation domain are very similar between the two domains. In Fig. B.2, there is good agreement between the average properties along the thruster channel centerline. The normalized average root mean square (RMS) error between the data sets is approximately 1.0% for the density and 2.1% for the axial velocity. This is the most important result, since the main area of concern for the HET simulation is the thruster channel and adjacent near-field plume. Thus, the conclusion is that the DK 2D2V approach can be used for the UM/AFRL P5 HET domain; results may be directly compared with those obtained via the PIC 2D3V approach.

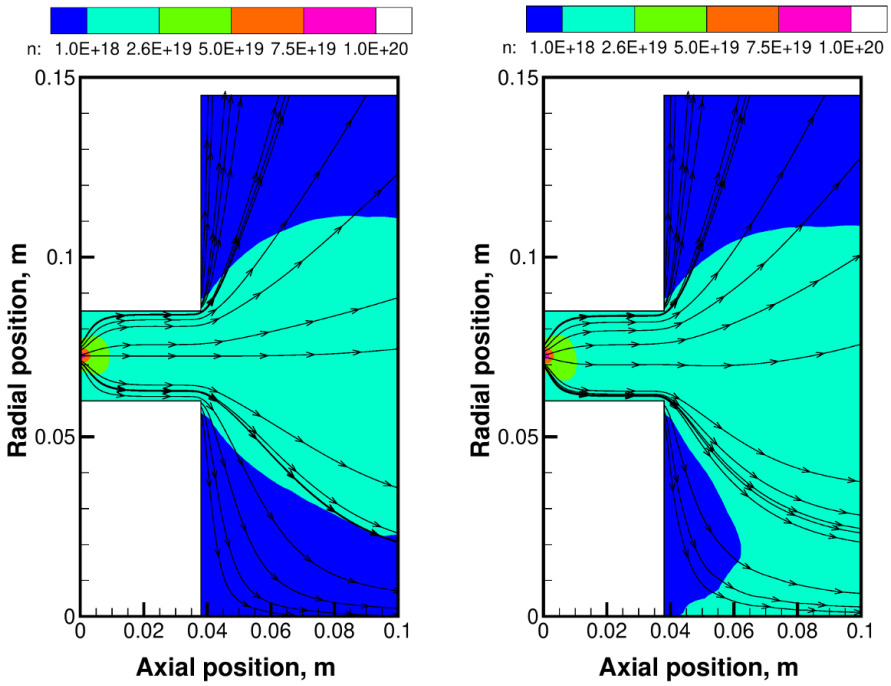

Figure B.1: Average neutral atom density contours overlaid with neutral velocity streamlines. (Left) planar simulation domain. (Right) axisymmetric simulation domain.

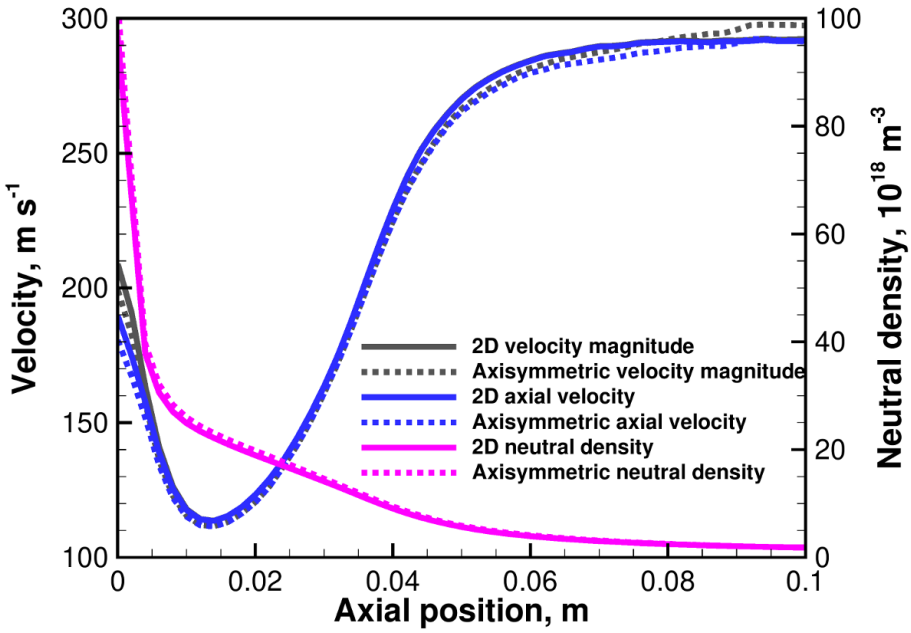

Figure B.2: Average planar (2d2v) and axisymmetric (2d3v) neutral properties along the thruster channel centerline for the UM/AFRL P5 HET domain.

BIBLIOGRAPHY

[1] Gurnett, D. A. and Bhatacharjee, A., *Introduction to Plasma Physics: With Space and Laboratory Applications*, Cambridge University Press, 2005.

[2] Boyd, I. D. and Schwartzentruber, T. E., *Nonequilibrium Gas Dynamics and Molecular Simulation*, Cambridge University Press, 2017.

[3] Galitzine, C., *On the Accuracy and Efficiency of the Direct Simulation Monte Carlo Method*, Ph.D. thesis, University of Michigan, 2014.

[4] Hager, R., Yoon, E. S., Ku, S., D'Azevedo, E. F., Worley, P. H., and Chang, C. S., "A fully non-linear multi-species Fokker-Planck-Landau collision operator for simulation of fusion plasma," *Journal of Computational Physics*, , No. 315, 2016, pp. 644–660.

[5] White, F. M., *Viscous Fluid Flow*, McGraw-Hill, 1974.

[6] Vincenti, W. G. and C. H. Kruger, J., *Introduction to Physical Gas Dynamics*, Krieger Publishing Company, 1965.

[7] Hara, K., *Development of Grid-Based Direct Kinetic Method and Hybrid Kinetic-Continuum Modeling of Hall Thruster Discharge Plasmas*, Ph.D. thesis, University of Michigan, 2015.

[8] Bellan, P. M., *Fundamentals of Plasma Physics*, Cambridge University Press, 2006.

[9] Li, Z. and Livescu, D., "High-order two-fluid plasma solver for direct numerical simulations of plasma flows with full transport phenomena," *Physics of Plasmas*, Vol. 26, No. 012109, 2019.

[10] Chen, F. F., *Introduction to Plasma Physics*, Plenum Press, 1974.

[11] Bird, G., *Molecular Gas Dynamics and the Direct Simulation of Gas Flows*, Oxford University Press, 1994.

[12] Hara, K. and Hanquist, K., "Test cases for grid-based direct kinetic modeling of plasma flows," *Plasma Sources Science and Technology*, Vol. 27, No. 065004, 2018.

[13] Hanquist, K. M., Hara, K., and Boyd, I. D., "Detailed modeling of electron emission for transpiration cooling of hypersonic vehicles," *Journal of Applied Physics*, Vol. 121, No. 5, 2017.

[14] Campanell, M. D. and Umansky, M. V., "Are two plasma equilibrium states possible when the emission coefficient exceeds unity?" *Physics of Plasmas*, Vol. 24, No. 057101, 2017.

[15] Hara, K., Boyd, I. D., and Kolobov, V. I., "One-dimensional hybrid-direct kinetic simulation of the discharge plasma in a Hall thruster," *Physics of Plasmas*, Vol. 19, No. 113508, 2012.

[16] Hara, K., Sekerak, M. J., Boyd, I. D., and Gallimore, A. D., "Mode transition of a Hall thruster discharge plasma," *Physics of Plasmas*, Vol. 21, No. 122103, 2014.

[17] Hara, K. and Kubota, K., "Direct kinetic simulation of ion acoustic turbulence in cathode plume," *IEPC-2017-496*, 2017.

[18] Hara, K. and Boyd, I. D., "Axial-azimuthal hybrid-direct kinetic simulation of Hall effect thrusters," *IEPC-2015-286*, 2015.

[19] Vazsonyi, A. R. and Boyd, I. D., "An Axisymmeteric Direct Kinetic Solver for Simulation of Hollow Cathode Plasmas," *IEPC-2019-331*, 2019.

[20] Raisanen, A. L., Hara, K., and Boyd, I. D., "Two-dimensional hybrid-direct kinetic simulation of a Hall thruster discharge plasma," *Physics of Plasmas*, Vol. 26, No. 123515, 2019.

[21] Liang, R., *The Combination of Two Concentric Discharge Channels into a Nested Hall-Effect Thruster*, Ph.D. thesis, University of Michigan, 2013.

[22] Lev, D., Myers, R. M., Lemmer, K. M., Kolbeck, J., Koizumi, H., and Polzin, K., "The technological and commercial expansion of electric propulsion," *Acta Astronautica*, Vol. 159, 2019, pp. 213–227.

[23] Goebel, D. M. and Katz, I., *Fundamentals of Electric Propulsion: Ion and Hall Thrusters*, JPL Space Science and Technology Series, 2008.

[24] Morozov, A. I., "The Conceptual Development of Stationary Plasma Thrusters," *Plasma Physics Reports*, Vol. 29, No. 3, 2003, pp. 235–250.

[25] Boeuf, J.-P., "Tutorial: Physics and modeling of Hall thrusters," *Journal of Applied Physics*, Vol. 121, No. 011101, 2017.

[26] Hofer, R. R., Goebel, D. M., Mikkelides, I. G., and Katz, I., "Magnetic shielding of a laboratory Hall thruster. II. Experiments," *Journal of Applied Physics*, Vol. 115, No. 043304, 2014.

[27] Cusson, S. E., Georgin, M. P., Dragnea, H. C., Dale, E. T., Dhaliwal, V., Boyd, I. D., and Gallimore, A. D., "On channel interactions in nested Hall thrusters," *Journal of Applied Physics*, Vol. 123, No. 133303, 2018.

[28] Wang, Y. M., Xu, S., Levchenko, I., Huang, S. Y., Xu, L. X., and Yu, M. Y., "Approach to a simplified numerical optimization of low-power Hall thrusters," *Vacuum*, Vol. 152, 2018, pp. 173–183.

[29] Hara, K., "An overview of discharge plasma modeling for Hall effect thrusters," *Plasma Sources Science and Technology*, Vol. 28, No. 044001, 2019.

[30] Choueiri, E. Y., "Plasma oscillations in Hall thrusters," *Journal of Applied Physics*, Vol. 8, No. 1411, 2000.

[31] Sekerak, M. J., *Plasma Oscillations and Operational Modes in Hall Effect Thrusters*, Ph.D. thesis, University of Michigan, 2014.

[32] Ellison, C. L., Raitses, Y., and Fisch, N. J., "Cross-field electron transport induced by a rotating spoke in a cylindrical Hall thruster," *Physics of Plasmas*, Vol. 19, No. 013503, 2012.

[33] Tsikata, S. and Minea, T., "Modulated Electron Cyclotron Drift Instability in a High-Power Pulsed Magnetron Discharge," *Physical Review Letters*, Vol. 114, No. 185001, 2015.

[34] Marusov, N. A., Sorokina, E. A., Lakhin, V. P., Ilgisonis, V. I., and Smolyakov, A. I., "Gradient-drift instability applied to Hall thrusters," *Plasma Sources Science and Technology*, Vol. 28, No. 015002, 2019.

[35] Adams, J. C., Boeuf, J. P., Dubuit, N., Dudeck, M., Garrigues, L., Gresillon, D., Heron, A., Hagelaar, G. J. M., Kulaev, V., N., L., Mazouffre, S., Perez Luna, J., Pisarev, V., and Tsikata, S., "Physics, simulation and diagnostics of Hall effect thrusters," *Plasma Phys. Control. Fusion*, Vol. 50, No. 124041, 2008.

[36] Boeuf, J. P. and Garrigues, L., "E×B electron drift instability in Hall thrusters: Particle-in-cell simulations vs. theory," *Physics of Plasmas*, Vol. 25, No. 061204, 2018.

[37] Dale, E. T. and Jorns, B. A., "Non-invasive time-resolved measurements of anomalous collision frequency in a Hall thruster," *Physics of Plasmas*, Vol. 26, No. 013516, 2019.

[38] Cusson, S. E., Dale, E. T., Jorns, B. A., and Gallimore, A. D., "Acceleration region dynamics in a magnetically shielded Hall thruster," *Physics of Plasmas*, Vol. 26, No. 023506, 2019.

[39] Taccogna, F. and Garrigues, L., "Latest progress in Hall thruster plasma modelling," *Reviews of Modern Plasma Physics*, Vol. 3, No. 1, 2019.

[40] Grimaud, L., Mazouffre, S., and Boniface, C., "Performance comparison between standard and magnetically shielded 200 W Hall thrusters with BN-SiO2 and graphite channel walls," *IEPC-2017-172*, 2017.

[41] Ortega, A. L., Mikellides, I. G., Sekerak, M. J., and Jorns, B. A., "Plasma simulations in 2-D (r-z) geometry for the assessment of pole erosion in a magnetically shielded Hall thruster," *Journal of Applied Physics*, Vol. 125, No. 033302, 2019.

[42] Fife, J. M., *Hybrid-PIC modeling and electrostatic prode survey of Hall thrusters*, Ph.D. thesis, Massachusetts Institute of Technology, 1999.

[43] Hofer, R. R., *Development and Characterization of High-Efficiency, High-Specific Impulse Xenon Hall Thrusters*, Ph.D. thesis, University of Michigan, 2004.

[44] Koo, J. W. and Boyd, I. D., "Modeling of anomalous electron mobility in Hall thrusters," *Phys. of Plasmas*, Vol. 13, No. 033501, 2006.

[45] Hagelaar, G. J. M., Bareilles, J., Garrigues, L., and Boeuf, J. P., "Two-dimensional model of a stationary plasma thruster," *Journal of Applied Physics*, Vol. 91, No. 5592, 2002.

[46] Morozov, A. I., Esipchuk, Y. V., Tilinin, G. N., Trofimov, A. V., Sharov, Y. A., and Shchepkin, G. Y., "Plasma Accelerator with Closed Electron Drift and Extended Acceleration Zone," *Soviet Journal of Plasma Physics*, 1972, pp. 17–38.

[47] Hara, K., "Non-oscillatory quasineutral fluid model of cross-field discharge plasmas," *Physics of Plasmas*, Vol. 25, No. 123508, 2018.

[48] Koo, J. W., *Hybrid PIC-MCC Computational Modeling of Hall Thrusters*, Ph.D. thesis, University of Michigan, 2005.

[49] Garrigues, L., Mazouffre, S., and Bourgeois, G., "Computed versus measured ion velocity distribution functions in a Hall effect thruster," *Journal of Applied Physics*, Vol. 111, No. 113301, 2012.

[50] Taccogna, F. and Dilecce, G., "Non-equilibrium in low-temperature plasmas," *European Physical Journal D*, Vol. 70, No. 251, 2016.

[51] Huang, W., Gallimore, A. D., and Hofer, R. R., "Neutral Flow Evolution in a Six-Kilowatt Hall Thruster," *Journal of Propulsion and Power*, Vol. 27, No. 3, 2011.

[52] Katz, I., Hofer, R. R., and Goebel, D. M., "Ion Current in Hall Thrusters," *IEEE Transactions on Plasma Science*, Vol. 36, No. 5, 2008, pp. 2015–2024.

[53] Smith, B. D., *A Numerical Study of Wall Erosion and Material Transport in Hall Thrusters*, Ph.D. thesis, University of Michigan, 2015.

[54] Hofer, R. R., Goebel, D. M., Mikellides, I. G., and Katz, I., "Design of a Laboratory Hall Thruster with Magnetically Shielded Channel Walls, Phase II: Experiments," *AIAA-2012-3788*, 2012.

[55] Puech, V. and Mizzi, S., "Collision Cross Sections and Transport Parameters in Neon and Xenon," *Journal of Physics D: Applied Physics*, Vol. 24, 1991, pp. 1974–1985.

[56] Huismann, T., *Improving Hall Thruster Plume Simulation through Rarefied Characterization of Near-field Plasma Properties*, Ph.D. thesis, University of Michigan, 2011.

[57] Boeuf, J. P. and Garrigues, L., "Low frequency oscillations in a stationary plasma thruster," *Journal of Applied Physics*, Vol. 84, No. 7, 1998.

[58] Hofer, R. R., Katz, I., Mikellides, I. G., Goebel, D. M., Jameson, K. K., Sullivan, R. M., and Johnson, L. K., "Efficacy of Electron Mobility Models in Hybrid-PIC Hall Thruster Simulations," *AIAA-2008-4924*, 2008.

[59] Cheng, C. Z. and Knorr, G., "The Integration of the Vlasov Equation in Configuration Space," *Journal of Computational Physics*, Vol. 22, 1976, pp. 330–351.

[60] Palmroth, M., Ganse, U., and et. al, Y. P.-K., "Vlasov methods in space physics and astrophysics," *Living Rev Comput Astrophys*, Vol. 4, No. 1, 2018.

[61] Shoucri, M., "Eulerian codes for the numerical solution of the Vlasov equation," *Communications in Nonlinear Science and Numerical Simulation*, Vol. 13, No. 1, 2008, pp. 174–182.

[62] Thomas, A. G. R., "Vlasov simulations of thermal plasma waves with relativistic phase velocity in a Lorentz boosted frame," *Phys Rev. E*, Vol. 94, No. 053204, 2016.

[63] Wettervik, B. S., DuBois, T. C., Siminos, E., and Fulop, T., "Relativistic Vlasov–Maxwell modelling using finite volumes and adaptive mesh refinement," *Eur Phys Journal D*, Vol. 71, No. 157, 2017.

[64] Batishchev, O. V., *Semi-Analytical Adaptive Vlasov - Fokker - Planck - Boltzmann Methods*, chap. 7, Nova Science Publishers, Inc., 2010, pp. 237–315.

[65] Nevins, W. M., Hammett, G. W., Dimits, A. M., Dorland, W., and Shumaker, D. E., "Discrete particle noise in particle-in-cell simulations of plasma microturbulence," *Physics of Plasmas*, Vol. 12, No. 122305, 2005.

[66] Birdsall, C. L. and Langdon, A. B., *Plasma Physics via Computer Simulation*, Institute of Physics Publishing, 1991.

[67] Aydemir, A. Y., "A unified Monte Carlo interpretation of particle simulations and applications to non-neutral plasmas," *Physics of Plasmas*, Vol. 1, No. 822, 1994.

[68] Hu, G. and Krommes, J. A., "Generalized weighting scheme for df particle-simulation method," *Physics of Plasmas*, Vol. 1, No. 863, 1994.

[69] Riva, F., Beadle, C. F., and Ricci, P., "A methodology for the rigorous verification of Particle-in-Cell simulations," *Physics of Plasmas*, Vol. 24, No. 055703, 2017.

[70] Radtke, G. A., Cartwright, K. L., and Musson, L. C., "Stochastic Richardson Extrapolation Based Numerical Error Estimation for Kinetic Plasma Simulations," *Sandia Technical Report, SAND2015-8620*, 2015.

[71] Faghihi, D., Carey, V., Michoski, C., Hager, R., Janhunen, S., Chang, C. S., and Moser, R. D., "Moment preserving constrained resampling with applications to particle-in-cell methods," *Journal of Computational Physics*, Vol. 409, No. 109317, 2020.

[72] Mikellides, I. G. and Katz, I., "Numerical simulations of Hall-effect plasma accelerators on a magnetic-field-aligned mesh," *Phys. Rev. E*, Vol. 86, No. 046703, 2012.

[73] Ahedo, E., Martinez-Cerezo, P., and Martinez-Sanchez, M., "One-dimensional model of the plasma flow in a Hall thruster," *Physics of Plasmas*, Vol. 8, No. 3058, 2001.

[74] Yim, J. T., *Computational Modeling of Hall Thruster Channel Wall Erosion*, Ph.D. thesis, University of Michigan, 2008.

[75] Adam, J. D., Heron, A., and Laval, G., "Study of stationary plasma thrusters using two-dimensional fully kinetic simulation," *Physics of Plasmas*, Vol. 11, No. 1, 2004, pp. 295–305.

[76] Szabo, J. J., *Fully Kinetic Numerical Modeling of a Plasma Thruster*, Ph.D. thesis, Massachusetts Institute of Technology, 2001.

[77] Taccogna, F., Schneider, R., Longo, S., and Capitelli, M., "Kinetic simulations of a plasma thruster," *Plasma Sources Sci. Technol.*, Vol. 17, No. 024003, 2008.

[78] Fernandez, E., Cappelli, M., and Mahesh, K., "2D simulations of Hall thrusters," *Center for Turbulence Research*, 1998.

[79] Gamero-Castano, M. and Katz, I., "Estimation of Hall Thruster Erosion Using HPHall," *IEPC-2005-303*, 2005.

[80] Ahedo, E., "Presheath/sheath model with secondary electron emission from two parallel walls," *Physics of Plasmas*, Vol. 9, 2002, pp. 4340–4347.

[81] Parra, F. I., Ahedo, E., Fife, J. M., and Martìnez-Sánchez, M., "A two-dimensional hybrid model of the Hall thruster discharge," *Journal of Applied Physics*, Vol. 100, No. 023304, 2006.

[82] Hofer, R. R., Mikellides, I. G., Katz, I., and Goebel, D. M., "Wall sheath and electron mobility modeling in hybrid-PIC Hall thruster simulations," *AIAA-2007-5267*, 2007.

[83] Dragnea, H. C. and Boyd, I. D., "Axisymmetric Fully 2D Hybrid-PIC Model for Hall Thrusters," *AIAA-2018-4811*, 2018.

[84] Scharfe, M. K., Gascon, N., Capelli, M. A., and Fernandez, E., "Comparison of hybrid Hall thruster model to experimental measurements," *Physics of Plasmas*, Vol. 13, No. 083505, 2006.

[85] Scharfe, M. K., Thomas, C. A., Scharfe, D. B., Gascon, N., Capelli, M. A., and Fernandez, E., "Shear-Based Model for Electron Transport in Hybrid Hall Thruster Simulations," *IEEE Transactions on Plasma Science*, Vol. 36, No. 5, 2008.

[86] Dunaevsky, A., Raitses, Y., and Fisch, N., "Secondary electron emission from dielectric materials of a Hall thruster with segmented electrodes," *Physics of Plasmas*, Vol. 10, No. 2574, 2003.

[87] Leer, B. V., "Towards the ultimate conservative difference scheme. IV. A new approach to numerical convection," *Journal of Computational Physics*, Vol. 23, No. 3, 1977, pp. 276–299.

[88] Arora, M. and Roe, P. L., "A Well-Behaved TVD Limiter for High-Resolution Calculations of Unsteady Flow," *Journal of Computational Physics*, Vol. 132, No. CP965514, 1997, pp. 3–11.

[89] Raisanen, A. L., Hara, K., and Boyd, I. D., "Two-dimensional Hybrid-Direct Kinetic Simulation of a Hall Thruster," *AIAA-2018-4809*, 2018.

[90] Haas, J. M. and Gallimore, A. D., "Internal plasma potential profiles in a laboratory-model Hall thruster," *Physics of Plasmas*, Vol. 8, No. 652, 2001.

[91] Peterson, P. Y., Gallimore, A. D., and Haas, J. M., "An experimental investigation of the internal magnetic field topography of an operating Hall thruster," *Phys. of Plasmas*, Vol. 9, No. 4364, 2002.

[92] Haas, J. M., *Low-perturbation Interrogation of the Internal and Near-field Plasma Structure of a Hall Thruster Using a High-speed Probe Positioning System*, Ph.D. thesis, University of Michigan, 2001.

[93] Massey, D., Kieckhafer, A., Sommerville, J., and King, L. B., "Development of a Vaporizing Liquid Bismuth Anode for Hall Thrusters," *AIAA-2004-3768*, 2004.

[94] Dannenmeyer, K. and Mazouffre, S., "Sizing of Hall effect thrusters with input power and thrust level: An Empirical Approach," *Journal of Technical Physics*, Vol. 49, No. 3-4, 2008.

[95] Raisanen, A. L., Hara, K., and Boyd, I. D., "Assessment of a two-dimensional hybrid-direct kinetic simulation of a Hall thruster," *AIAA-2017-4727*, 2017.

[96] Lim, Y., Choe, W., Mazouffre, S., Park, J. S., Kim, H., Seon, J., and Garrigues, L., "Nonlinear ion dynamics in a Hall thruster plasma source by ion transit-time instability," *Plasma Sources Science and Technology*, Vol. 26, No. 3, 2017.

[97] Bareilles, J., Hagelaar, G. J. M., Garrigues, L., Boniface, C., Boeuf, J. P., and Gascon, N., "Critical assessment of a two-dimensional hybrid Hall thruster model: comparison with experiments," *Physics of Plasmas*, Vol. 11, No. 3035, 2004.

[98] Nishiguchi, A. and Yabe, T., "Second-Order Fluid Particle Scheme," *Journal of Computational Physics*, Vol. 52, 1983, pp. 390–413.

[99] Dorf, L., Raitses, Y., and Fisch, N. J., "Effect of anode dielectric coating on Hall thruster operation," *Appl. Phys. Lett.*, Vol. 84, No. 1070, 2004.

[100] Thomson, C. D., *Measurements of the Secondary Electron Emission Properties of Insulators*, Ph.D. thesis, Utah State University, 2005.

[101] Levchenko, I., Xu, S., Teel, G., Mariotti, D., Walker, M., and Keidar, M., "Recent progress and perspectives of space electric propulsion systems based on smart nanomaterials," *Nature*, Vol. 9, 2018, pp. 879.

[102] Takamura, S., Ohno, N., Ye, M. Y., and Kuwabara, T., "Space-Charge Limited Current from Plasma-Facing Material Surface," *Contrib. Plasma Phys.*, Vol. 44, 2004, pp. 126–137.

[103] Schwager, L. A. and Birdsall, C. K., "Collector and source sheaths of a finite ion temperature plasma," *Phys. Fluids B: Plasma Physics*, Vol. 2, 1990, pp. 1057–68.

[104] Sheehan, J. P., Hershkowitz, N., Kaganovich, I. D., Wang, H., Raitses, Y., Barnat, E. V., Weatherford, B. R., and Sydorenko, D., "Kinetic Theory of Plasma Sheaths Surrounding Electron-Emitting Surfaces," *Phys. Rev. Lett.*, Vol. 111, No. 075002, 2013.

[105] Kim, D. and Economou, D., "Simulation of a two-dimensional sheath over a flat insulator conductor interface on a radio-frequency biased electrode in a high density plasma," *Journal of Applied Physics*, Vol. 95, No. 3311, 2004.

[106] Schiesko, L., Carrere, M., Cartry, G., and Layet, J. M., "Experimental study and modeling of the electron-attracting sheath: The influence of secondary electron emission," *Physics of Plasmas*, Vol. 15, No. 073507, 2008.

[107] Balruud, S. D., Scheiner, B., Yee, B. T., Hopkins, M. M., and Barnat, E., "Interaction of Biased Electrodes and Plasmas: Sheaths, Double Layers, and Fireballs," *Plasma Sources Sci. Technol.*, Vol. in press, 2020.

[108] Falgout, R., Baker, A., Chow, E., Hensen, V. E., Hill, E., Jones, J., Kolev, T., Lee, B., Painter, J., Tong, C., Vassilevski, P., and Yang, U. M., *Users' Manual, HYPRE High Performance Preconditioners*, 2002, Lawrence Livermore National Laboratory.

[109] Hittinger, J. and Banks, J., "Block-structured adaptive mesh refinement algorithms for Vlasov simulation," *Journal of Computational Physics*, Vol. 241, 2013, pp. 118–140.

[110] Raisanen, A. L. and Boyd, I. D., "Boundary conditions in a direct kinetic simulation of a Hall thruster," *IEPC-2019-613*, 2019.

[111] Deriaz, E. and Peirani, S., *Multiscale Modeling and Simulation: A SIAM Interdisciplinary Journal*, Vol. 16, No. 2, 2018, pp. 583–614.

[112] Kolobov, V. I. and Arslanbekov, R. R., "Towards adaptive kinetic-fluid simulations of weakly ionized plasmas," *Journal of Computational Physics*, Vol. 231, 2011, pp. 839–869.

[113] Roytershteyn, V. and Delzanno, G. L., "Spectral Approach to Plasma Kinetic Simulations Based on Hermite Decomposition in the Velocity Space," *Front. Astron. Space Sci.*, Vol. 5, 2018, pp. 27.